



FACULTE DES SCIENCES

Jülich Center for Neutron Sciences und Peter Grünberg Institute PGI
JCNS-2, PGI-4: Scattering Methods
"Lattice Dynamics in Emerging Functional Materials" group
Forschungszentrum Jülich

Structure and Lattice Dynamics of Bismuth Telluride Nanostructures

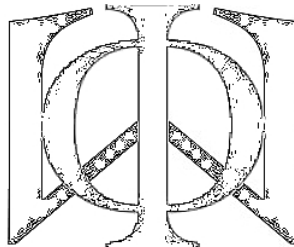
Année académique 2011-2012

Dissertation présentée par
Dimitrios Bessas
en vue de l'obtention du grade de
Docteur en Sciences



FACULTE DES SCIENCES
Jülich Center for Neutron Sciences und Peter Grünberg Institute PGI
JCNS-2, PGI-4: Scattering Methods
"Lattice Dynamics in Emerging Functional Materials" group
Forschungszentrum Jülich

Structure and Lattice Dynamics of Bismuth Telluride Nanostructures



Année académique 2011-2012

Dissertation présentée par
Dimitrios Bessas
en vue de l'obtention du grade de
Docteur en Sciences

Dimitrios Bessas

Structure and Lattice Dynamics of Bismuth Telluride Nanostructures

THESIS JURY:

Prof. Dr. Rudi Cloots

Dr. Raphaël P. Hermann, Prof. Inv. (supervisor)

Dr. Werner Schweika

Prof. Dr. Benedikt Vetryen

Prof. Dr. Kornelius Nielsch

Prof. Dr. Mathieu Verstraete (chairman)

Liège, 2012

Study hard what interests you the most
in the most undisciplined, irreverent
and original manner possible.

— Richard P. Feynman

ABSTRACT

A brief outline of experimental lattice dynamics related to thermal transport in solids introduces this thesis. The introduction is followed by three chapters dedicated to structure and lattice dynamics of bulk and nanostructured bismuth telluride, a chapter on lattice instabilities observed in bulk EuTiO_3 around room temperature, and a chapter on the development of a resonant ultrasound spectrometer for small samples.

First, the lattice dynamics in bulk Bi_2Te_3 and Sb_2Te_3 were investigated by nuclear inelastic scattering, diffraction of high energy synchrotron radiation and calorimetry. In combination with earlier inelastic neutron scattering data, the element specific density of phonon states was extracted not only for Te and Sb but also for Bi. The Bi-Te bonding in Bi_2Te_3 is fundamentally different than the Sb-Te bonding in Sb_2Te_3 . It appears that the Te specific density of phonon states is mostly unaffected upon substitution of Sb with Bi. Phonon polarization analysis was conducted in a Bi_2Te_3 single crystal. The observed low lattice thermal conductivity in bulk Bi_2Te_3 and Sb_2Te_3 results essentially from the small acoustic cut off energy.

Second, the lattice dynamics in elemental modulated Sb_2Te_3 films were studied by nuclear inelastic scattering and diffraction of high energy synchrotron radiation. These studies reveal that the main features in the Sb specific density of phonon states arise from the layered structure. The extracted average speed of sound is practically the same as in bulk Sb_2Te_3 . The impact of the acoustic cut off energy is further highlighted.

Third, the phonon confinement in a Bi_2Te_3 nanowire array was studied by nuclear inelastic scattering, diffraction of high energy synchrotron radiation, scanning as well as transmission electron microscopy. For the first time the element specific density of phonon states was measured on nanowires in two perpendicular orientations. The much lower than in bulk average speed of sound measured in 56 nm diameter nanowires is directly related to the confined dimensions. The related 50 % decrease in macroscopic thermal conductivity is in line with macroscopic measurements on similar nanowires.

Fourth, a detailed structural and lattice dynamical investigations of the bulk cubic perovskite EuTiO_3 revealed a lattice instability close to room

temperature. The low temperature phase is associated with anharmonic europium displacement and has a significant impact in the lattice dynamics.

Last, a resonant ultrasound spectrometer for measurements on small samples and thin films was developed. Successful measurements versus temperature of the elastic constants were carried out with sub-percentage accuracy on oriented single crystals smaller than 1 mm^3 .

RÉSUMÉ

Une brève description des aspects expérimentaux de la dynamique de réseau liée au transport thermique dans les solides introduit cette thèse. L'introduction est suivie de trois chapitres dédiés à la structure et la dynamique de réseau dans le tellurure de bismuth sous forme bulk et nanostructurée, une chapitre sur l'instabilité de réseau observée dans EuTiO_3 à température ambiante, et un chapitre sur le développement d'un spectromètre à résonance d'ultrasons pour de petits échantillons.

Premièrement, la dynamique de réseau dans Bi_2Te_3 et Sb_2Te_3 sous forme bulk a été étudiée par diffusion nucléaire résonante inélastique, par diffraction de rayonnement synchrotron de haute énergie et par calorimétrie. In combinaison avec des données antérieures de diffusion inélastique de neutrons, la densité d'états des phonons élémentaire à été extraite non seulement pour Te et Sb mais aussi pour Bi. La liaison Bi-Te dans Bi_2Te_3 est fondamentalement différente de la liaison Sb-Te dans Sb_2Te_3 . Il apparaît que la densité d'états de phonons spécifique de Te est essentiellement non affectée par la substitution de Sb par Bi. Une analyse de la polarisation des phonons a également été réalisée sur un monocristal de Bi_2Te_3 . La faible conductivité thermique du réseau dans Bi_2Te_3 et Sb_2Te_3 sous forme bulk résulte essentiellement de la faible énergie de coupure pour les phonons acoustiques.

Deuxièmement, la dynamique de réseau dans un film de Sb_2Te_3 déposé par modulation élémentaire a été étudiée par diffusion nucléaire résonante inélastique et par diffraction de rayonnement synchrotron de haute énergie. Ces études montrent que les aspects principaux dans la densité d'états de phonons spécifique de Sb proviennent de la structure en couche. La vitesse du son moyenne est essentiellement la même que dans Sb_2Te_3 sous forme bulk. L'impact de l'énergie de coupure des phonons acoustiques est à nouveau mise en évidence.

Troisièmement, le confinement des phonons dans un arrangement de nanofils de Bi_2Te_3 a été étudié par diffusion nucléaire résonante inélastique et par diffraction de rayonnement synchrotron de haute énergie ainsi que par microscopie électronique par transmission et par balayage. Pour la première fois, une densité d'états de phonons élémentaire a été obtenue sur des nanofils dans deux directions perpendiculaires. La vitesse du son beaucoup

plus faible que dans le bulk mesurée dans ces nanofils de 56 nm de diamètre est directement liée aux confinement spatial. La diminution associée de 50 % de la conductivité thermique est en accord avec des mesures macroscopiques sur de nanofils similaires.

Quatrièmement, une étude détaillée de la structure et de la dynamique de réseau dans la perovskite bulk EuTiO_3 a montré une instabilité de réseau proche de la température ambiante. La phase basse température est associée à des déplacement anharmonique de l'euprium et a un impact significatif sur la dynamique de réseau.

Finalement, un spectromètre à résonance d'ultrasons pour des mesures sur de petits échantillons a été développé. Des mesures des constantes élastique en fonction de la température ont été réalisées avec succès sur des monocristaux orientés plus petits que 1 mm^3 .

KURZBESCHREIBUNG

Eine Kurzfassung experimenteller Gitterdynamik in Bezug auf den thermischen Transport in Festkörpern leitet diese Dissertation ein. Der Einleitung folgen drei Kapitel, die sich mit der Struktur und Gitterdynamik in bulk und nanostrukturiertem Wismuttellurit befassen, ein Kapitel, in welchem die Gitterinstabilität in EuTiO_3 nahe Zimmertemperatur behandelt wird, und ein Kapitel über die Entwicklung eines resonanten Ultraschallspektrometers zur Messung kleiner Proben.

Erstens wurde die Gitterdynamik in bulk Bi_2Te_3 und Sb_2Te_3 mittels inelastischer Kernresonanzstreuung, hochenergetischer Röntgenbeugung mit Synchrotronstrahlung und kalorimetrischen Methoden untersucht. Zusammen mit früheren Daten der inelastischen Neutronenbeugung wurde die elementspezifische Phononenzustandsdichte nicht nur für Te und Sb sondern auch für Bi bestimmt. Die Bi-Te Bindung in Bi_2Te_3 ist grundsätzlich verschieden von der Sb-Te Bindung in Sb_2Te_3 . Es scheint, dass die Te elementspezifische Phononenzustandsdichte durch die Substitution von Sb mit Bi im Wesentlichen unverändert bleibt. Eine Analyse der phononischen Polarisation wurde an einem Bi_2Te_3 Einkristall durchgeführt. Die beobachtete niedrige Wärmeleitfähigkeit in bulk Bi_2Te_3 und Sb_2Te_3 ist hauptsächlich auf die niedrige Abschneidefrequenz des akustischen Bereiches zurückzuführen.

Zweitens wurde die Gitterdynamik in elementmodulierten Sb_2Te_3 Filmen, die durch schichtweise Deposition der Elemente hergestellt wurden, mittels inelastischer Kernresonanzstreuung und hochenergetischer Röntgenbeugung untersucht. Diese Studie zeigt, dass die Hauptmerkmale der Sb elementspezifischen Phononenzustandsdichte von der geschichteten Struktur bestimmt werden. Die ermittelte Schallgeschwindigkeit ist im Wesentlichen die gleiche wie in bulk Sb_2Te_3 . Die Rolle der akustischen Abschneidefrequenz wird ebenfalls bestätigt.

Drittens wurde die räumlich-dimensionale Einschränkung von Phononen in einer Anordnung von Bi_2Te_3 Nanostäben mittels inelastischer Kernresonanzstreuung, hochenergetischer Röntgenbeugung und sowohl Raster- wie Transmissionselektronenmikroskopie untersucht. Zum ersten Mal wurde die Phononenzustandsdichte elementspezifisch in Nanostäben gemessen, sowohl senkrecht als auch parallel zur Stabachse. Die viel niedrigere Schallgeschwin

digkeit im Vergleich zum Bulk in den 56 nm durchmessenden Nanostäben wird direkt durch die verringerten Dimensionen verursacht. Die damit verbundene 50 % Verminderung der makroskopischen Wärmeleitfähigkeit ist im Einklang mit Messungen an ähnlichen Nanostäben.

Viertens zeigte eine detaillierte Untersuchung der Struktur und der Gitterdynamik in bulk kubischem Perowskit EuTiO_3 eine Gitterinstabilität nahe Zimmertemperatur. Die Tieftemperaturphase ist mit anharmonischen Bewegungen des Europiums verbunden und hat einen bedeutenden Einfluss auf der Gitterdynamik.

Letztens wurde ein resonantes Ultraschallspektrometer für Messungen an kleinen Proben entwickelt. Messungen der elastischen Konstanten als Funktion der Temperatur wurden erfolgreich mit sub-Prozent Genauigkeit an orientierten Einkristallen kleiner als 1 mm^3 durchgeführt.

PUBLICATION DISSERTATION

Chapters 2 to 5 of this thesis contain the main body of manuscripts that are submitted or will be submitted shortly in peer reviewed journals. A summary of the conclusions is contained in Chapter 6. All references are sorted at the end of this dissertation.

Chapter 2:

D. Bessas, I. Sergueev, H.-C. Wille, J. Perßon, D. Ebling and R.P. Hermann, **Lattice dynamics in Bi_2Te_3 and Sb_2Te_3 : Te and Sb density of phonon states**, submitted to *Phys. Rev. B*, July 2012.

Chapter 3:

D. Bessas, M. Winkler, I. Sergueev, J.D. König, H.-C. Wille, H. Böttner, and R.P. Hermann, **Lattice dynamics in elemental modulated Sb_2Te_3** , to be submitted to *Phys. Rev. B (Brief Report)*, September 2012.

Chapter 4:

D. Bessas, W. Töllner, Z. Aabdin, N. Peranio, I. Sergueev, H.-C. Wille, O. Eibl, K. Nielsch and R.P. Hermann, **Phonon spectroscopy in Bi_2Te_3 nanowire array**, to be submitted to *Nanotechnology*, September 2012.

Chapter 5:

D. Bessas, M. Kachlik, S. Disch, O. Gourdon, K. Maca, I. Sergueev, S. Kamba and R.P. Hermann, **Lattice instabilities in bulk EuTiO_3** , submitted to *Phys. Rev. Lett.*, August 2012.

*those who manage well the circumstances they encounter day by day,
those who are not ultimately overcome by their misfortunes,
those who are decent and honorable in their intercourses,
those who hold their pleasures always under control,
those who are not spoiled by their successes,
those I call educated people.*

— Socrates [1]

ACKNOWLEDGMENTS

My gratitude goes to my supervisor Prof. Dr. Raphael P. Hermann for giving me the opportunity to explore a previously unknown world. His advice, material and ethical support as well as his multidimensional education was inspiring at any moment of this journey.

Special thanks to my co-supervisor Dr. Werner Schweika for his pedagogical way of handling my inquiries.

I would like to thank also my co-advisor at the Université de Liège Prof. Dr. Rudy Cloots. He was always keen to promote my education.

I thank Prof. Benedikt Vertruyen for following my educational progress and accepting to be in my thesis advisory committee and Prof. K. Nielsch for accepting to be in my thesis jury.

Many thanks to Prof. M. Verstraete for accepting to be the chairman of the examination jury.

Many people helped me to realise this work. Special thanks to Mr. R. Simon, Mr. M. Herlitschke, Ms. T. Claudio Weber, Ms. P. Bauer Pereira, Mr. W. Töllner, Mr. Z. Aabdin, Dr. B. Klobes, Dr. S. Nandi, Drs. Andreas and Anne Houben, Dr. S. Disch, Dr. G. Bruns, Dr. M. Winkler, Dr. J. D. König, Dr. D. Ebling, Dr. H. Böttner, Dr. V. Pacheco, Dr. A. Hashibon, Dr. F. Juranyi, Dr. D. Robinson, Dr. P. J. Ryan, Dr. N. Peranio, Dr. A. Shkabko, Dr. K. Z. Rushchanskii, Dr. M. Ležaić, Dr. O. Gourdon, Dr. M. Koza, Dr. J. Zhao, Dr. H.-C. Wille, Dr. I. Sergueev, Dr. A. Chumakov, Dr. E. Alp, Dr. R. Ruffer, Prof. Dr. O. Eibl, Prof. Dr. J. R. Gladden, Prof. Dr. J. Neumeier, Prof. Dr. F. Grandjean, Prof. Dr. Th. Brückel.

I would like to thank all my colleagues from JCNS-2 and PGI-4 for everyday communication and especially Mr. B. Schmitz and Mr. F. Gössen for their technical assistance.

For the funding of this thesis the DFG priority program SPP 1386 ‘Nanos-structured Thermoelectrics’ and the Helmholtz Association of German research centers (VH NG-407 “Lattice dynamics in emerging functional materials”) are acknowledged.

The European Synchrotron Radiation Facility, the Advanced Photon Source, the Petra III, the Spallation Neutron Source, the Paul Scherrer Institut, the Institute Laue-Langevin, the Forschungs-Neutronenquelle Heinz Maier-Leibnitz (FRM II), the Jülich Center for Neutron Science are acknowledged for provision of synchrotron radiation and neutron beamtime.

Finally, I want to thank Ms. Theodora Tzima for being my muse.

CONTENTS

1	INTRODUCTION	1
1.1	Lattice dynamics and thermal conductivity	1
1.2	Thermoelectricity	4
1.3	Measurement considerations	5
1.4	Studied materials and Organization	18
	I THERMODYNAMICS AND LATTICE DYNAMICS	23
2	LATTICE DYNAMICS IN BULK BISMUTH TELLURIDE AND ANTI-MONY TELLURIDE	25
2.1	Introduction	25
2.2	Experimental Method	27
2.3	Results	29
2.4	Discussion	37
3	LATTICE DYNAMICS IN ELEMENTAL MODULATED ANTIMONY TELLURIDE FILMS	45
3.1	Introduction	45
3.2	Experimental Method	46
3.3	Results	48
3.4	Discussion	50
4	PHONON SPECTROSCOPY IN BISMUTH TELLURIDE NANOWIRE ARRAY	53
4.1	Introduction	53
4.2	Experimental method	54
4.3	Results	56
4.4	Discussion	62
5	LATTICE INSTABILITIES IN BULK EUROPIUM TITANATE	67
5.1	Introduction	67
5.2	Preparation	68
5.3	Results and Discussion	68
5.4	Supplementary information	75
6	CONCLUSIONS	83
	II RESONANT ULTRASOUND SPECTROSCOPY	85
7	DEVELOPMENT OF A SMALL SAMPLE RUS SETUP	87
7.1	Mechanical resonances of small samples and thin films	87
7.2	Sample preparation	89
7.3	Experimental setup	91
7.4	Measurement considerations and possible errors	94

7.5	Computation	97
7.6	Proof of principle and outlook	100
7.7	Conclusions	104
7.8	Appendix	105
BIBLIOGRAPHY		131

LIST OF FIGURES

Figure 1	One dimensional linear atomic chain in the Born - von Karman approximation.	1
Figure 2	The phonon dispersion for a linear chain in the Born - von Karman approximation.	2
Figure 3	An anharmonic potential energy.	3
Figure 4	Illustration of a thermoelectric converter.	5
Figure 5	The sample holder for heat capacity measurements using the QD-PPMS.	7
Figure 6	The applied forces and the elastic deformation related to bulk and shear moduli.	8
Figure 7	The basic schematics of resonant ultrasound spectroscopy.	9
Figure 8	Elastic scattering process in the Fraunhofer approximation.	13
Figure 9	Snapshot of the nuclear excited states of ^{125}Te and various scattering processes that can follow from resonant absorption of γ -photons.	15
Figure 10	Experimental set-up for nuclear inelastic scattering measurements.	16
Figure 11	The nuclear inelastic scattering measured on a polycrystalline metallic Te sample at 20 K.	17
Figure 12	The tetradymite structure in which Bi_2Te_3 and Sb_2Te_3 crystallise.	19
Figure 13	The perovskite structure in which EuTiO_3 crystallises.	21
Figure 14	X-ray diffraction pattern of $\text{Bi}_2^{125}\text{Te}_3$ obtained at 295 K using synchrotron radiation.	27
Figure 15	The temperature dependence of the a and c lattice parameters for Sb_2Te_3 (open tics) and Bi_2Te_3 (filled tics) between 50 and 300 K	30
Figure 16	The nuclear inelastic scattering spectra obtained with the ^{125}Te and the ^{121}Sb resonances on $\text{Bi}_2^{125}\text{Te}_3$ and $\text{Sb}_2^{125}\text{Te}_3$	31
Figure 17	Density of phonon states measured with the ^{125}Te and ^{121}Sb resonance at 20 K on Sb_2Te_3	33
Figure 18	Element specific, Sb or Bi and Te, density of phonon states in Sb_2Te_3 and Bi_2Te_3	34
Figure 19	Orientation dependent Te DPS measured on a Bi_2Te_3 single crystal.	35

Figure 20	Specific heat at constant pressure, C_P , data measured on Sb_2Te_3 and Bi_2Te_3 between 3 and 300 K.	37
Figure 21	X-ray diffraction pattern of the elemental modulated Sb_2Te_3 film obtained at 295 K using synchrotron radiation in two orientations	47
Figure 22	The nuclear inelastic spectra obtained on the elemental modulated Sb_2Te_3 film in two orientations.	51
Figure 23	The alumina membrane filled with Bi_2Te_3 nanowires.	57
Figure 24	Diffraction of synchrotron radiation obtained on an array of Bi_2Te_3 nanowires with diameter of 56 nm embedded in a self ordered amorphous alumina membrane.	59
Figure 25	Te specific DPS measured in two orientations on an array of Bi_2Te_3 nanowires with 56 nm diameter embedded in amorphous alumina template	61
Figure 26	Rietveld refinement of a typical $EuTiO_3$ diffractogram at 300 K measured using synchrotron radiation.	69
Figure 27	Compilation of experimental data obtained on $EuTiO_3$ and comparison to $SrTiO_3$	70
Figure 28	Probability density function distribution of the Eu-atom in the ab plane at 180 K.	72
Figure 29	Temperature dependent ^{151}Eu -Mossbauer spectra measured on $EuTiO_3$ powder.	76
Figure 30	Temperature dependence of the ac magnetic susceptibility measured on cooling on $EuTiO_3$	77
Figure 31	Pair distribution function analysis of neutron scattering data obtained on $EuTiO_3$	79
Figure 32	The ^{151}Eu projected density of phonon states at 110, 210, 300 and 360 K.	80
Figure 33	The first 12 normal modes of a sample with plate like geometry.	88
Figure 34	A snapshot during polishing of a bulk polycrystalline sample.	90
Figure 35	Indicative types of geometry errors during the rectangular parallelepiped sample preparation.	91
Figure 36	The transducer holder and the bare RUS cell for small samples.	92
Figure 37	A scheme of the metallised PVDF transducer.	94
Figure 38	A snapshot of the sample mounting between the transducers using the vacuum tweezer.	95
Figure 39	Resonant ultrasound spectrometer for small samples mounted in the QD cryostat sample holder.	96

Figure 40	Sample loading effect in determination of resonant frequency.	97
Figure 41	Temperature dependence of a resonance recorded between 275 and 295 K on the same GaAs single crystalline sample.	98
Figure 42	A Laue diffraction pattern on a GaAs single crystalline substrate	101
Figure 43	The output of the elastic constants refinement	102
Figure 44	The elastic constants of GaAs between 100 and 300 K measured using the RUS cell for small samples.	103
Figure 45	A comparison of two RUS spectra measured on a bare substrate and two spectra measured on the same substrate covered with SnSb ₂ Te ₄ film.	104

LIST OF TABLES

Table 1	Independent elastic constants for various crystallographic symmetries	12
Table 2	Refinement parameters (pseudo-hexagonal notation) for $\text{Sb}_2^{125}\text{Te}_3$ and $\text{Bi}_2^{125}\text{Te}_3$ at 295 K.	28
Table 3	Summary of the lattice dynamics parameters on Sb_2Te_3 and Bi_2Te_3 , Lamb-Mössbauer factor f_{LM} , mean square atomic displacement $\langle u^2 \rangle$, mean force constants $\langle F_i \rangle$ obtained at 20 K.	39
Table 4	Summary of the thermodynamical parameters, speed of sound, v_s , Grüneisen parameter γ at 295 K, Debye Temperature θ_D and Schottky Temperature θ_S extracted from NIS at 20 K as well as the Schottky prefactor C_S	40
Table 5	Summary of crystallographic parameters extracted from x-ray diffraction by a nanoalloyed Sb_2Te_3 film in grazing incident geometry, transmission geometry and comparison with bulk Sb_2Te_3	49
Table 6	Temperature dependent anharmonic refined parameters $D_{\text{GC}}^{ijkl}(\mathbf{r})$ of Eu atom in EuTiO_3 refined using the Gram-Charlier expansion.	78
Table 7	Matrix for rotating a coordinate system using the angles of rotation α , β and γ	99

ACRONYMS

6-ID-D	High energy synchrotron diffraction beamline at APS
DPS	Density of Phonon States
FWHM	Full Width at Half Maximum
HC	Heat Capacity
ID18	Nuclear resonant inelastic beamline at ESRF
ID22N	Nuclear resonant inelastic beamline at ESRF, no longer in operation
NIS	Nuclear Inelastic Scattering
NW	Nanowires
PDF	Pair Distribution Function
POWGEN	Neutron time of flight diffractometer at SNS
RUS	Resonant Ultrasound Spectroscopy
SEM	Scanning Electron Microscopy
TEM	Transmission Electron Microscopy
XRD	X-Ray Diffraction

INTRODUCTION

This introduction is a brief outlook in experimental lattice dynamics related to thermal transport. More details are given in terms of references.

1.1 LATTICE DYNAMICS AND THERMAL CONDUCTIVITY

Several cases in which thermal conduction is essential, such as thermal barrier coatings for higher turbine operating temperature [2] and energy harvesting [3], are currently important topics in scientific research not only for fundamental but also for technological reasons. However, thermoelectricity is probably one of the few fields where both reasons are merging together with equal importance. The importance of lattice dynamics was highlighted as early as the current textbook example of an ensemble of coupled oscillators [4] was formulated and solved. The general case of a one dimensional infinite chain of atomic masses, m_1 , m_2 , connected with restoring forces is shown in Fig. 1. The solution of the equation of motion, i.e. the dispersion relation $\omega = \omega(k)$, is represented in Fig. 2.

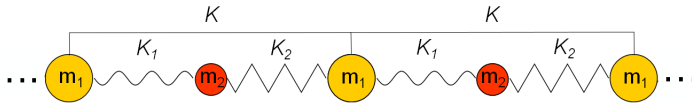


Figure 1: One dimensional linear atomic chain in the Born - von Karman approximation. m_1 stands for the host and m_2 for the guest atoms. The interatomic force constants K and K_1 , K_2 are given, respectively.

In a monoatomic linear chain, i.e. $m_1 = m_2$ and $K = K_1 = K_2$, the phonon dispersion relation follows the Debye approximation, $\omega = v \cdot k$, in the low energy region and flattens, $\omega = \omega_{max}$, at the zone boundary. In a diatomic linear chain, i.e. $m_1 \neq m_2$, in addition to the lowering of group velocity, $v_g(\omega) = d\omega/dk$, high-energy optical phonons emerge, see red curve in Fig.2. In the same case by increasing the K_2 force constant an extended avoided crossing between the phonon modes appears. This example is extensively discussed in Ref. [5]. Modifications in phonon dispersion have an influence on macroscopically measured properties such as the lattice

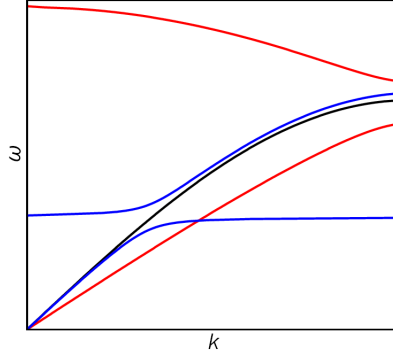


Figure 2: The phonon dispersion for a monoatomic linear chain (black curve), diatomic (red curve) and diatomic chain with stiff framework (m_1, K) and loosely bound guest atoms (m_2, K_1, K_2) in the Born - von Karman approximation.

thermal conductivity. In a simplified Callaway model [6] of solely phonon - phonon interactions the lattice thermal conductivity, k_L , is given by Eq. 1.1.

$$k_L = \frac{1}{3} \int_0^{E_{max}} C_V(E) v_g^2(E) \tau(E) dE \quad (1.1)$$

where C_V is the heat capacity at constant volume, v_g is the group velocity, τ is the phonon lifetime and E_{max} is the cut-off energy of the phonons that transport heat. Thus, lattice thermal conductivity can be modified by modifying each of its three ingredients. A common approach is the reduction of the group velocity either by polyatomic unit cells [7] or by nanostructuring [8].

The underlying mechanisms in modifying the phonon dispersion curve stem from either major or minor modifications in the underlying potential energy of the system under investigation. Both from the theoretical as well as from the experimental perspective there is no single method which can provide full information about the potential energy. In first approximation, the potential energy can be assumed as a harmonic potential but a more realistic asymmetric potential energy is shown in Fig. 3. The asymmetry of the potential in Fig. 3 is depicted in the shift of the equilibrium atomic distance from r_0 to r_1 and r_2 at temperature T_1 and T_2 .

Thus, several experimental techniques, both microscopic and macroscopic, have been developed or are lately under development which probe the inter-

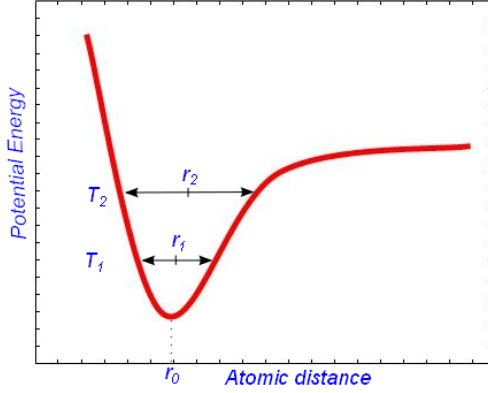


Figure 3: An anharmonic potential energy and the atomic distance equilibrium, r_0 , r_1 and r_2 at absolute zero temperature, at T_1 and at T_2 , respectively.

atomic potential. The global minimum of the potential energy is defined by the first derivative of the potential energy with respect to the interatomic distance, $\left. \frac{dU_{i,m}}{dr} \right|_{r_0} = 0$, and provides information about the interatomic distance, r_0 . The average interatomic distance can primarily be probed by diffraction experiments using either neutrons or x-rays having wavelength comparable to the interatomic distance. The curvature of the interatomic potential close to the global minimum is expressed mathematically by the second derivative of the potential with respect to the interatomic distance, $\left. \frac{d^2U_{i,m}}{dr^2} \right|_{r_0} \sim C_{ij}$, and provides information about the elastic constants, C_{ij} , of the system. Additional information can be extracted from the temperature evolution of the potential energy global minimum such as the thermal expansion coefficient, α_V . In the adiabatic approximation [9], thermal expansivity expresses the deviation of the interatomic potential energy from the parabolic shape. Although it is only indirectly related to thermal conduction, it is one of the fundamental properties for the lattice dynamical characterization. Once all aforementioned properties are measured or calculated the Grüneisen parameter, γ , given in Eq. 1.2 is calculated.

$$\gamma = \frac{\alpha_V}{C_V K_T} \quad (1.2)$$

where K_T is the isothermal compressibility and C_V the heat capacity at constant volume.

In an one dimensional ensemble of N atoms interacting through pair potentials, $\phi(r)$, and constrained to have a length $L = Na$, where a is the equilibrium lattice constant, the Grüneisen parameter is given by $\gamma = -\frac{a}{2} \frac{\phi'''(a)}{\phi''(a)}$ [10]. In case the potential has a parabolic shape the extracted Grüneisen parameter is 0. In case the potential is proportional to the well known Lennard - Jones formula, $\phi(r) = \epsilon \left[\left(\frac{a}{r}\right)^{12} - 2 \left(\frac{a}{r}\right)^6 \right]$, and if only nearest-neighbor interactions are appreciable, then $\gamma \approx 11$. However, in simple metallic systems the experimentally measured Grüneisen parameter [9] is around 2 which indicates that neither the harmonic approximation nor the Lennard - Jones potential is valid. The Grüneisen parameter is the hallmark of anharmonicity and can also be defined through the vibrational energy, E , change, $\gamma = -\frac{d \ln E}{d \ln V}$, where V the unit cell volume. Conclusions based only on the Grüneisen parameter should be drawn with great care because various results exist even for the same compound [11]. It is, thus, better to carefully consider the source of the very high or very low extracted parameter than its absolute value.

1.2 THERMOELECTRICITY

Thermoelectric converters enable the conversion of thermal energy to electric energy by harnessing the heat flow across a thermal gradient to generate charge flow and vice versa. A conversion module is comprised of n- and p-type semiconducting counterparts coupled electrically in series, see Fig. 4. The thermoelectric figure of merit, zT , quantifies the material's efficiency output and is given in Eq.1.3.

$$zT = \frac{S^2 \sigma}{k_e + k_L} \quad (1.3)$$

Lattice dynamics expressed in terms of lattice thermal conductivity, k_L , is one of the constituents of the thermoelectric figure of merit with the other being the Seebeck coefficient, S , and the Wiedemann - Franz law [10], $\frac{\sigma}{k_e} = LT$, where L the Lorentz number. In order to estimate the actual device efficiency, electrical and thermal resistances due to device engineering must also be taken into account. However, here this contribution is neglected. The straightforward but tedious calculation on the dependence of the efficiency, η , upon zT , $\eta = \frac{T_H - T_C}{T_H} \frac{\sqrt{1+zT} - 1}{\sqrt{1+zT} + \frac{T_C}{T_H}}$ where T_H is the temperature at the hot junction and T_C is the temperature at the surface being cooled, can be found in Ref. [12]. Currently a realistic device efficiency is below 10% but in theory the upper limit is only the Carnot efficiency. In any case recovering energy using thermoelectricity can be considered a green energy source not only

because it is a greenhouse gas free technology but also because it recovers energy which in fact be wasted.

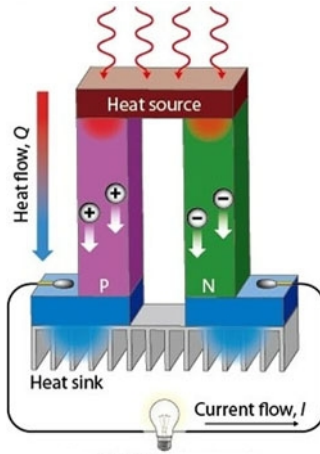


Figure 4: Illustration of a thermoelectric converter [13]. The p- and n-type semi-conducting legs, the electrical carriers, the thermal gradient and the flowing current are shown.

There are currently several approaches on how to maintain low thermal conductivity and at the same time sufficient electrical conductivity which are summarised in a review by Snyder and Toberer [14].

1.3 MEASUREMENT CONSIDERATIONS

Several techniques for probing microscopically the lattice dynamics of a system exist and are mainly associated with scattering methods, e.g. scattering of electrons [15], helium atoms [16], photons [17], neutrons [18] etc. The distinguishing parameters among them are in the properties of the used particles, such as the kinetic energy and the interaction with matter, and thus gives information on different length and time scales. Two main categories of microscopic experimental techniques which focus on the dynamics of a system can be distinguished:

- direct scattering techniques which give access to the density of electronic states, of phonon states, of magnon states.
- indirect scattering techniques which mainly probe local effects, i.e. surface properties or limited space of the Brillouin zone.

Both microscopic and macroscopic measurements have been used in the framework of this study. Among the macroscopic techniques, heat capacity at constant pressure, C_P , using the relaxation method as well as resonant ultrasound spectroscopy for obtaining the elastic tensor and consequently the speed of sound, v_S , in a material have been used. Both C_P and v_S are contributing to the lattice thermal conductivity, κ_L , according to Eq. 1.1. To substantiate the macroscopically observed phenomena and to obtain deeper insight in their origin complementary microscopic methods have also been used. Diffraction of synchrotron radiation as well as neutron diffraction were carried out in a series of compounds giving information not only about static parameters i.e. crystallographic structure but also on dynamical properties such as atomic displacement parameters in the coherent limit [19]. In addition, inelastic techniques, mainly nuclear inelastic scattering has been developed and applied to tellurium based chalcogenides suitable for thermoelectric applications. The element specific and polarization projected density of phonon states, $g(E)$, is available together with all the related properties, e.g. heat capacity at constant volume, C_V , Debye level, $\lim_{E \rightarrow 0} \frac{g(E)}{E^2}$, speed of sound in the Debye approximation, v_S , mean force constants, $\langle F \rangle$, Lamb - Mössbauer factor, f_{LM} , and atomic displacement parameter in the incoherent limit. The complementarity of the used techniques gives us the opportunity to deeply investigate the origin of the observed phenomena and to answer questions such as the different Te bonding in Sb_2Te_3 and Bi_2Te_3 , the importance of layered structures upon the lattice dynamics, the significance of phonon engineering as well as to reveal the europium displacement in $EuTiO_3$. In the next paragraphs we will set the scene on the experimental methods and techniques used in this study and try to guide the reader through the routes we traced.

1.3.1 Heat Capacity Measurements

Heat Capacity is defined as the amount of energy required to raise the temperature of a certain amount of material by one Kelvin. Heat capacity probes fundamental properties in many fields of physics, chemistry and material science. For instance, lattice dynamics - phonons - of several systems [20] have been explained, Schottky anomalies in paramagnetic salts [21] and heavy fermion systems [22] have been revealed, electronic contributions in metals have been measured [10] and phase transitions have been recorded [23, 24]. From the mathematical point of view the relation of heat capacity with all the aforementioned properties is given in Eq. 1.4.

$$C_P = \left. \frac{\partial H}{\partial T} \right|_P \quad (1.4)$$

The heat capacity under constant pressure, C_P , is a function of the enthalpy, H , of the investigated system and thus sensitive to any phenomenon affecting directly the internal energy. Heat capacity measurements were traditionally difficult in realisation because strict thermal insulation issues should be fulfilled during measurement. In former times, such measurements were accessible only to few specialists who had the knowledge and the equipment to realise them. Although today commercial automated systems are available to wider group of scientists, several pitfalls need to be overcome in order to obtain meaningful results.

At least three methods for measuring accurately heat capacity at constant pressure exist nowadays. In chronological order, the adiabatic technique, the relaxation technique and the AC technique. It is common ground in all of them that a set of heaters and high accuracy thermometers should be placed in close contact with the sample which is secured using a thermal coupling grease.

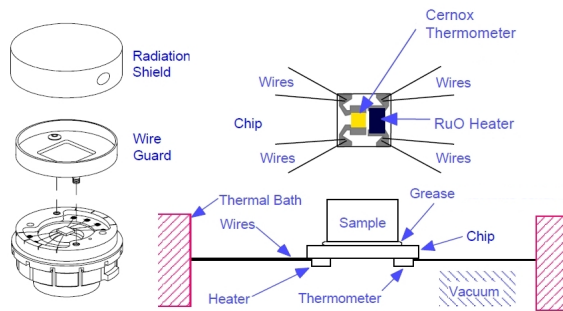


Figure 5: The sample holder (puck) for heat capacity measurements [25] using the QD-PPMS. The set of heater - thermometer and the sample position is shown. (Adapted from QD manual)

Here the relaxation technique was used utilising the Quantum Design calorimeter [25]. In this technique, a heat pulse is applied to the sample and the transient temperature is recorded both during and after the application of the heat pulse. After fitting the transient signal with a model [26], taking into account the coupling of the sample holder with the environment, the heat capacity of the sample is readily available. The main drawback of this technique is that in data analysis a curve fitting is involved which could lead to result misinterpretation if measuring conditions are not ideal.

A possible common error in all heat capacity measurements is related to the thermal coupling of the sample and the sample holder, see Fig. 5. Normally a high thermal conductivity grease is used. However, the used grease has a finite

heat capacity as well which sometimes does not have smooth temperature dependence [27]. Hence, it is mandatory that the addenda measurement is not too coarse.

1.3.2 Elastic Constants - Resonant Ultrasound Spectroscopy

Measurements of elastic constants are divided into two main categories: methods which are based on scattering techniques [28, 29, 30] and all others which are utilizing macroscopic mechanical vibrations [31, 32] and tension. Although both have advantages and disadvantages, the strong point of the latter is that no complicated and expensive experimental hardware is required and it is possible to perform such measurements in a typical laboratory environment. Even adopting the mechanical deformation as a way of estimating the stress, σ_{xy} , - strain, ε_{xy} , relation, $\sigma_{xy} = C_{ij}\varepsilon_{xy}$, there is still a wide variety of approaches in obtaining the desired results. For example in an isotropic sample, such as ordinary glass, there are only two existing elastic moduli, the shear, C_{44} , and the bulk modulus, C_{11} . An illustration of shear and bulk deformation related to the applied forces is depicted in Fig. 6

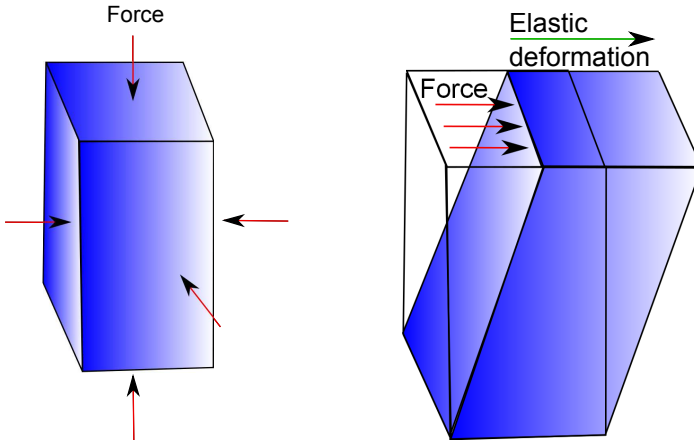
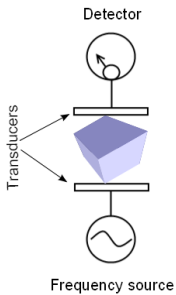


Figure 6: The applied external forces and the elastic deformation related to the bulk, left, and shear moduli, right are shown.

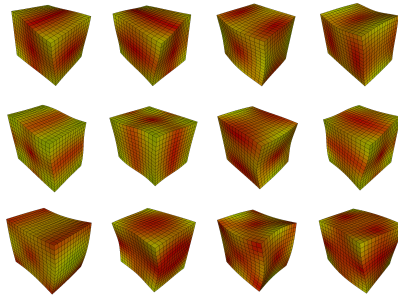
Historically, the quasistatic method appeared first. In this approach the applied stress and the induced strain is determined in the frequency range of 100 Hz. The attractive characteristic of this technique is that all measurements are carried out at low frequencies, which makes the related apparatus really

inexpensive. On the other hand, this method is not qualified as a low noise, ultra precise measurement technique since the isolation of low frequency noise is still an important issue.

After the quasistatic method, time-of-flight techniques have been used. This method relies on the measurement of the required time-of-flight for an elastic wave to be transmitted through a pathway in a medium with given properties. Concerning precision issues related to up-to-date electronic equipment, a typical frequency range of several MHz is applicable for a sample length of several cm. The readily obtained results are related to the speed of the transported elastic wave in a specific direction, v_{xy} , which is directly related to the elastic constants, C_{ij} , of the medium, $v_{xy} = \sqrt{C_{ij}/\rho}$, where ρ is the mass density. More information about the wave dispersion can be obtained concerning the wave attenuation which is inherent in any material. This technique appears more powerful than the quasistatic approach since the frequency range currently well suits the needs of the existing electronic equipment. However, in case the measurement is performed on single crystals of low symmetry, several elastic constants depending on the crystallographic orientation exist. Hence, different transducer mounting should be done either on the same or different samples introducing independent errors which are most of the time difficult to predict.



(a) RUS schematic.



(b) The first 12 normal modes of an Al rectangular parallelepiped sample with dimensions $0.9 \text{ mm} \cdot 1.1 \text{ mm} \cdot 1.0 \text{ mm}$. The figure was reconstructed from the calculated eigenvectors using Mathematica. The red areas denote high strain regions.

Figure 7: The basic schematic of resonant ultrasound spectroscopy, detector - transducers - frequency source, and an example of Al rectangular parallelepiped sample normal modes are shown.

The general importance of elasticity has been identified very early in the previous century [33]. However, the need for computer power for solving the related theoretical models was not available at that time and thus resonant ultrasound spectroscopy appeared in the mid 90's. In this method, a sample of well defined geometry is put between two piezoelectric transducers, as shown in Fig. 7. One of the two transducers triggers the sample's mechanical resonances and the opposite transducer records the response. The frequency range for the observation of resonances depends on the sample shape and size as well as on its elastic constants. The typical frequency range for a sample volume of 10 mm^3 assuming elastic constants in the range of several GPa is a few MHz. However, the information derived from resonant ultrasound spectra is not related to the elastic constants via a simple linear transformation. A numerical analysis based on the minimisation of the Langrangian of the system is carried out in order to obtain the elastic constants. Several approaches have been followed in the Langrangian minimisation. Among them the Rayleigh - Ritz method is usually adopted but finite element calculation have also been reported [34]. Resonant ultrasound spectroscopy is based on classical mechanics. Thus the equation of motion is a modification of Newtons law, see Eq. 1.5.

$$\rho\omega^2 \varphi_i + \sum_{j,k,l} C_{ijkl} \frac{\partial^2 \varphi_k}{\partial x_j \partial x_l} = 0 \quad (1.5)$$

The eigenvalues, ω , in Eq.1.5 are the resonant frequencies observed experimentally and the eigenfunction φ can be expanded in any set of basis. Visscher et al [35] made a crucial contribution in the development of resonant ultrasound spectroscopy by introducing very simple basis functions, a set of simple powers of the cartesian coordinates, $x^p y^q z^r$ with p, q, r positive integers with their extremum set by $N \leq p + q + r$. Mathematically, the Eq.1.5 reduces to the explicit calculation of the integral $f(p, q, r) = \int_V x^p y^q z^r dV$. Thus, all feasible sample shapes, e.g.rectangular parallelepipeds, cylinders, and spheres, can be described. Eq. 1.5 gives us the opportunity not only to extract the elastic constants given a set of resonances using a least square minimisation process (inverse problem) but also from an estimate of elastic constants the mechanical resonances can be predicted (forward problem). Although the approach of cartesian coordinates expansion is not the most efficient regarding computing power, it offers flexibility in the geometry of the sample being modelled. The elastic constants, C_{ijkl} , have the form of a tensor of fourth order. To make the fourth order tensor less obscure we divide the four subscripts in pairs of two, $ij \equiv I, kl \equiv K$ and then the elastic constant matrix is having the form C_{IK} . Regarding the I, K indices the transformation

follows the Voigt convention: $11 \equiv 1$, $22 \equiv 2$, $33 \equiv 3$, $23 \equiv 4$, $13 \equiv 5$, $12 \equiv 6$, $32 \equiv 4$, $31 \equiv 5$, and $21 \equiv 6$. As a result, in the most general case the elastic constant matrix has the form indicated in Eq. 1.6.

$$\begin{pmatrix} \sigma_1 \\ \sigma_2 \\ \sigma_3 \\ \sigma_4 \\ \sigma_5 \\ \sigma_6 \end{pmatrix} = \begin{pmatrix} C_{11} & C_{12} & C_{13} & C_{14} & C_{15} & C_{16} \\ C_{12} & C_{22} & C_{23} & C_{24} & C_{25} & C_{26} \\ C_{13} & C_{23} & C_{33} & C_{34} & C_{35} & C_{36} \\ C_{14} & C_{24} & C_{34} & C_{44} & C_{45} & C_{46} \\ C_{15} & C_{25} & C_{35} & C_{45} & C_{55} & C_{56} \\ C_{16} & C_{26} & C_{36} & C_{46} & C_{56} & C_{66} \end{pmatrix} \begin{pmatrix} \varepsilon_1 \\ \varepsilon_2 \\ \varepsilon_3 \\ \varepsilon_4 \\ \varepsilon_5 \\ \varepsilon_6 \end{pmatrix} \quad (1.6)$$

The theory to describe the elastic behaviour of single crystals as well as crystalline aggregates exists since long time [36]. It takes into account the symmetries imposed by the crystallographic structure as well as the macroscopic stress and strain relation. The elastic tensor in its general form has 36 elements. However, 21 is the maximum number of independent elastic constants observed in the most anisotropic, triclinic, crystal structure. On the other hand the most isotropic crystal structure, cubic, possesses only 3 independent elastic constants as shown in Table 1. The higher the number of independent elastic constants the higher is the complexity to extract them from the measured data. For polycrystalline aggregates only 2 independent elastic constants exist. The translation of single crystalline elastic constants to isotropic was extensively described by Hill [37]. In his approach two ways are important in obtaining a shear, C_{44} , and bulk modulus, C_{11} , from anisotropic elastic constants, the Voigt and the Reuss average.

In the former, isostrain conditions are assumed during mechanical loading. In the latter, isostress conditions are assumed. Thus, the mathematical procedure according to Voigt average is performed on the elastic constants, in the contrary, in the Reuss average all mathematical operations are done on the elastic compliances¹. However, even today there is no straightforward analysis on the extraction of elastic constants from a non fully isotropic, textured, material. We faced this problem in Chapter 2, where it was not possible to obtain a macroscopically isotropic pellet of the layered compounds Bi_2Te_3 and Sb_2Te_3 . In this case, mechanical resonances have been observed coming from the sample however the refined elastic constants were not in agreement with previously measured elastic constants on single crystals of similar materials. Further detailed information on the resonant ultrasound technique is given in Chapter 7.

¹ The elastic compliances are equal to the inverse elastic constants

CRYSTALLOGRAPHIC SYMMETRY	INDEPENDENT ELASTIC CONSTANTS
Triclinic	All possible combinations
Monoclinic	$C_{11}, C_{12}, C_{13}, C_{16}, C_{22}, C_{23}, C_{26}, C_{33}, C_{36}, C_{44}, C_{45}, C_{55}, C_{66}$
Orthorombic	$C_{11}, C_{12}, C_{13}, C_{22}, C_{23}, C_{33}, C_{44}, C_{55}, C_{66}$
Trigonal	$C_{11}, C_{12}, C_{13}, C_{14}, C_{33}, C_{44}, (C_{25})$
Tetragonal	$C_{11}, C_{12}, C_{13}, C_{33}, C_{44}, C_{66}$
Hexagonal	$C_{11}, C_{12}, C_{14}, C_{33}, C_{44}$
Cubic	C_{11}, C_{12}, C_{44}
Isotropic	C_{11}, C_{44}

Table 1: Independent elastic constants for various crystallographic symmetries

1.3.3 Elastic Scattering - Diffraction

Atomic long range translational order is the basic characteristic of crystalline materials. This picture emerges from early pioneering work established by von Laue, Bragg, Ewald, Langevin and others. In order to draw their conclusions the founders of crystallography used elastic scattering processes of radiation mainly coming from x-ray tubes. Today a variety of particles, apart from photons, including electrons, neutrons, helium atoms, etc are available. In the elastic scattering framework, excluding special cases of magnetic scattering, highly absorbing compounds and scattering from so-called low-Z elements, given the de-Broglie principle almost all aforementioned particles can be used. The energy, E , - wavelength, λ , relation, for massive $\lambda = \frac{h}{\sqrt{2mE}}$ and non massive particles $\lambda = \frac{hc}{E}$ where c is the speed of light, plays central role in deciding not only about the feasibility of diffraction experiments but also on its corresponding accuracy. For example, by taking into account the Bragg's law, $2d\sin\theta = \lambda$ where d is the distance between crystallographic planes and 2θ is the angle between incident and scattered beam, the lower the wavelength the more reflections are observed in a fixed experimental setup. In elastic scattering the absolute value of energy, or equivalently the absolute value of momentum before, $|\vec{k}_i|$ and after $|\vec{k}_f|$, scattering, does not change. The vector, $\vec{Q} = \vec{k}_f - \vec{k}_i$, is defined as the scattering vector. Bragg scattering takes place when the momentum transfer, $|\vec{Q}|$, is equal to a reciprocal lattice vector, $|\vec{G}|$,

in the momentum phase space. According to Fig. 8 the momentum transfer is given by the formula: $|\vec{Q}| = 2|\vec{k}_f| \sin\theta = \frac{4\pi}{\lambda} \sin\theta$. Constructive interference takes place at certain 2θ as well as destructive interference happens for all other angles. Thus, the positions of the observed peaks (reflections) in the measured diffractogram provides information about the reciprocal lattice or the crystallographic symmetry in real space. However, this is not the only information one can extract from a diffractogram. Apart from the peak positions the intensities of the reflections can be used.

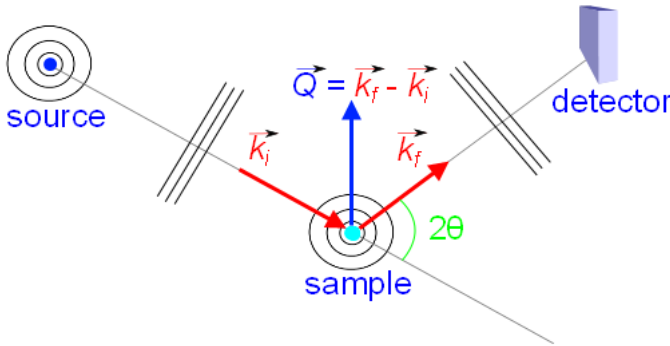


Figure 8: Elastic scattering process in the Fraunhofer approximation. The detector as well as the source is viewed at a long distance from the diffracting object.

Any crystal structure is a real space convolution of a periodic infinitesimal set of points, the lattice, with a set of finitely extended atoms, the so-called base. In reciprocal space the scattering amplitude, F^{crystal} , is a multiplication of both contributions. The structure factor is related to the structure, and the form factor is linked to the atomic base resulting in $F^{\text{crystal}} = \sum_j f(\vec{Q}) e^{i\vec{Q}\vec{R}_j}$, where $f(\vec{Q})$ is the form factor and the summation runs over all atomic positions. Since, the atomic positions, \vec{R}_j , change with time due to thermal vibrations it is more convenient to describe them in terms of a deviation from their average positions, $\vec{R}_j(t) = \langle \vec{R}_0 \rangle + \vec{u}(t)$ where $\langle \vec{R}_0 \rangle$ is the time average position and $\vec{u}(t)$ is correspondingly the atomic displacement. Taking into account the atomic displacement, information can be obtained not only about static, $\langle \vec{R}_0 \rangle$, but also about dynamical properties, $\vec{u}(t)$.

Typically, the observed diffractogram (I_{obs} versus Q) is composed of many reflections. The intensity of each, provided that scattering amplitude as well

as the instrumental details are known, can be precisely calculated from Eq. 1.7.

$$I_{\text{obs}} = s \sum_{h,k,l} L_{hkl} \left| F_{hkl}^{\text{crystal}} \right|^2 \Phi P_{hkl} + I_0 \quad (1.7)$$

where s is a scale factor, L_{hkl} contains the polarization and multiplicity factor, F_{hkl}^{crystal} is the contribution of the scattering amplitude for a specific reflection, Φ is the instrumental function, P_{hkl} is the preferred orientation function and I_0 is the instrumental background intensity. The fitting procedure or refinement using the Rietveld method is given in Eq. 1.7. Currently such refinement is performed using several software editions [38, 39]. In this work, the diffraction patterns were refined mostly using the Fullprof [40] program.

1.3.4 Nuclear Scattering of x-rays

The elastic nuclear absorption of γ -rays by the so called ‘Mössbauer’ isotopes is known as nuclear resonance scattering. The nuclear excited states related to nuclear absorption are typically in the keV regime and have energy widths of several neV (or lifetime in the ns range). Therefore the excitation of such short lived nuclear transitions requires a high spectral density and a high brilliance of x-rays. Nuclear resonance scattering for solid state research is thus performed either at hard x-ray beamlines at large scale synchrotron radiation facilities or using relevant radioactive sources [41]. Although radioactive sources have been historically pioneering in this field, nowadays due to the importance of the technique in various field of scientific research, i.e. physics, chemistry, material science, geology, biology etc, the largest high energy third generation synchrotron radiation facilities (ESRF, APS, PETRAIII, SPRING-8) have a dedicated beamline for such measurements. However, for simple nuclear resonance measurements under normal conditions, i.e. by varying temperature or external fields (electric, magnetic, etc), measurements using synchrotron radiation are not competitive because the intensity per unit area per unit time is of the same order of magnitude with the one obtained using radioactive sources available in physics laboratories. This is not the case for special measurements, i.e. measurements under extreme conditions (high pressure) [42]. Key issues in the realization of such measurements are the monochromatization of the incident beam as well as the detection of the scattered beam. For more information on the nuclear resonance scattering the reader can follow Ref. [43].

In addition to elastic nuclear resonance scattering, x-ray nuclear absorption may take place inelastically with creation or annihilation of vibrational states,

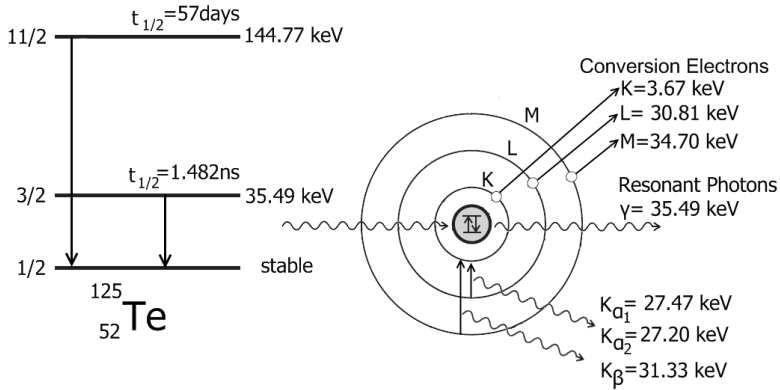


Figure 9: The nuclear excited states of ^{125}Te and various scattering and emission processes that can follow from resonant absorption of γ -photons. Data were summarized from [44].

and a corresponding nuclear inelastic spectrum can be obtained. This method relies essentially on the phonon assisted nuclear resonant absorption and can be used to directly probe phonon states. Nuclear inelastic scattering emerges as sidebands in the energy spectra around the elastic peak. The energy spectrum of nuclear inelastic scattering provides direct information about the density of phonon states of the probed nucleus. However, in contrast to other inelastic techniques such as inelastic neutron scattering, Raman scattering and infrared absorption, nuclear inelastic scattering is isotope selective, purely incoherent and provides an ideal integration over momentum space of the phonon spectrum.

Nowadays, for technical reasons related both to development of monochromators as well as the development of ultra-fast detectors, nuclear inelastic scattering is measured only for isotopes with relatively low resonance energies, less than 40 keV [45], and long lifetimes of the excited states, roughly more than 0.8 ns [46]. As an example the nuclear level scheme and various scattering processes that can follow from ^{125}Te are depicted in Fig. 9. A special experimental setup for performing nuclear inelastic scattering is wanted. From the user perspective the dedicated nuclear inelastic scattering setup is depicted in Fig. 10. The synchrotron radiation bunches should be well separated in time domain in order to provide a corresponding time window for the nuclear deexcitation to take place and the products to be detected. Upstream, a high-heat load monochromator is located with throughput of $\sim \text{eV}$. In order, to resolve vibrational states, in the meV energy range, a high resolution

– high efficiency monochromator is crucial. Several routes for the design of high resolution – high efficiency monochromators have been followed, such as multibounce and backscattering schemes and are summarized in Ref. [47]. A rather traditional approach is to use a set of crystals and to scan the energy by fine tuning the beam incident angle on the monochromator [48]. In this study, we have utilized the back scattering geometry using a corundum single crystal as an active element. The thermal expansion of the monochromator, $\delta d/d$, very precisely determined, was used to change the energy of the reflected beam according to Bragg's law, $(\delta E/E)^2 = (\delta d/d)^2 + (\cot\theta_B \delta\theta_B)^2$. At the end, a sample environment with two sets of detectors is used. The energy dependence of the nuclear absorption (nuclear inelastic channel) is recorded by the first detector. At the same time, the second detector set monitors the nuclear forward scattering (nuclear resonance channel) which in its time integrated form is identical to the instrumental function. In order to distinguish the products of nuclear interaction from alternative channels of electronic origin the readings of both detectors are gated in time and data acquisition takes place only in the time window of interest. Fig. 11 shows the phonon spectrum measured between -10 and 40 meV (or between -25 and 100 mK around the corresponding temperature of the monochromator) around the resonant transition energy of ^{125}Te . The spectra were obtained by adding the results of several successive energy scans.

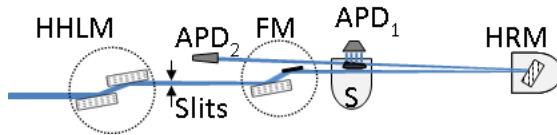


Figure 10: Experimental set-up for nuclear inelastic scattering measurements with high heat load monochromator (HHLM), high resolution monochromator (HRM), sample environment (S), avalanche photo diode detectors for measuring the instrumental function (APD₂) and the inelastic spectrum (APD₁). Figure is modified by Ref. [45].

Once the phonon spectrum is available, the well established theory of nuclear absorption [49] is applicable on the obtained data. A set of sum rules [50] can be applied on the raw data and gives information about fundamental properties of the substance related to the Mössbauer effect such as the recoil energy, E_R , the Lamb - Mössbauer factor, f_{LM} , as well as the density of phonon states, $g(E)$. The density of phonon states is directly related to the one phonon term. However, in the NIS experimental data single- and multi-phonon scattering is present. The one phonon term is separated from multiphonon scattering using a Fourier decomposition procedure [51] and

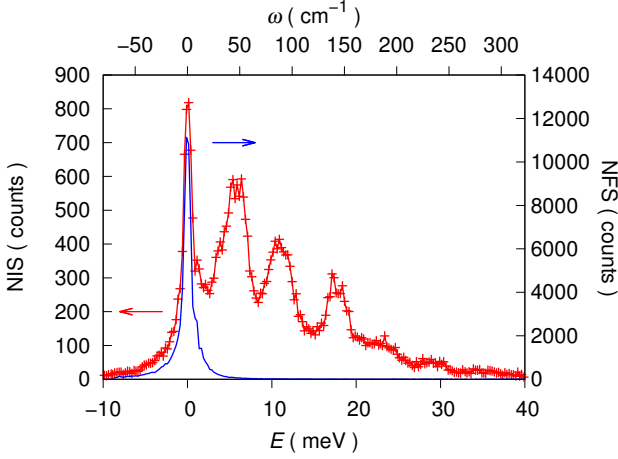


Figure 11: The nuclear inelastic scattering, NIS, measured on a polycrystalline metallic Te sample with the ^{125}Te resonance at 20 K (red points) and the time integrated nuclear forward scattering, NFS, which was measured as resolution function (blue line) [45].

the density of phonon states is extracted. A common experimental strategy for suppressing multiphonon scattering in NIS measurements is the reduction of temperature. Reliability of the obtained DPS is checked using several spectral moments calculated both from the raw spectra as well as the DPS. Furthermore, the temperature of the sample can be precisely calculated from the detailed balance of Bose - Einstein statistics.

An important issue on the extraction of the DPS from NIS which should be highlighted is its orientation dependence. The analysis methods discussed above hold for crystallographically isotropic samples, i.e. single crystals of cubic symmetry, polycrystalline or amorphous samples. However, in the case of low symmetry single crystals or textured powder the probability of phonon assisted nuclear absorption depends on the relative orientation of the beam with respect to the crystallographic axis [52]. In the general case the DPS is given in Eq. 1.8.

$$g(E, \vec{s}) = V_0 \sum_j \int \frac{d\vec{q}}{8\pi^3} \delta[E - \hbar\omega_j(\vec{q})] \frac{|\vec{k} \cdot \vec{e}_j(\vec{q})|^2}{k^2} \quad (1.8)$$

where $\vec{e}_j(\vec{q})$ is the phonon polarization and \hat{k} is a unit vector along the beam direction.

In the case of a single crystal irrespective from its crystallographic symmetry, according to the last term of Eq. 1.8 three phonon modes (two with propagation vector transversal and one longitudinal to the beam direction) with displacement along the beam direction can be excited. However, in order to signify the importance of this term, $\frac{|\vec{k} \cdot \vec{e}_j(\vec{q})|^2}{k^2}$, experimentally either combined diffraction experiments or NIS experiments in different orientations should be carried out. For randomly oriented powders or glasses the last term is equal to unity.

1.4 STUDIED MATERIALS AND ORGANIZATION

Among the case studies, pnictide-chalcogenide thermoelectrics with tetradymite crystal structure, see Fig. 12, are also suitable as reversible phase change materials, with a switching from crystalline to amorphous phase induced by temperature or electric field [53, 54]. Bismuth-antimony telluride solid solutions are widely used as room temperature solid state refrigerators and power generators [55]. However, although the end members of the series, i.e. Bi_2Te_3 and Sb_2Te_3 , are isostructural (space group $R\bar{3}m$) and have similar electronic configurations the observed macroscopic properties are significantly different. The peculiar Bi-Te bonding in these and similar compounds has been underlined in theoretical investigations [56, 57]. However, still no direct experimental proof on the peculiarity of the Bi-Te bonding exists. Using nuclear resonance inelastic scattering of ^{125}Te and ^{121}Sb on 95% ^{125}Te enriched Bi_2Te_3 and Sb_2Te_3 we have measured the nuclear resonant scattering probability function and extracted the isotope specific density of phonon states, DPS. In order to obtain the Bi DPS a harmonic approximation was assumed and the correct mass renormalization was applied on the Sb contribution assuming that the Bi-Te bonding in Bi_2Te_3 is identical with the Sb-Te bonding in Sb_2Te_3 . Thus, a pseudo Bi contribution was obtained and the total Bi_2Te_3 as well as the Sb_2Te_3 DPS are presented in Chapter 2. Comparison of our data with previously measured densities of phonon states using neutrons reveals substantial agreement for the Sb_2Te_3 DPS. However, the difference in the case of the reconstructed Bi_2Te_3 DPS is significant. We interpret this difference of the pseudo Bi_2Te_3 and neutron measured DPS as being caused mainly by the difference in bonding between Sb-Te and the Bi-Te.

In Chapter 3 the lattice dynamics on an elemental modulated Sb_2Te_3 film were investigated using ^{121}Sb nuclear inelastic scattering combined with high energy synchrotron radiation diffraction. The element specific density of phonon states was extracted and the nature of the Sb - Te interlayer

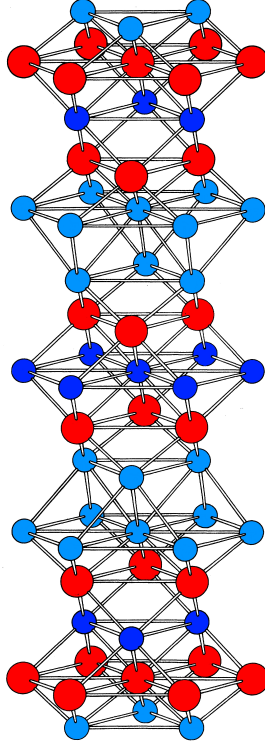


Figure 12: The tetradymite structure in which Bi_2Te_3 and Sb_2Te_3 crystallise. The blue balls stand for the Te atoms and the red for the Bi or Sb atoms, respectively. Figure is adapted from Ref. [58].

bond was investigated. Comparison with earlier nuclear inelastic scattering measurements on bulk Sb_2Te_3 reveals that the main features of the Sb specific density of phonon states arise from the layered structure.

Dimensionality effects have been proposed [59, 60, 61] to enhance and tailor both thermal and electrical properties of bulk thermoelectric materials. Arguably, the electronic mean free path is orders of magnitude shorter than that of phonons. Thus in first approximation, no clear effect in the measured electronic properties is expected for up-to-date Bi_2Te_3 available nanostructures with diameter in around 40 nm [62]. We have investigated the crystallinity and lattice dynamics of a 80% ^{125}Te enriched Bi_2Te_3 nanowire array embedded in an amorphous alumina membrane with pore diameter of 50 nm. Similar studies on nanowires are dealing only with the optical phonons at the Γ -point

of the Brillouin zone. They vary depending on the experimental conditions [63, 64] and have been partially interpreted by Wang et al [65]. Nevertheless, due to complexity of handling and the limited amount of material, scattering methods were confined only to surface studies until now, e.g. using electrons. Diffraction using synchrotron radiation was performed on two perpendicular directions relative to the nanowire ensembles. In case the incident beam is parallel to the nanowires the diffraction pattern appears isotropic indicating random rotational freedom of the NWs in the template pores. In this case the data were successfully refined and all structural parameters are in agreement with the corresponding of bulk Bi_2Te_3 . However, in case the incident beam is aligned perpendicular to the NWs highly anisotropic azimuthal evolution is observed. The crystallographic c -axis, represented by the $(0\ 0\ 1)$, is almost normal -within 5 deg- to the NW axis. Symmetry forbidden reflections indicative of basal twinning exist and were further investigated and identified by TEM diffraction on single NWs. On the same nanowires, in the same two perpendicular orientations lattice dynamics properties were studied using nuclear resonance inelastic scattering. The extracted ^{125}Te projected DPS and a comparison with the corresponding DPS in bulk Bi_2Te_3 are shown in Chapter 4. When the NW appear crystallographically isotropic the DPS of NW and bulk material are almost the same. However, a deviation is observed in the low energy regime, indicative of acoustical softening. In the other orientation a significant difference in the optical phonons, around $100\ \text{cm}^{-1}$ is observed which is attributed to the preferred crystal orientation in this direction. To our knowledge, the speed of sound on nanowires was extracted for the first time. For 50 nm diameter wire, the speed of sound was reduced by about 29% as compared to bulk Bi_2Te_3 . To complete our knowledge, similar studies have been performed on Bi_2Te_3 based nanocomposites, which could not be included in this work.

Phonon confinement is one of the successful ways in phonon engineering for reducing the lattice thermal conductivity, however, it is not the only possibility. Atomic delocalization expressed either in atomic tunnelling [66] or rattling [67] give rise to reduction of thermal conductivity and is widely used in related applications. In this context we have studied the structure, see Fig. 13, and lattice dynamics of EuTiO_3 . Although EuTiO_3 is relatively high-priced for present practical applications it appears to be a model system for lattice dynamical investigations. The simplicity of the structure together with the theoretically predicted lattice dynamics instabilities gave us the opportunity to investigate the structural properties on EuTiO_3 using neutron diffraction at different temperatures. The diffraction patterns obtained on a polycrystalline sample versus temperature reveal no irregularity. A Fourier map study in the vicinity of Eu has been performed using a fourth order Gram-Charlier expansion for anisotropic displacement [19] and a Eu probability density

map was created. In Chapter 5, a section of the obtained probability density function along the cubic a direction for several temperatures is illustrated. These sections reveal that at 180 K the atomic potential exhibits off-centering by 0.2 \AA , however, at elevated temperatures the boundary potential on the Eu atomic sites is almost flattened at 320 K. Macroscopic measurements of the heat capacity and resonant ultrasound spectroscopy [68] were carried out. In the former, no irregularity has been observed down to 10 K. However, a giant acoustical softening, by 30%, was extracted from the latter upon cooling, between 100 and 300 K. This study highlights the potential of macroscopic measurements like resonant ultrasound spectroscopy.

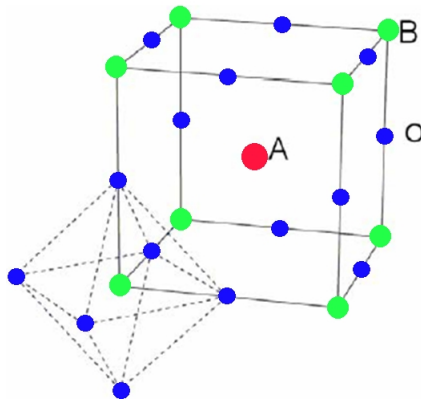


Figure 13: The perovskite structure in which EuTiO_3 crystallises. The A site are occupied by Eu atoms, the B sites by Ti atoms. Oxygen atoms are located at O sites.

Further research on the development of a resonant ultrasound spectrometer dedicated to small-sized samples as well as thin films has been carried out in parallel. We were successful in measuring the elastic constants with sub-percentage accuracy on polycrystalline samples as well as oriented single crystals down to 1 mm^3 versus temperature. As proof of principle, we performed measurements on GaAs oriented single crystals between 100 and 300 K. The results presented in Chapter 7 are in excellent agreement with previously measured elastic constants on similar samples [69].

Part I

THERMODYNAMICS AND LATTICE DYNAMICS

LATTICE DYNAMICS IN BULK BISMUTH TELLURIDE AND ANTIMONY TELLURIDE

The lattice dynamics in Bi_2Te_3 and Sb_2Te_3 were investigated both microscopically and macroscopically using ^{121}Sb and ^{125}Te nuclear inelastic scattering, x-ray diffraction, and heat capacity measurements. In combination with earlier inelastic neutron scattering data, the element specific density of phonon states was obtained for both compounds and phonon polarization analysis was carried out for Bi_2Te_3 . A prominent peak in the Te specific density of phonon states at 13 meV, that involves mainly in-plane vibrations, is mostly unaffected upon substitution of Sb with Bi revealing vibrations with essentially Te character. A significant softening is observed for the density of vibrational states of Bi with respect to Sb, consistently with the mass homology relation in the long wavelength limit. In order to explain the energy mismatch in the optical phonon region a $\sim 20\%$ force constant softening of the Sb-Te bond with respect to the Bi-Te bond is required. The reduced average speed of sound at 20 K in Bi_2Te_3 , 1.75(1) km/s, compared to Sb_2Te_3 , 1.85(4) km/s, is not only related to the larger mass density but to a larger Debye level. The observed low lattice thermal conductivity at 295 K, 2.4 W/m/K for Sb_2Te_3 and 1.6 W/m/K for Bi_2Te_3 , cannot be explained by the rather modest Grüneisen parameters, 1.7(1) for Sb_2Te_3 and 1.5(1) for Bi_2Te_3 without accounting the reduced speed of sound and more importantly the low acoustic cut-off energy.

2.1 INTRODUCTION

Binary pnictide chalcogenides with tetradymite crystal structure are semiconductors, with a typical band gap $E_g < 1$ eV, and have been long studied mainly for potential thermoelectric applications as they exhibit a large thermoelectric figure of merit, $ZT \sim 1$, close to room temperature [70]. Recently, reversible phase switching from a crystalline to an amorphous phase induced by temperature or electric field [54, 53] was reported. Because the phase change is accompanied by a large resistance change, such materials are considered candidates for future nonvolatile memory applications [71]. Furthermore, Bi_2Te_3 and Sb_2Te_3 as well as related compounds [72] are predicted to be three dimensional topological insulators where the role of spin-orbit interaction [73] is important, and the topological insulator behaviour of these materials has been experimentally established [74, 75]. Lately, combined theo-

retical and experimental studies under extreme conditions were reported by Vilaplana et al. [76] on similar compounds pointing out the importance of lattice dynamics in this series of compounds.

Both Bi_2Te_3 and Sb_2Te_3 exhibit a layered rhombohedral lattice structure ($R\bar{3}m$, #160) with three quintuple $-\text{Te(I)-Pn-Te(II)-Pn-Te(I)}-$ stacks, where $\text{Pn} = \text{Bi}$ or Sb , forming a unit cell. The parenthetical indices, Te(I) and Te(II) , denote two types of differently bonded tellurium atoms. Te(II) is coordinated nearly octahedrally by Pn atoms. In addition Te(I) has three Pn and three Te(I) as nearest neighbors and the coordination has not exactly octahedral geometry. The easy cleavage of these compounds perpendicular to c -axis is due to weak binding between the $-\text{Te(I)} \cdots \text{Te(I)}-$ nearest neighbors [56]. The observed unit cell elongation, $c/a^{\text{Bi}_2\text{Te}_3} = 6.95$, see room temperature lattice parameters given in Table 2, is indicative of a large structural anisotropy, which was reported also for the electrical properties [77]. Apart from transport anisotropy, layered compounds often also exhibit elastic anisotropy.

Several experimental techniques are specialised on the study of lattice dynamics [78, 79]. However, access to the full Density of Phonon States, DPS, is feasible only by inelastic neutron [80] or x-ray scattering [81]. For most chalcogenides, due to structural complexity and formation of antisite defects, discussed e.g. in Ref. [82], it is rather difficult to grow large single crystals for measuring phonon dispersion curves. Therefore, we have studied the density of phonon states by Nuclear resonant Inelastic Scattering, NIS. The NIS technique requires a Mössbauer active isotope and meV monochromatised synchrotron radiation of the corresponding nuclear resonant energy and provides the isotope specific, projected DPS [43]. Both Sb and Te have Mössbauer active isotopes, ^{121}Sb and ^{125}Te , respectively, however, no Bi Mössbauer active isotope exists.

Herein, we report both on the macroscopic characterization of Bi_2Te_3 and Sb_2Te_3 based on heat capacity measurements and on the microscopic characterization by synchrotron radiation diffraction and ^{121}Sb [83] and ^{125}Te [84] NIS. The combination of the Te DPS measured by NIS and the total DPS measured by inelastic neutron scattering [85] in Bi_2Te_3 allows us to obtain an approximative Bi DPS and to perform an elemental comparison for both compounds. Phonon polarization analysis was carried out on a Bi_2Te_3 single crystal measured with the incident radiation parallel and perpendicular to the c -axis. Clues to the low thermal conductivity related to the acoustical cut-off and experimental insight on the difference in the nature of the elemental binding between Bi_2Te_3 and Sb_2Te_3 are obtained.

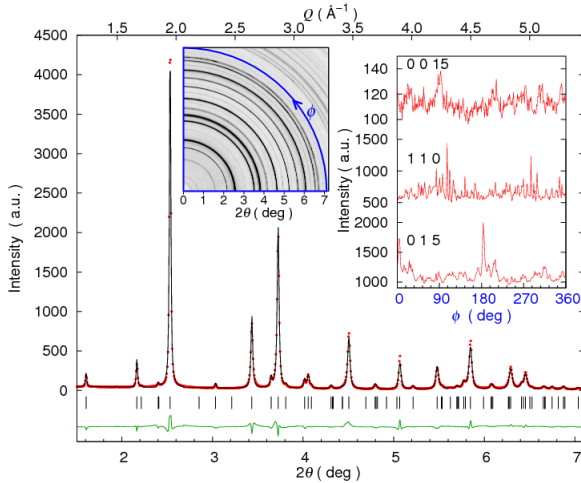


Figure 14: X-ray diffraction pattern of $\text{Bi}_2^{125}\text{Te}_3$ obtained at 295 K using synchrotron radiation (red dots), the expected peak positions (black ticks), the corresponding refinement (black line) obtained using Fullprof [40] and the difference plot (green line). Inset: (left) a quarter of the corresponding detector image, (right) intensity distribution along the ϕ angle for the (0 1 5), (1 1 0) and (0 0 15) reflections in the pseudohexagonal setting.

2.2 EXPERIMENTAL METHOD

The nuclear inelastic signal for both Bi_2Te_3 and Sb_2Te_3 can be enhanced by enrichment with ^{125}Te . No further enrichment is required¹ for ^{121}Sb . The enriched samples were prepared by sealing stoichiometric amount of reactants, Sb or Bi and ^{125}Te metal with 95% enrichment, in a quartz tube under argon atmosphere and heated up to melting temperature. The sealed melt was then left to cool down under ambient conditions. The resulting amount was 50 mg of $\text{Bi}_2^{125}\text{Te}_3$ and 10 mg of $\text{Sb}_2^{125}\text{Te}_3$. Following the same procedure Bi_2Te_3 and Sb_2Te_3 with natural isotopic abundance were prepared.

Synchrotron radiation diffraction was performed at the 6-ID-D station of the Advanced Photon Source, at 295 K, on the isotopically enriched $\text{Sb}_2^{125}\text{Te}_3$ and $\text{Bi}_2^{125}\text{Te}_3$. The wavelength was 0.142519 Å. Data was collected using an amorphous Si area detector of 2048 × 2048 pixels (pixel size: 200 μm). The sample-detector distance of 1715.5 mm was refined by using diffraction from

¹ The natural abundance of ^{125}Te and ^{121}Sb is 7% and 57% respectively

NIST Si 470c. The thermal expansion coefficient on the natural abundance Sb_2Te_3 and Bi_2Te_3 was measured using a calibrated Huber G670 image plate powder diffractometer.

Table 2: Refinement parameters (pseudo-hexagonal notation) for $\text{Sb}_2^{125}\text{Te}_3$ and $\text{Bi}_2^{125}\text{Te}_3$ at 295 K. a) obtained from Ref. [58] on Sb_2Te_3 , b) obtained from Ref. [86] on Bi_2Te_3 .

	$\text{Sb}_2^{125}\text{Te}_3$	$\text{Bi}_2^{125}\text{Te}_3$
Bragg R-factor (%)	8.6	5.0
R_f (%)	10.6	4.5
a (Å)	4.2691(1)	4.3843(1)
	4.264(1) ^a	4.3835(3) ^b
c (Å)	30.4650(1)	30.4887(1)
	30.458(1) ^a	30.487(1) ^b
ρ (g/cm ³)	6.488(5)	7.857(5)

The lattice dynamics were investigated by means of ^{121}Sb and ^{125}Te NIS using a backscattering sapphire single crystal monochromator [45] with a resolution of 1.1 meV and 1.3 meV for, 35.49 keV, ^{125}Te and, 37.13 keV, ^{121}Sb resonances respectively. The spectra were recorded in 16-bunch mode at the nuclear resonance station ID22N [87] of the European Synchrotron Radiation Facility. The samples containing ~ 10 mg of fine powder, evenly distributed on an area of 3 by 5 mm², were covered with aluminised mylar tape. In addition, for consistency check similar measurements have been performed on a small non-enriched single crystal of Bi_2Te_3 . Measurements on the single crystal carried out in two orientations, perpendicular and parallel to the crystallographic c -axis. The obtained statistics were reduced compared to enriched polycrystalline samples but satisfactory to extract the DPS. Temperature dependent measurements using ^{121}Sb and ^{125}Te NIS are not feasible due to low Lamb-Mössbauer factor, see Table 3 and the related enhanced multiphonon contribution [88]. Thus, in order to minimise multiphonon contribution the measurements were carried out at 20 K.

Heat capacity measurements on phase pure Bi_2Te_3 and Sb_2Te_3 were performed using the relaxation method of the Quantum Design (QD-PPMS) calorimeter between 3 and 300 K

2.3 RESULTS

2.3.1 Microscopic Characterization

X-ray diffraction on $\text{Bi}_2^{125}\text{Te}_3$, see Fig. 14, and on $\text{Sb}_2^{125}\text{Te}_3$, not shown, is indicative of a rhombohedral lattice, space group $R\bar{3}m$. The inset to Fig. 14 shows the Debye-Scherrer rings recorded using the area detector. No reflections from secondary phases are observed. In the same figure, the intensity distribution along the ϕ angle of the area detector is given. The $(1\ 1\ 0)$, $(0\ 1\ 5)$ and $(0\ 0\ 15)$ reflections² reveal somewhat inhomogeneous azimuthal intensity distribution which indicates slight preferential orientation. The preferred orientation was refined by the March - Dollase multiaxial function [89] with the assumption that the preferred orientation planes were the $(1\ 1\ 0)$, $(0\ 1\ 5)$ and $(0\ 0\ 15)$. The March-Dollase coefficients, r , that characterise the magnitude of the preferred orientation were 0.61, 0.68 and 1.69 respectively; random oriented powder samples have $r = 1$. Moreover, the extracted r coefficients indicates that the $(1\ 1\ 0)$ reflections have maximum pole density separated by 90° from the maximum pole density of the $(0\ 0\ 15)$ reflections. This observation is expected for crystalites of the same symmetry. After the correction, the parameters obtained at 295 K by refining the data using Fullprof [40] are given in Table 2. The lattice parameters of the ^{125}Te enriched samples appear increased by $\sim 0.1\%$ with respect to non enriched samples. However, within our instrumental resolution, $\frac{\Delta d}{d} \sim 5.0 \cdot 10^{-3}$, claims on the isotopic effects [90] in the unit cell volume cannot be drawn. All in all, the lattice parameters obtained in this study are in good agreement with literature values [86, 58].

A temperature dependent diffraction study on Bi_2Te_3 and Sb_2Te_3 was carried out for comparison and the refined lattice parameters are given in Fig. 15. Linear thermal expansion is observed between 200 and 300 K for both compounds. The volume thermal expansion coefficient, α_V , depends on the directional thermal expansion α_a and α_c by $\alpha_V = 2\alpha_a + \alpha_c$. The thermal expansion coefficients, α_a and α_c , were obtained from the derivative, $\alpha_a = (da(T)/dT)/a(300\text{ K})$, of the lattice parameter a and the corresponding expression for c . The extracted volume thermal expansion coefficient, α_V , of Bi_2Te_3 between 200 and 300 K is, $5.2 \cdot 10^{-5}\text{ K}^{-1}$, in excellent agreement with reference data [91]. In Sb_2Te_3 , we obtain a volume thermal expansion coefficient, $\alpha_V = 7.1 \cdot 10^{-5}\text{ K}^{-1}$, in agreement with the previously measured [92] thermal expansivity.

The nuclear inelastic scattering spectra from ^{125}Te and ^{121}Sb in $\text{Bi}_2^{125}\text{Te}_3$ and $\text{Sb}_2^{125}\text{Te}_3$ together with the time integrated Nuclear Forward Spectrum, i.e. the instrumental function, are depicted in Fig. 16. In this work the instru-

² the reflections are given in the pseudohexagonal notation

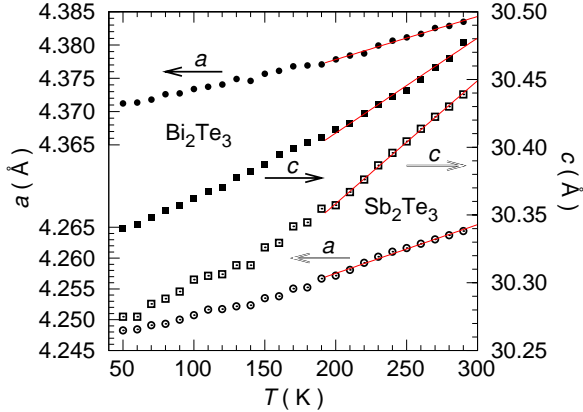


Figure 15: The temperature dependence of the a (circles) and c (squares) lattice parameters for Sb_2Te_3 (open tics) and Bi_2Te_3 (filled tics) between 50 and 300 K. Pointsize defines errorbar. The linear thermal expansion above 200 K in both orientations is indicated by red lines.

mental resolution was improved to 1.1 meV for ^{125}Te and 1.3 meV for ^{121}Sb with respect to 6.5 and 4.5 meV in the first demonstration of ^{125}Te and ^{121}Sb NIS [84, 83], respectively. After subtraction of the elastic peak, a modified version³ of the program DOS [51] was used to extract the density of phonon states. The reliability of the procedure was verified using the conventional sum rules [50]. The obtained Sb and Te partial DPSs are shown in Fig. 18. A validity check was performed in Sb_2Te_3 where the partial Sb and Te DPSs were obtained by NIS and a total generalised DPS was measured by inelastic neutron scattering [85]. The agreement of the DPS measured using NIS at 20 K after neutron weighting⁴ and the DPS measured using neutrons [85] at 77 K is substantial, see Fig. 17. In analogy, the procedure followed in extracting the Bi contribution in Bi_2Te_3 consists in subtracting the neutron weighted Te contribution measured using NIS on Bi_2Te_3 at 77 K from the total DPS measured using neutrons [85]. The obtained Bi DPS is shown in Fig. 18.

Phonon modes at Γ point in Sb_2Te_3 have been calculated from first principles [93] and observed experimentally using Raman scattering measurements as well as IR spectroscopy [94]. The even g -modes are Raman active and odd

³ The DOS program was modified for reconvoluting the extracted DPS with a gaussian function with the same FWHM as the measured time integrated NFS

⁴ In order to compare the DPS acquired using nuclear inelastic spectroscopy and the corresponding using neutrons the correct weighting factor should be applied. In first approximation, the neutron weighted DPS, $g_n(E)$ is given by $g_n(E) = \sum_i N_i g_i b_c^2 i / M_i$ where N_i is the number of atoms, $b_c^2 i$ is the nucleus specific coherent neutron scattering length and g_i is the element projected DPS

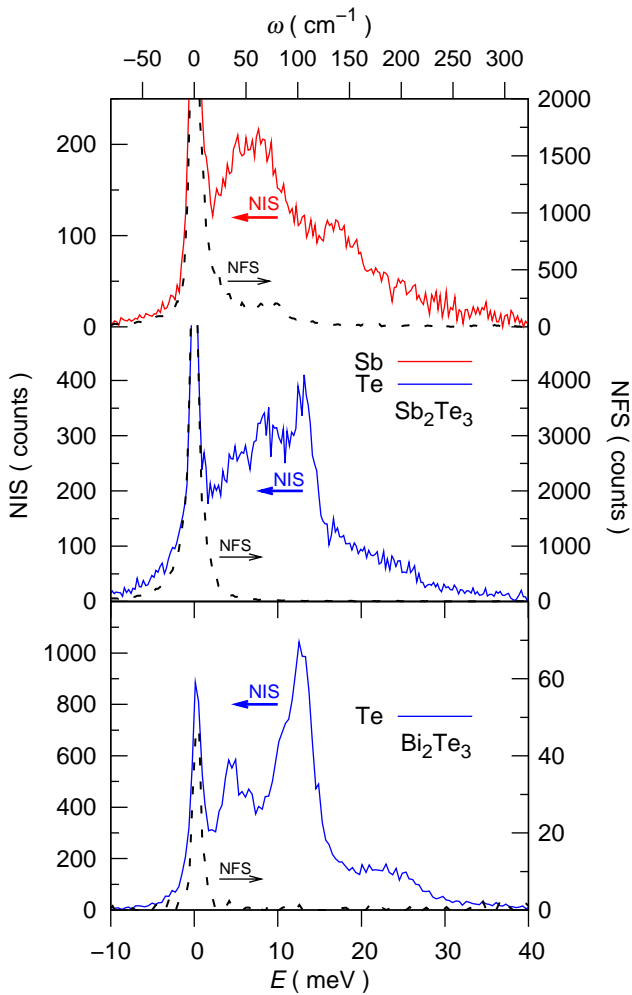


Figure 16: The Nuclear Inelastic Scattering, NIS, spectra (lines) and the time integrated nuclear forward scattering, NFS-instrumental function, (dashed lines) obtained with the ^{125}Te (blue lines) and the ^{121}Sb (red line) resonances on $\text{Bi}_2^{125}\text{Te}_3$ and $\text{Sb}_2^{125}\text{Te}_3$.

u-modes are IR active. Color tics denote the main elemental contribution to the specific mode. The mode $E_u(3)$ and the mode $A_{2u}(2)$ correspond to pure Te displacement. The displacement in the former is in the $a - b$ plane the displacement in the latter is along the c -axis. In contrast, the $A_{2u}(3)$ and $A_{1g}(2)$ modes are dominated by Sb displacements along the c -axis. A signature of all Γ point phonon modes is visible in the DPS due to enhanced resolution, see Fig. 17.

In NIS, the absorption probability depends on the orientation of the incident radiation relative to atomic vibrations and only the vibrational component along the incident beam is probed. Thus, in anisotropic crystal structures, provided that a single crystal is available, NIS is able to measure the different polarisation of phonon modes [95]. Orientation dependent measurements have been performed on a Bi_2Te_3 single crystal in two orientation, parallel and perpendicular to the crystallographic c -axis and the extracted Te DPS in both cases is shown in Fig. 19. In case the incident beam is parallel to the c -axis, a main peak around 14 meV arises in the Te DPS. This peak is identified as the $A_{2u}(2)$ phonon mode which involves vibrations only along the c -axis. When the incident beam is perpendicular to c -axis this $A_{2u}(2)$ mode does not appear in the Te DPS. Instead, a peak around 12.5 meV emerges and is identified as the $E_u(3)$ mode, which involves only in-plane atomic vibrations. The Debye level in both orientations is approximately equal, within 5%, and is shown as inset to Fig.19. In addition, the first local minimum in the orientation dependent DPS is observed around 5(1) meV for radiation parallel and around 7(1) meV for radiation perpendicular to c -axis. The isotropic DPS has been calculated from the directional dependent DPSs by averaging both contributions according to $\text{DPS}_{\text{avg}} = (2\text{DPS}_{k_{in}\perp c} + \text{DPS}_{k_{in}\parallel c})/3$ and is shown in Fig. 19. Although the obtained statistics in the non-enriched single crystal were reduced the isotropic DPS extracted from such measurements is in very good agreement with the DPS extracted from polycrystalline enriched samples.

NIS [96] is based on the Mössbauer effect and the probability of the recoilless absorption, known as Lamb - Mössbauer factor, f_{LM} , reveals the purely incoherent mean square atomic displacement parameter, ADP, $\langle u^2 \rangle = -\ln f_{\text{LM}}/k^2$, where k the wavenumber of the resonant photons. The extracted f_{LM} and ADP for both Te and Sb atoms as well as the Te orientation dependence in Bi_2Te_3 crystal are given in Table 3.

From the DPS a series of thermodynamical parameter are obtained from weighted integrals. The element specific Debye temperature is obtained directly from DPS using the expression $\theta_D^2 = 3/(k_B \int_0^\infty g(E) dE/E^2)$ valid in the high temperature limit. The obtained Debye temperature for Te is 157(1) K for both compounds, significantly larger than 135(1) K obtained for Sb in Sb_2Te_3 . The element specific mean force constants, $\langle F_i \rangle$, are obtained from

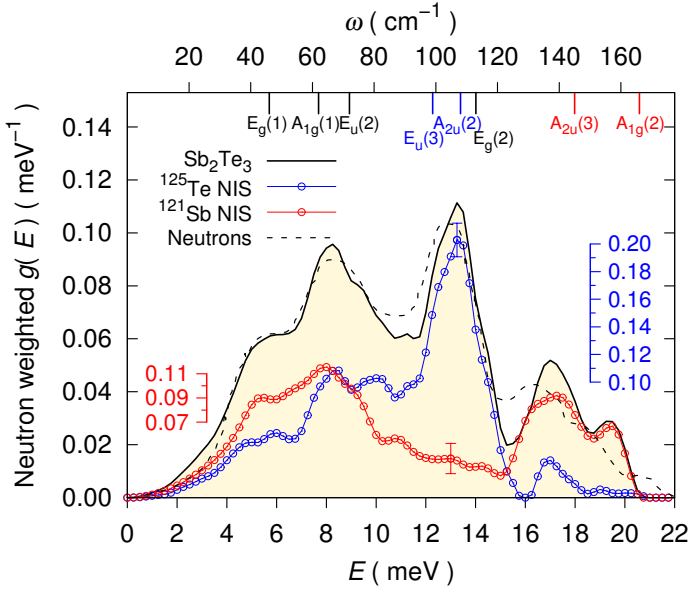


Figure 17: Density of Phonon States measured with the ^{125}Te (blue points) and ^{121}Sb (red points) resonance at 20 K on Sb_2Te_3 , for clarity line between points and typical errorbar is given. Comparison of the neutron weighted DPS of Sb_2Te_3 obtained with NIS (highlighted area), see text, with the one obtained using neutrons [85] (dashed line). Calculated [93] Γ -point phonon mode energies and symmetries are indicated by the labeled ticks.

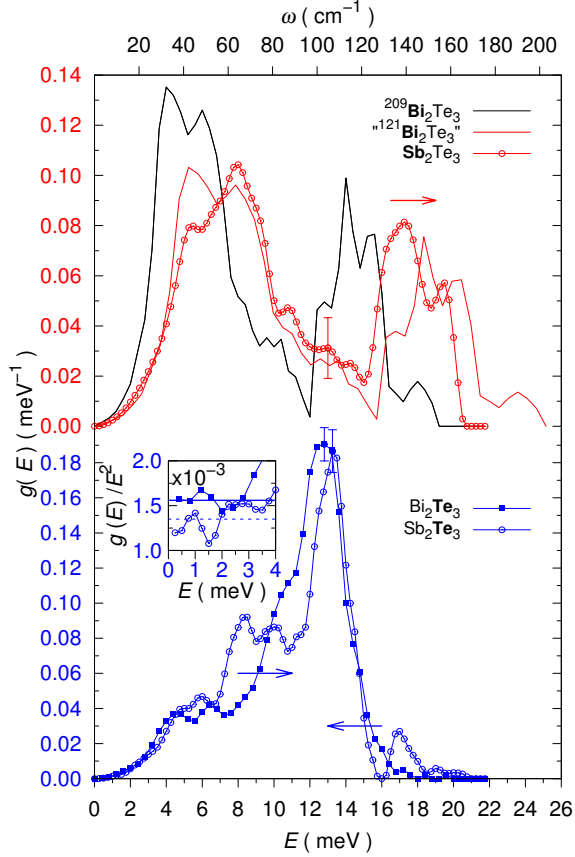


Figure 18: Element specific, Sb or Bi (red tics) and Te (blue tics), density of phonon states in Sb_2Te_3 (open circles) and Bi_2Te_3 (filled circles). The Bi specific DPS was extracted from the combination of NIS and reference neutron data [85] (black line) and renormalisation according to homology relation was applied (red line). Inset shows the Debye level calculated from the Te specific DPS measured in Sb_2Te_3 and Bi_2Te_3 .

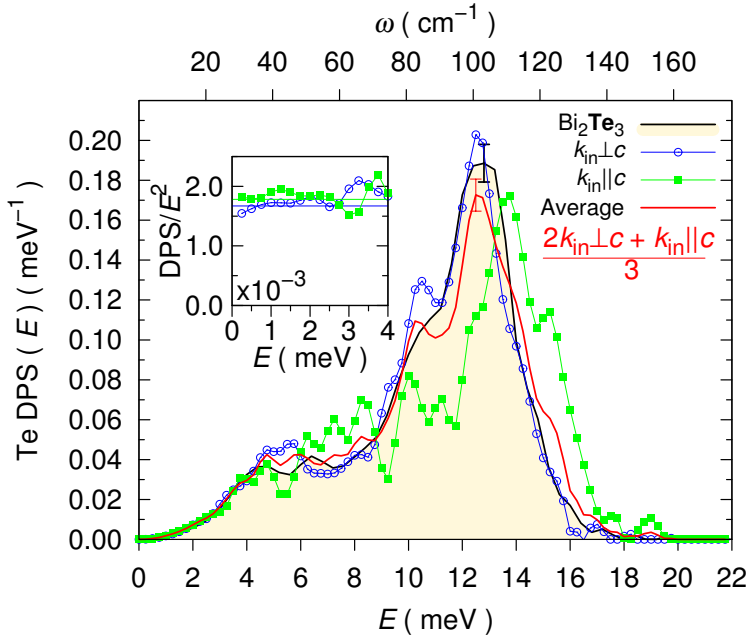


Figure 19: Orientation dependent Te DPS measured on a Bi_2Te_3 single crystal parallel (green squares), and perpendicular (blue circles), to the crystallographic c -axis. A comparison of the measured Te DPS in a Bi_2Te_3 polycrystalline sample (black curve) with the isotropic average obtained from data measured on single crystal (red curve) is given. Inset: Debye level calculated in the two orientations (solid lines) from the measured Te specific DPS.

the expression $\langle F_i \rangle = M_i \int_0^\infty g(E) E^2 dE / \hbar^2$ where M_i is the mass of the resonant isotope. The obtained values are 61(1) N/m for ^{125}Te and 55(2) N/m for ^{121}Sb in $\text{Sb}_2^{125}\text{Te}_3$ and 58(1) N/m for ^{125}Te in $\text{Bi}_2^{125}\text{Te}_3$. In addition, the force constants parallel and perpendicular to the c axis extracted from similar measurements on a single crystal are given in Table 3. The heat capacity at constant volume, $C_V(T)$, is also obtained from the total DPS using $C_V(T) = k_B \int_0^\infty g(E) \frac{(\beta E)^2 \exp(\beta E)}{(\exp(\beta E) - 1)^2} dE$, where $\beta = 1/k_B T$, in the rigid phonon approximation [10]. In Sb_2Te_3 where both Sb and Te contributions are available the obtained C_V is given in Fig. 20.

The average speed of sound, v_S , was extracted from the ^{125}Te Debye level, $\lim_{E \rightarrow 0} \frac{g(E)}{E^2}$, shown in the inset of Fig. 18, using $\lim_{E \rightarrow 0} \frac{g(E)}{E^2} = \frac{M_i}{2\pi^2 \hbar^3 \rho v_S^3}$ [90] where ρ the mass density, and given in Table 4.

2.3.2 Macroscopic Characterization

The measured specific heat at constant pressure, C_P , of natural isotope abundant Sb_2Te_3 and Bi_2Te_3 between 3 and 300 K is shown in Fig. 20. The obtained C_P in Bi_2Te_3 approaches smoothly the Dulong-Petit limit, $124.5 \text{ Jmol}^{-1} \text{ K}^{-1}$ close to room temperature. In contrast, in Sb_2Te_3 the measured C_P deviates linearly from the Dulong-Petit limit between 230 and 300 K by $0.038 \pm 0.009 \text{ Jmol}^{-1} \text{ K}^{-2}$, indicating internal degrees of freedom related either to electronic properties or enhanced anharmonicity. In addition, a simple fitting of the measured C_P data in Sb_2Te_3 and Bi_2Te_3 with a model of a collection of Einstein oscillators embedded in a Debye solid gives Einstein temperatures around 55 K, see Table 4, for both compounds. This model does, however, fail to reproduce adequately the experimental data below 30 K. We have modelled this deviation using a Schottky [97] model for a two level system. The contribution in the specific heat of such two level system is given by $C_S \left(\frac{\theta_S}{T}\right)^2 \exp(\frac{\theta_S}{T}) / [1 + \exp(\frac{\theta_S}{T})]^2$ where C_S the Schottky heat capacity prefactor and θ_S is the Schottky temperature. After the introduction of these two additional free parameters a reduction of the reduced χ^2 from 462 to 3 was achieved. The resulting fit, between 3 and 80 K, as well as the Schottky contribution is shown in the inset to Fig. 20. The nature of the Schottky term was further investigated. In the literature Schottky anomalies in the specific heat have been reported in paramagnetic salts [?] and heavy fermion systems [22] as well as in amorphous systems [98] and systems with artificially created defects [99]. In all cases, Schottky anomalies arise at low temperatures, moreover, in magnetic systems the related Schottky parameters have a magnetic field dependence [100]. Heat capacity measurements with a 4 T applied magnetic field revealed no modification in heat capacity and

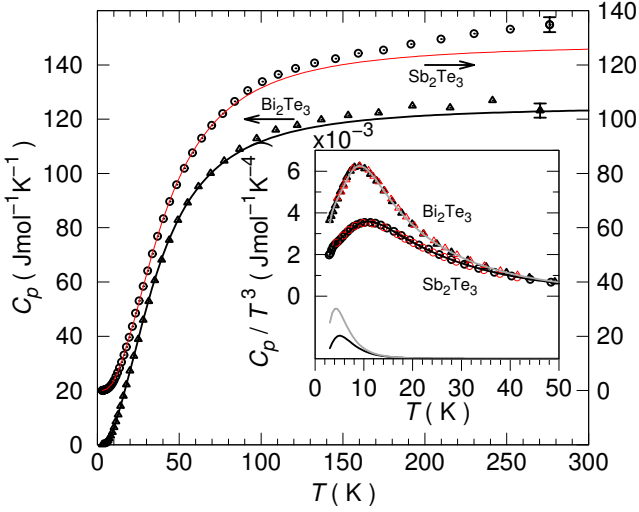


Figure 20: Specific heat at constant pressure, C_p , data measured on Sb_2Te_3 (circles) and Bi_2Te_3 (triangles) between 3 and 300 K and heat capacity at constant volume, C_V , calculated from low temperature DPS (red line). A typical errorbar is given. Inset: the Debye representation, C_p/T^3 , of both measurements. A fit of the experimental data was applied using a two level Schottky model superimposed to a Debye model with embedded Einstein oscillators (solid lines). The contribution of the Schottky model is given in the lower part of the inset. Specific heat measurements under 4 T magnetic field are shown as red symbols.

no change in the Schottky contribution. The additional states concentration attributed to the Schottky term was calculated from the prefactor C_S given in Table 4, with respect to the total thermodynamical degrees of freedom $C_D + C_E$. In Bi_2Te_3 the additional states amount to 0.9% and in $\text{Sb}_2^{125}\text{Te}_3$ to 0.6% of the total thermodynamical degrees of freedom.

2.4 DISCUSSION

In this study, the calculated discrepancies between natural abundant Te, 127.60 amu, and our enriched ^{125}Te , 125 amu, according to the mass rule $\theta_D \sim M_i^{-1/2}$, where M_i is the isotopic mass, are in the range of experimental error, namely 0.8%, and isotopic effects are neglected in what follows.

The Te projected DPS in Sb_2Te_3 and Bi_2Te_3 shown in Fig. 18, bottom, include a prominent peak, at 13 meV, which dominates the total DPS, and

does not shift perceptibly upon substitution of Bi by Sb which indicates pure Te vibrations. This was previously indirectly identified by a series of inelastic neutron experiments on powder samples [85] and shown in theoretical calculations [93, 58]. Below 30 cm^{-1} a minor discrepancy between the tellurium DPSs in Sb_2Te_3 and Bi_2Te_3 is observed and is related to the low lying transverse acoustical phonons. Together with the increased mass density of Bi_2Te_3 with respect to Sb_2Te_3 , see Table 2, an 8% increase in the speed of sound in Sb_2Te_3 as compared to Bi_2Te_3 is obtained. Pronounced differences in the Te specific DPS between 60 and 110 cm^{-1} , $E_u(2)$ modes, as well as between 130 and 150 cm^{-1} , $A_{2u}(3)$ and $A_{1g}(2)$ modes, are seen in the two studied compounds. The aforementioned modes have contribution both from Sb and Te, as seen from the Fig. 18, and this might be the reason for the observed differences in the Te specific DPSs. In contrast, the comparison of the Sb and Bi DPSs reveal significant softening for the Bi compound which is explained partly by the larger mass of the Bi atoms. Assuming the same electronic structure, a homology relation [101] can be applied to describe the mode energy difference $E_{\text{Sb}}/E_{\text{Bi}} = \sqrt{(M_{\text{Bi}}a_{\text{Bi}}^2) / (M_{\text{Sb}}a_{\text{Sb}}^2)}$. The mass ratio $\sqrt{M_{\text{Bi}}/M_{\text{Sb}}} = 1.66$ and the lattice constants ratio $a_{\text{Bi}}/a_{\text{Sb}} = 1.000$ or 1.027 for c and a , respectively, yield $E_{\text{Sb}}/E_{\text{Bi}} = 1.31$ or 1.35 . The Bi DPS, scaled by 1.33 and renormalised to unity area is shown in Fig. 18, top, as “ $^{121}\text{Bi}_2\text{Te}_3$ ”. Such scaling is sufficient to describe the change in the low energy part of the DPS. It is, however, too large to describe the change observed in the highest energy optical part where a scaling factor of 1.25 would have to be used. This difference must be ascribed to a $\sim 20\%$ softening in force constant of Sb in Sb_2Te_3 as compared to Bi in Bi_2Te_3 . The simultaneous stiffening of the low-energy acoustical phonons which results in increased speed of sound and the softening of the high-energy optical phonons which results in reduced force constants is a unique characteristic of phase change materials [102]. This behaviour is observed here upon substitution of Bi with Sb and might be related to more favourable phase switching behaviour in antimony than in bismuth bearing chalcogenides [103]. At the atomic scale it might be related to the resonance bonding which is highlighted in phase switching applications. Similar effect in the DPS, i.e. rescaling of the high energy optical phonons, might arise due to preferred orientation of the sample under investigation. However, the good correspondence of our measured element specific DPS using NIS with theoretical calculations as well as with reference data measured on polycrystalline material using neutrons preclude this explanation.

Macroscopic experimental techniques usually deal with integrals of microscopic quantities, among them, heat capacity measurements were used. From the low temperature data, see inset to Fig. 20, in Bi_2Te_3 and Sb_2Te_3 the

Table 3: Summary of the lattice dynamics parameters, Lamb-Mössbauer factor, f_{LM} , mean square atomic displacement, $\langle u^2 \rangle$, mean force constants, $\langle F_i \rangle$, obtained in this study at 20 K.

Compound	Method	f_{LM}	$\langle u^2 \rangle, 10^{-3} \text{Å}^{-2}$	$\langle F_i \rangle, \text{N/m}$
Sb_2Te_3	^{125}Te NIS	0.53(1)	1.96(1)	61(2)
	^{121}Sb NIS	0.41(9)	2.52(1)	55(2)
Bi_2Te_3	^{125}Te NIS	0.52(1)	2.02(1)	58(2)
	" ^{121}Bi " or ^{209}Bi	-	-	74(2)
Bi_2Te_3 crystal	^{125}Te NIS k c	0.54(1)	1.91(1)	68(3)
	^{125}Te NIS k \perp c	0.52(1)	2.03(1)	58(3)

extracted Debye and Schottky temperature are shown in Table 4. Although the Debye temperature depends on temperature, in the crude approximation of temperature independency the extracted value agrees within 15% with the value extracted from DPS in the high temperature limit. Not surprisingly, the Debye temperature extracted from the Te specific DPS is the same for Bi_2Te_3 and Sb_2Te_3 . The Schottky temperature is practically also the same in both compounds. Several explanations regarding this Schottky anomaly in heat capacity are possible. As the compounds have no magnetisation the magnetic origin should be discarded. Similarly, assuming that the origin of the Schottky term is of electronic nature, electronic spin polarization [104] is unlikely because no dependence on magnetic field was observed. A non spin polarised electronic origin of the Schottky term can not be excluded a priori. The electronic contribution in heat capacity from activated charge carriers for semiconducting Bi_2Te_3 above 3 K is insignificant according to Shoemaker et al. [105]. The presence of defects provides a plausible explanation as defect formation is an important issue in Bi_2Te_3 . The energy scale for the existence of antisite defects has been recently calculated theoretically [82] and attempts to prove their existence experimentally [106] have been carried out. Activation of trapped charges around these antisite defects could contribute to the measured heat capacity as these charges will cause small lattice distortions. No irregularity is however observed around the expected energy, $E_{\text{Schottky}} = 1.8 \text{ meV}$, in the measured DPS of both compounds. A reasonable explanation for this lacking observation is the low states concentration, below 1% in both cases, as well as the instrumental function of $\sim 1 \text{ meV}$ full width at half maximum which hampers the observation of such small contribution that would be hidden in the tails of the elastic line. To the best of our knowledge, no direct relation of antisite defects in Bi_2Te_3 and Sb_2Te_3 with macroscopic physical properties have been reported so far. However, the relation of thermal

Table 4: Summary of the thermodynamical parameters, speed of sound, v_s , extracted from NIS at 20 K, Grüneisen parameter, γ , at 295 K, Debye Temperature, θ_D , Einstein Temperature, θ_E , Schottky Temperature, θ_S , as well as the prefactors, C_D , C_E , C_S , extracted from heat capacity measurements. a) obtained from Ref. [58], b) obtained from Ref. [58] using the Voigt and Reuss average [37] at 20 K.

Compound	Method	v_s , km/s	γ	C_D , J/mol/K	θ_D , K	C_E , J/mol/K	θ_E , K	C_S , J/mol/K	θ_S , K
Sb ₂ Te ₃	¹²⁵ Te NIS	1.90(2)	-	-	157(5)	-	-	-	-
	¹²¹ Sb NIS	-	-	-	135(5)	-	-	-	-
Bi ₂ Te ₃	Calorimetry	1.91(5)	1.7(1)	109(3)	179 (5)	18(1)	59(1)	0.9(1)	23 (1)
	¹²⁵ Te NIS	1.75(1)	-	-	157(5)	-	-	-	-
	Calorimetry	1.78(5)	1.5(1)	102(3)	164 (5)	23(1)	50(1)	1.2(1)	21 (1)
	Ultrasound	1.918 ^b	-	-	165 ^a	-	-	-	-
		1.394 ^b							

properties with artificially created defects in crystalline materials has been extensively investigated. It was shown that presence of defects give rise to Schottky anomaly in heat capacity [107]. Similar behaviour is observed in our heat capacity measurements. The two level system was proposed to interact resonantly with thermal phonons leading to the T^2 dependence of thermal conductivity [108] below the temperature at which the peak in the Schottky term of heat capacity appears. Thermal conductivity data neither on Bi_2Te_3 nor on Sb_2Te_3 were found in literature at very low temperature, $T < 5$ K. In order to clarify the existence of resonant interaction of antisite defects with thermal phonons we suggest that such thermal conductivity measurements below 5 K should be carried out.

Above 230 K a strong deviation between the measured C_P and calculated C_V is observed only in Sb_2Te_3 whereas in Bi_2Te_3 C_P approaches the Dulong-Petit limit $124.5 \text{ Jmol}^{-1} \text{ K}^{-1}$ at 295 K. Similar effects were observed close to 300 K in previous calorimetric studies on Sb_2Te_3 [109] with the temperature deviation between C_P and C_V being, $0.028 \text{ Jmol}^{-1} \text{ K}^{-2}$, in agreement with our measurement. The band gap in Sb_2Te_3 and Bi_2Te_3 is $E_g \sim 0.1 \text{ eV}$ [110]. Thus the carrier activation temperature in both compounds is ~ 1000 K. At temperatures much lower than the corresponding carrier activation energies anharmonicity effects are contributing in the specific heat expressed in the formula $C_P - C_V = \frac{\alpha_V^2 V}{K_T} T$ [10], where K_T is the isothermal compressibility. Hence, our estimation of the Sb_2Te_3 isothermal compressibility between 230 and 300 K based on our C_P measurements and our C_V calculated from the total DPS is, $K_T = 1.3 \pm 0.3 \text{ Mbar}^{-1}$, in quite poor agreement with the compressibility extracted from high pressure diffraction [111], $K_T = 3.3 \text{ Mbar}^{-1}$. Consequently, the observed deviation between C_P and C_V in Sb_2Te_3 might not have solely anharmonic origin. The excess in heat capacity close to room temperature in Sb_2Te_3 can possibly be attributed to electronic contribution due to self doping which has been highlighted in this compound [112].

Macroscopic ultrasonic techniques which focus on the study of the speed of sound on either single crystal or polycrystalline materials are widely used [68]. In this study we were not able to obtain a large macroscopically isotropic or single crystalline sample of Sb_2Te_3 and Bi_2Te_3 . However, our microscopically extracted speed of sound can be directly compared to reference data on single crystals [58] using both the Voigt and Reuss average [37]. With the Bi_2Te_3 mass density, ρ , of 7.86 g/cm^3 at 20 K the upper and lower limits in the speed of sound obtained from ultrasonic techniques on single crystals, i.e. related to isostress and isostrain conditions, are 1.918 km/s and 1.394 km/s respectively. The extracted speed of sound of this work is between the limits calculated from reference ultrasonic data. A second estimation of the speed of sound was obtained with the Debye approximation [113], $v_S = k_B \theta_D / \left(\hbar (6\pi^2 N)^{1/3} \right)$,

using our heat capacity measurements. The density of atoms for Bi_2Te_3 is $2.95 \cdot 10^{22}$ atoms/cm³ and for Sb_2Te_3 $3.11 \cdot 10^{22}$ atoms/cm³. Hence using the Debye temperature extracted from our heat capacity measurements the estimated speed of sound given in Table 4 is obtained. Not only is the speed of sound extracted from our macroscopic heat capacity measurements in excellent agreement with the one obtained from NIS but it also is largely smaller than in typical metallic systems, e.g. 3.750 km/s in Cu. Thus, in substances with layered structures, such as in Sb_2Te_3 and Bi_2Te_3 , it seems that the shear modulus related with the first peak in the measured DPS dominates the long wavelength phonon propagation and results in reduced speed of sound.

Speed of sound and heat capacity are one constituent of thermal conductivity with the other being anharmonicity. The role of disorder and anharmonicity in the thermal conductivity have been thoroughly studied in the last years [?]. To quantify the anharmonicity in Bi_2Te_3 and Sb_2Te_3 the macroscopically extracted dimensionless Grüneisen parameter, γ , that is considered as a hallmark of anharmonicity was chosen. In this study γ is defined by the formula $\gamma = \frac{\alpha_V}{C_V K_T}$ [97]. In Bi_2Te_3 the Grüneisen parameter using our measured volume expansivity, $\alpha_V^{\text{Bi}_2\text{Te}_3} = 5.2 \times 10^{-5} \text{ K}^{-1}$, with hexagonal unit cell volume $V = 507 \text{ \AA}^3$, heat capacity under constant volume $C_V = 124.5 \text{ Jmol}^{-1} \text{ K}^{-1}$ and isothermal compressibility $K_T = 2.67 \text{ Mbar}^{-1}$ [58] is $\gamma = 1.5(1)$ at 295 K. In Sb_2Te_3 from our measured expansivity $\alpha_V^{\text{Sb}_2\text{Te}_3} = 7.1 \times 10^{-5} \text{ K}^{-1}$ of the hexagonal unit cell with volume $V = 481 \text{ \AA}^3$, at 295 K, heat capacity under constant volume $C_V = 124.5 \text{ Jmol}^{-1} \text{ K}^{-1}$ and isothermal compressibility $K_T = 3.3 \text{ Mbar}^{-1}$ [111], the Grüneisen parameter is $\gamma = 1.7(1)$. Furthermore, in order to quantify anisotropic effects the orientation dependent Grüneisen parameter has been extracted on Bi_2Te_3 by modifying the orientation dependent formulas given by Barron [114] for anisotropic crystal structure [115], namely $\gamma_a = [\alpha_a(c_{11} + c_{12}) + \alpha_c c_{13}]/C_V$ along the a direction and $\gamma_c = [\alpha_c c_{33} + 2\alpha_a c_{13}]/C_V$ along the c direction. The elastic constants c_{11} , c_{12} , c_{13} and c_{33} at 280 K given by Ref. [58] are 0.685, 0.218, 0.270 and 0.477 Mbar, respectively. The direction dependent thermal expansion measured herein in the same temperature range is $\alpha_a = 1.48 \cdot 10^{-5} \text{ K}^{-1}$ and $\alpha_c = 2.30 \cdot 10^{-5} \text{ K}^{-1}$. In addition, close to room temperature all phonons in the DPS are populated, the heat capacity reaches the Dulong-Petit limit and can be considered isotropic. The estimated direction dependent Grüneisen parameters along a , $\gamma_a = 1.6(1)$, and along c , $\gamma_c = 1.5(1)$, do not deviate significantly from the average Grüneisen parameter, $\gamma = 1.5(1)$. To elucidate the impact of the Grüneisen parameter on our measured DPS both in Bi_2Te_3 as well as in Sb_2Te_3 we used the vibrational energy defined Grüneisen parameter, $\gamma = -\frac{d \ln E}{d \ln V}$. A straightforward way to change the unit cell volume is

by conducting temperature dependent studies. However, temperature dependent ^{125}Te and ^{121}Sb NIS is not feasible above 100 K. The estimated phonon mode energy shift, between 50 and 100 K using our measured $\frac{\delta V}{V} \sim 0.005$ and our extracted average Grüneisen parameter of $\gamma = 1.6$ at 295 K results in $\frac{\delta E}{E} \sim 0.008$. Therefore, even the highest energy phonon modes, around 20 meV will not shift due to anharmonicity by more than 0.2 meV. Such energy mode shift is currently within the resolution limit for ^{125}Te and ^{121}Sb NIS. The small effect of anharmonicity on the DPS is also substantiated by the correspondence of our measured DPS on Sb_2Te_3 at 20 K and the DPS obtained by neutron scattering [85] at 77 K.

An empirical expression of the thermal conductivity in the umklapp scattering limit was derived by Toberer [116], $\kappa_L = \frac{(6\pi^2)^{2/3}}{4\pi^2} \frac{\bar{M}v_s^3}{TV_{\text{at}}^{2/3}\gamma^2} \left(\frac{1}{N^{1/3}}\right)$, where V_{at} the volume per atom, \bar{M} the average atomic mass and N the number of atoms per primitive cell. Both Bi_2Te_3 and Sb_2Te_3 have 5 atoms per primitive unit cell. Bi_2Te_3 has an average atomic mass of 168.29 amu with 33.8 \AA^3 atomic volume. Sb_2Te_3 has 124.64 amu average atomic mass and 32 \AA^3 atomic volume. Accordingly, the lattice thermal conductivity in the umklapp limit for Bi_2Te_3 is 4.76 W/m/K and for Sb_2Te_3 is 3.65 W/m/K in contrast to 1.6 W/m/K and 2.4 W/m/K observed at room temperature for Bi_2Te_3 and Sb_2Te_3 [117], respectively. In our calculation the lattice thermal conductivity was extracted at room temperature but we used our measured speed of sound at 20 K. The calculated thermal conductivity in the umklapp scattering limit is not only overestimated compared to the measured thermal conductivity but it also shows that Bi_2Te_3 should have larger conductivity than Sb_2Te_3 . Thermal transport of optical branches is generally neglected because they contribute to less than 1% in the thermal conductivity. Because the Grüneisen parameter was taken into account in our estimation anharmonicity effects fail, at least in first approximation, to explain this deviation. The acoustic mode Debye temperature, θ_a , can be extracted from the calorimetry estimated Debye temperature, θ_D^{cal} , using the relation $\theta_a = N^{-1/3}\theta_D^{\text{cal}}$ [118]. The lattice thermal conductivity derived by Slack [119] is shown in Eq. 2.1.

$$\kappa_L = A \frac{\bar{M}\theta_a^3 v_{\text{at}}^{1/3} N^{1/3}}{\gamma^2 T} \quad (2.1)$$

where $A \approx 3.1 \cdot 10^{-6}$ is a collection of physical constants. In both compounds Eq. 2.1 yields a reduced thermal conductivity, namely 3.76 W/m/K in Bi_2Te_3 and 2.76 W/m/K in Sb_2Te_3 , but still lower in Sb_2Te_3 than in Bi_2Te_3 . Assuming that the only channel in thermal conduction is realised through the acoustical phonons the acoustic cut-off can alternatively be estimated by

our element specific DPS. In both compounds the tellurium contribution in the DPS is relatively smooth and does not change significantly upon substitution of Bi with Sb. The pnictide contribution, see Fig. 18, top, is more structured and indicates that the acoustical cut-off is 6(1) meV and 8(1) meV, i.e. $\theta_a = 71$ K and 94 K for Bi_2Te_3 and Sb_2Te_3 , respectively. The thermal conductivity calculated using these acoustical cut-off θ_a obtained by DPS is, 1.6(2) W/m/K for Bi_2Te_3 and 2.0(2) W/m/K for Sb_2Te_3 , in excellent agreement with reference data [117], 1.6 W/m/K and 2.4 W/m/K, respectively.

NIS on anisotropic single crystals measures the DPS of modes with vibrations along the incident beam. However, the phonon polarization and the phonon transport direction do not coincide. For example, when $k_{in} \perp c$ the probed vibrations have three components: one is coming from longitudinal modes transported along the basal plane, another one is related to transversal modes transported along the c -axis and the last is coming from transversal modes transported in the basal plane. When $k_{in} \parallel c$ the probed vibrations, one is related to longitudinal modes transported along the c -axis and two are coming from transversal modes transported in the basal plane, have one transversal mode transported in the basal plane in common with the $k_{in} \perp c$ case. The orientational dependent thermal conductivity, or equivalently the acoustic cut-off energy, can in principle be estimated from our measured orientational dependent DPS. However, the measured chalcogenide contribution in the DPS is not well structured and the acoustic cut-off energy cannot be extracted directly from the DPS. Even if the direction dependent acoustic cut-off energies were available from our measurements, special attention should be drawn in the fact that the thermal conductivity ratio $\kappa_L^{k_{in} \perp c} / \kappa_L^{k_{in} \parallel c}$ extracted from our DPS using Eq. 2.1 would not be the same with the measured lattice thermal conductivities [120], $\kappa_{L \perp c} = 1.73$ W/m/K and $\kappa_{L \parallel c} = 0.64$ W/m/K. The same holds for the composite speed of sound. Thus, in order to further clarify the orientational dependence of thermal conductivity detailed theoretical investigation are needed.

LATTICE DYNAMICS IN ELEMENTAL MODULATED ANTIMONY TELLURIDE FILMS

The lattice dynamics in an elemental modulated Sb_2Te_3 film were investigated microscopically using ^{121}Sb nuclear inelastic scattering combined with high energy synchrotron radiation diffraction. The element specific density of phonon states was extracted and the nature of the Sb - Te interlayer bond has been investigated. Comparison to earlier nuclear inelastic scattering measurements on bulk Sb_2Te_3 reveals that the main features in the Sb specific density of phonon states are coming mainly from the layered structure. The average speed of sound at 40 K, 1.74(2) km/s, is slightly decreased compared to bulk Sb_2Te_3 at 20 K, 1.78(2) km/s. The acoustic cut-off energy shows as well a decrease from 8.5 to 8 meV which is in agreement with macroscopic thermal conductivity measurements.

3.1 INTRODUCTION

Tetradymite chalcogenide compounds usually form anisotropic layered structures [121] with interesting lattice dynamics [122]. In layered unit cells, low-frequency intra-layer modes [123] were reported in which the layers move nearly as rigid units. The energy separation between the inter- and the intra-layer modes is a measure for the elastic anisotropy of the material. It is thus interesting to study the density of phonon states, DPS, on artificially created layered compounds which mimic the natural crystal structures and compare it with reference data on bulk crystalline counterparts.

Sb_2Te_3 crystallises in the tetradymite structure ($R\bar{3}m$, #160) with three quintuple $-\text{Te(I)-Sb-Te(II)-Sb-Te(I)}-$ stacks forming a unit cell. The parenthetical indices, Te(I) and Te(II) denote two tellurium sites. The easy cleavage of these compounds perpendicular to c -axis is due to weak van der Waals type binding [124] between quintuple stacks at the Te(I) - Te(I) bond.

Sb_2Te_3 has been reported as the best candidate, next to Bi_2Te_3 , for room temperature thermoelectric conversion and as the model compound for phase change applications [103]. In both cases, the layered structure is thought to lead to low thermal conductivity. For Sb_2Te_3 films the influence of stoichiometry, morphology, annealing temperature and crystallinity of the films on thermal conductivity [125] and furthermore on their thermoelectric perfor-

mance [126, 127] have been studied and the most promising results were obtained for near stoichiometric films [128].

Herein, we study the lattice dynamics and the influence of interlayer bonding on an elemental modulated Sb_2Te_3 sample prepared via the nanoalloying method [129, 130] by measuring the Sb specific density of phonon states. On the same sample, we identified diffuse x-ray scattering which indicates that in the as grown state finite correlation length in the basal plane is observable.

3.2 EXPERIMENTAL METHOD

Repeated layers of the elements Sb and Te with 0.2 nm thickness were deposited on 10×10 mm pieces of commercially available $\text{SiO}_2(100 \text{ nm})$ at Si (1 0 0) substrates in an MBE system at room temperature. All layers were deposited to maintain the stoichiometric 40/60 ratio for Sb/Te and the repeating quintuplet pattern. The nominal total thickness of the thin film was $1 \mu\text{m}$. The use of an ambient temperature substrate instead of a heated substrate prevents the re-evaporation of Te, thus facilitating stoichiometry control and enabling a fast composition screening. In addition, no epitaxial relation to the substrate is needed. The nanoalloyed films are very smooth compared to the epitaxial thin films which tend to exhibit a significant roughness [131]. The cross plane thermal conductivity at room temperature was determined using a time domain thermal reflectance measurement system [132, 133] calibrated to Si/ SiO_2 standard and the results were reported elsewhere [130].

To verify crystallinity and phase purity, diffraction using synchrotron radiation was carried out at 295 K at 6-ID-D station of the Advanced Photon Source on nanoalloyed Sb_2Te_3 films in two orientations, (i) with the incident, k_{in} , vector parallel to the Si (1 0 0), in transmission geometry, and (ii) with k_{in} perpendicular to the Si (1 0 0), in grazing incidence geometry. The wavelength was 0.142519 \AA . Data was collected using an amorphous Si area detector of 2048×2048 pixels (pixel size: $200 \mu\text{m}$). The sample detector distance of 1715.5 mm was refined by using diffraction from NIST Si 470c. Both detector patterns are interpreted as follows: the radial distance from the beam center corresponds to the scattering angle 2θ and the circular angle at certain radius corresponds to the azimuthal angle ϕ . The data raw were treated using FIT2D [134] and the modified detector patterns in azimuthal coordinates, ϕ and 2θ , are shown in Fig. 21. The one dimensional diffractograms were extracted after integrating intensities at all ϕ for certain 2θ .

The lattice dynamics were investigated by means of ^{121}Sb nuclear inelastic scattering [84], NIS, using a backscattering monochromator [45] with a resolution of 1.3 meV for the 37.13 keV ^{121}Sb resonance. The natural abundance of ^{121}Sb is 57% and no isotopic enrichment is required. The spectra

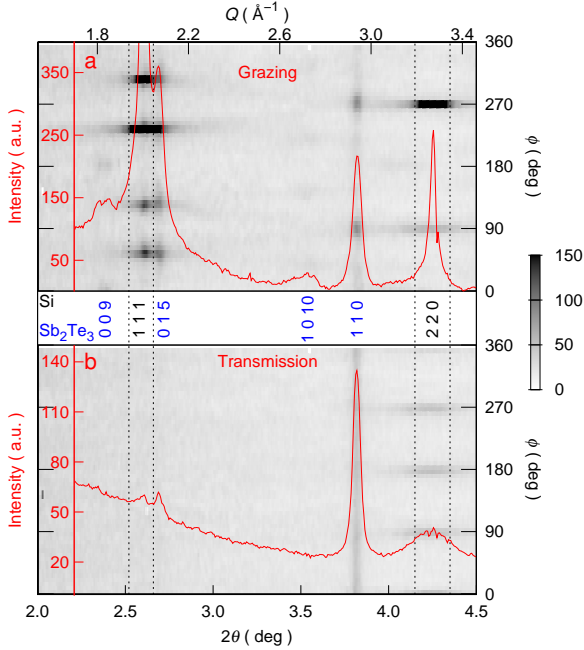


Figure 21: X-ray diffraction pattern of the elemental modulated Sb_2Te_3 film obtained at 295 K using synchrotron radiation in two orientations, see text, (a) grazing incident geometry and (b) transmission geometry. Background shows the actual detector pattern and red lines the related diffractograms. Expected peak positions are indicated by the corresponding Miller indices in pseudo-hexagonal setting.

were recorded in 16-bunch mode at the nuclear resonance station ID18 [87] of the European Synchrotron Radiation Facility on the same sample and orientation where diffraction patterns were acquired. In order to minimise multiphonon contributions the measurements were performed at 40 K. In NIS, the absorption probability depends on the orientation of the incident radiation relative to the crystallographic axes [135]. Only modes with non zero polarization projected along the beam direction are probed. The ^{125}Te DPS has not been measured because the samples are too thin to probe without isotopic enrichment, which is very challenging for this type of deposition.

3.3 RESULTS

X-ray diffraction on the nanoalloyed film shows only one homogeneous and broad Debye - Scherrer ring of the (1 1 0) type in transmission geometry, see Fig. 21b. In grazing incidence geometry broad but discrete reflections are identified not only for (1 1 0) type of reflections but also for (0 0 9) and (1 0 10). The diffuse scattering related to the (0 1 5) type of reflections appears close to the (1 1 1) reflections of the silicon substrate. All reflections were fitted with a Lorentzian profile and the extracted parameters are given in Table 5. The full width at half maximum, FWHM, of the Si (1 1 1) reflection has also been extracted and indicates the instrumental resolution. It appears that the instrumental resolution is at least three times narrower than film reflections. An estimate of the correlation length, ξ , can be extracted from the FWHM of the reflections, FWHM_{ref} , corrected for the instrumental resolution, $\text{FWHM}_{\text{inst}}$, using $1/\xi = 0.5\sqrt{\text{FWHM}_{\text{ref}}^2 - \text{FWHM}_{\text{inst}}^2}$. The correlation length extracted from all reflections is smaller than 100 Å, see Table 5. Note that the extracted correlation length for the (0 0 9) reflection is very close to the nominal layer thickness of 20 Å. Thus, although crystalline order is identified, long range crystalline order is not fully established in the elemental modulated films. An estimate of the interplane distance change, δd , was extracted by comparing the positions of the observed reflections with the nominal reflection positions of crystalline Sb_2Te_3 , see Table 5. The crystallographic c-axis related to (0 0 9) type of reflections appears elongated by $\sim 5\%$ which indicates somewhat loose packing perpendicular to the basal plane, however, all reflections which have in-plane component have lower 2θ values than their nominal positions. This indicates that the nanoalloyed Sb_2Te_3 film is slightly denser in-plane than the crystalline counterpart.

The nuclear inelastic scattering spectrum by ^{121}Sb in bulk Sb_2Te_3 have been reported earlier [136]. In this study, we used the same instrumental setup [45] and we obtained the ^{121}Sb nuclear inelastic spectra and the instrumental function, i.e. time integrated nuclear forward spectra, simultaneously in a nanoalloyed, 3 by 5 mm², Sb_2Te_3 film. The elastic line was subtracted manually and the data were further treated using a modified version¹ of the program DOS [51]. The density of phonon states were extracted from the raw spectra and all related thermodynamical parameters were extracted both from the raw data and the density of phonon states. The self consistency of the procedure was confirmed by applying the conventional sum rules [50]. The ^{121}Sb specific DPS on the nanoalloyed film, $g(E)$, was extracted only in grazing incident geometry and shown in Fig. 22c. For transmission geometry

¹ The DOS program was modified for reconvoluting the extracted DPS with a gaussian function with the same FWHM as the measured time integrated NFS

Table 5: Summary of crystallographic parameters extracted from x-ray diffraction by a nanoalloyed Sb_2Te_3 film in ^agrazing incident geometry, ^btransmission geometry and comparison with bulk Sb_2Te_3 , reflection positions are calculated from Ref. [86] using wavelength 0.142519 Å. The FWHM and the reflection position was extracted after fitting the data with a Lorentzian profile. The calculated interplane distance difference was calculated using the relation $\delta Q = (Q_{\text{film}} - Q_{\text{bulk}}) / Q_{\text{bulk}}$. The correlation length, ξ , is also given, see text.

2θ (deg)					
Reflection	Sb_2Te_3	film	δQ , %	FWHM, Å ⁻¹	ξ , Å
(0 0 9) ^a	2.413	2.3 (2)	-4.5(4)	0.15 (5)	13(4)
(0 1 5) ^a	2.586	2.69 (1)	3.9(1)	0.05 (1)	42(6)
(1 0 10) ^a	3.476	3.51 (2)	1.0(1)	0.2 (1)	10(8)
(1 1 0) ^a	3.815	3.82 (2)	0.1(1)	0.043 (5)	50(4)
(1 1 0) ^b				0.035 (5)	63(5)
Si (1 1 1) ^a	2.606 (1)		-	0.015 (1)	

the raw data are shown in Fig. 22a. Although the statistics are poor due to limited amount of material defined by the film thickness the main features are shown in both orientations of raw spectra.

The Lamb Mössbauer factor can be extracted using the DPS, $f_{\text{LM}} = \exp\left(-E_{\text{R}} \int_0^{\infty} \frac{g(E)}{E} \frac{1+e^{-\beta E}}{1-e^{-\beta E}} dE\right)$ where E_{R} the recoil energy and $\beta = (k_{\text{B}}T)^{-1}$ where k_{B} is the Boltzmann constant and T is temperature. In the Debye approximation the f_{LM} in bulk Sb_2Te_3 using a Debye temperature of 135 K is 0.41 at 20 K and decreases to 0.30 at 40 K. The extracted Sb specific f_{LM} at 40 K, 0.18(5), on elemental modulated Sb_2Te_3 decreases dramatically with respect to the bulk counterpart. Thus, partial non crystallinity [137] further decreases the f_{LM} by 0.12. The Sb specific mean force constant, $\langle F_i \rangle$, is obtained from the second moment of the DPS, $\langle F_i \rangle = m_{\text{R}} \int_0^{\infty} g(E) E^2 dE / \hbar^2 = 52(2)$ N/m, where m_{R} is the resonant nuclear mass. The inset to Fig. 22 shows the Debye representation, $g(E)/E^2$. In the Debye representation, both crystalline and elemental modulated Sb_2Te_3 follow almost the same behaviour. However, the Debye level, $\lim_{E \rightarrow 0} \frac{g(E)}{E^2}$, slightly increases in the elemental modulated Sb_2Te_3 structure with respect to crystalline Sb_2Te_3 . The average speed of sound, v_{s} , can be extracted from the ¹²¹Sb Debye level using $\lim_{E \rightarrow 0} \frac{g(E)}{E^2} = \frac{m_{\text{R}}}{2\pi\hbar^3 \rho v_{\text{s}}}$, where ρ the mass density. In this study the long wavelength limit is set to 3.5 meV. The extracted average speed of sound in grazing incidence geometry using that the mass density is 5% decreased with respect to the bulk value, 6.48g/cm³, is 1.74(2) km/s.

3.4 DISCUSSION

Crystalization along the basal plane of layered structures has been reported in literature [138]. Shrinkage of in-plane distances with simultaneous extension of the out-of-plane lattice constants is characteristic of partially crystallised films obtained by modulated deposition. The non complete crystallinity of the sample studied in this work is confirmed not only by the enlarged FWHM of the observed crystallographic reflections but also by the reduction in the f_{LM} . In glasses, the f_{LM} appears reduced mainly due to lower elastic moduli and lower mass density compared to crystalline counterparts [139]. However, such modulated deposition compounds do not possess all properties of glasses, such as excess vibrational modes in the low energy range of the density of phonon states, because they still exhibit periodicity.

Phonon modes at the Γ point in bulk crystalline Sb_2Te_3 have been calculated from first principles [93]. The IR active $A_{2u}(3)$ mode, 18 meV, and the Raman active $A_{1g}(2)$, mode, 20 meV, correspond predominantly to Sb displacement along the c -axis. The extracted Sb specific DPS in elemental modulated Sb_2Te_3 films does not change significantly from its bulk counterpart. The extracted speed of sound coincides in bulk sample and elemental modulated film. This coincidence results from both the reduced mass density and the increased Debye level in the elemental modulated film with respect to the bulk counterpart. A slight decrease is observed in the acoustic cut-off energy, from 8.5 meV to 8 meV see Fig.22. This indicates that once the layered structure is formed, even before the crystallization is fully established, the main features in the DPS already emerge. In case crystallisation starts, misleading results related to preferred orientation might appear in anisotropic structures. Orientational dependence of the DPS has been observed earlier in anisotropic single crystals [52], however, this is not the case in this study since no obvious difference in the raw nuclear inelastic spectra as well as no strong film reflections have been identified.

The intraplane vibrational mode closest to the interlayer $A_{2u}(3)$ and $A_{1g}(2)$ modes is the mixed Sb-Te Raman active $E_g(2)$ at 14 meV. This indicates that, the elastic anisotropy defined by the energy spacing between inter- and intralayer modes is not as pronounced in Sb_2Te_3 as in typical layered structures, see for e.g. [124]. In addition, the ratio of interlayer to intralayer spacing is a rough but revealing structural measure of the layerlike character of the crystal. The higher this ratio is, the weaker the expected layer-layer coupling relative to intralayer bond becomes. In this study not only is the interlayer distance elongated by $\sim 5\%$ but also is the intralayer spacing compressed by $\sim 0.2\%$ with respect to crystalline Sb_2Te_3 . Slight decrease has been observed in the DPS extracted force constants which might be related to the interlayer force constants since the intralayer distance has not been changed significantly.

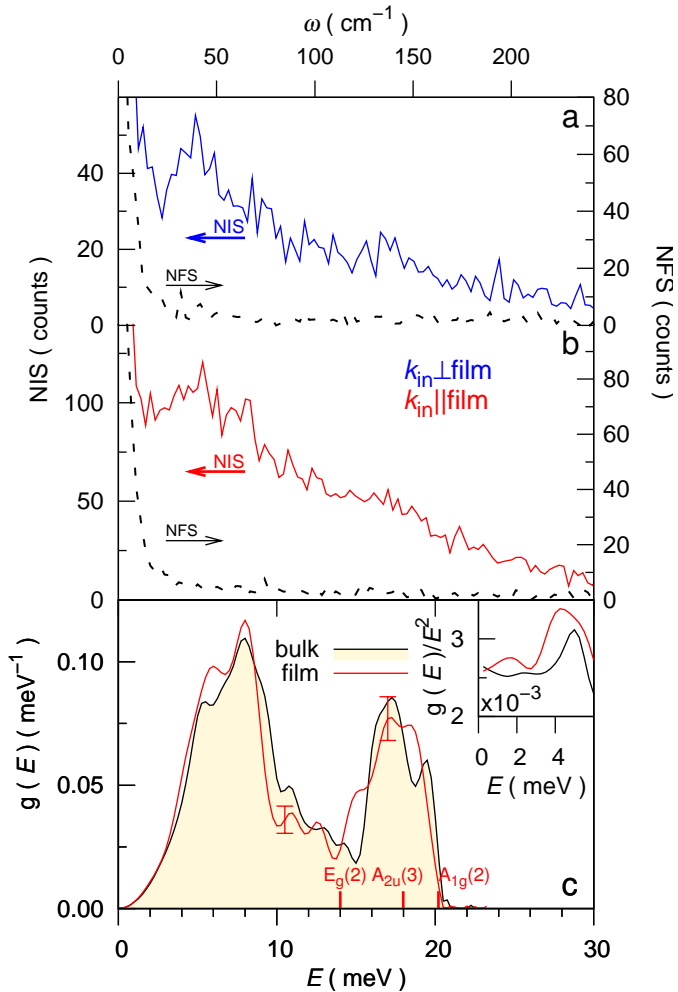


Figure 22: The nuclear inelastic spectra (lines) and the time integrated nuclear forward scattering, NFS-instrumental function (dashed lines), obtained in the elemental modulated Sb_2Te_3 film in two orientations. (a) with the incident wavevector, k_{in} , perpendicular to film surface and (b) with k_{in} parallel to the film surface. (c) shows the density of phonon states extracted with k_{in} parallel to the film surface (red) and the DPS measured on bulk Sb_2Te_3 . Inset: Debye level calculated from the Sb specific DPS measured in Sb_2Te_3 .

To corroborate the significance in the reduction of the acoustic cut-off energy an estimate in the macroscopically measured thermal conductivity is given using the relation extracted by Slack [119], $\kappa_L = A \frac{\overline{M}\theta_a^3 V_{at}^{1/3} N^{1/3}}{\gamma^2 T}$, where \overline{M} the average atomic mass, θ_a the acoustic mode Debye temperature, N the number of atoms per primitive cell, V_{at} the volume per atom, γ the Grüneisen constant, T is the temperature and $A \approx 3.1 \cdot 10^{-6}$ is a collection of physical constants. Because the measured DPS on the elemental modulated film is almost identical to the crystalline counterpart the vibrational energy defined Grüneisen parameter, $\gamma = -\frac{d \ln E}{d \ln V}$, is expected to be the same in first approximation. Thus, we assume that, $\gamma = 1.7$ [136]. The 5% increase of the volume per atom V_{at} , which is related to the corresponding decrease in the mass density in the elemental modulated film, does not increase κ_L by more than 1% in the film. However, the acoustic cut-off energy in the film appears $\sim 6\%$ decreased, from 8.5 meV to 8.0 meV, with respect to the bulk counterpart. We thus suggest that the lattice thermal conductivity in partially crystalline elemental modulated Sb_2Te_3 films is $\sim 15\%$ reduced with respect to bulk Sb_2Te_3 . Macroscopically measured thermal conductivity data on a similar samples exist [130]. The measured cross plane thermal conductivity, 1.6 W/m/K, has a lattice contribution apart from the lattice contribution and an electronic contribution as well. The observed reduction in thermal conductivity from the bulk value, 2.4 W/m/K, at room temperature [117] can be attributed both to the reduction of the electronic and the lattice contribution by almost the same amount, 17% and 16% respectively.

Combined lattice dynamics characterization using nuclear inelastic scattering by ^{121}Sb and x-ray diffraction on an elemental modulated Sb_2Te_3 show that in Sb_2Te_3 the main features in the density of phonon states are related to the layered of the crystallographic structure. The correlation length even in the as grown state is finite. The interlayer force constant shows an interlayer distance dependence. Reduction in macroscopically measured thermal conductivity on similar samples might be related equally to the reduction of the electronic and lattice contribution.

PHONON SPECTROSCOPY IN BISMUTH TELLURIDE NANOWIRE ARRAY

The lattice dynamics in 56 nm diameter Bi_2Te_3 nanowires embedded as an array in a self-ordered amorphous alumina membrane were investigated microscopically using ^{125}Te nuclear inelastic scattering. For the first time the element specific density of phonon states is measured on nanowires in two perpendicular orientations. In line with single crystalline Bi_2Te_3 the prominent peak in the Te density of phonon states at 13 meV is orientation dependent. Combined high energy synchrotron radiation diffraction and transmission electron microscopy was performed on the same sample and the crystallinity was studied. Nanowires grow almost perpendicular to the c-axis and some of the appear twinned along the c-axis. This results in highly texture in one orientation and nearly isotropic scattering in the other. The much lower average speed of sound at 40 K, 1.36(2) km/s, measured in 56 nm diameter Bi_2Te_3 nanowires as compared to 1.75(1) km/s in bulk Bi_2Te_3 is related to confined dimensions. The predicted decrease in the macroscopic lattice thermal conductivity by 50% due to confined cross section is primarily related to the reduced speed of sound and is corroborated by earlier macroscopic data.

4.1 INTRODUCTION

Theoretical foundations on nanoscale systems exist [140] and are routinely used to predict enhancement in thermal [141], electrical [55], and mechanical [142] properties of the investigated material. Recently, owing to rapid progress in nanostructuring technology the attention of scientific community was redrawn in the microscopic characterisation of low dimensional structures. Among the nanoscale systems, 2d nanomaterials such as graphene [143] and transition metal oxide nanolayers [144] are of great technological importance. The traditional 2d nanomaterials [145] have a thickness in the order of a few nanometers and length in the order of microns which makes them candidates not only for direct applications but also as building blocks of artificial structures.

In 1993, Hicks and Dresselhaus [59, 60] reported a significant enhancement in the thermoelectric figure of merit [146], zT , both in two- and one-dimensional nanostructures below $d = 3$ nm, where d is the dimension of

confinement, due to effective mass of charge carriers. After their study a great number of experimental studies was dedicated to the realisation of the asymptotic d^{-2} enhancement of zT . A definitive experimental confirmation is nevertheless, still lacking. A recent study by Cornett and Rabin [61] on semi-conducting nanowires deals has investigated the electrical properties, but no clear enhancement of the electrical properties were suggested for nanowires with several nm diameter. Arguably, the electronic mean free path is orders of magnitude shorter than that of phonons, thus in first approximation no clear effect in electronic properties was expected for d of hundred nm [147, 148].

Tetradymite structured chalcogenides exhibit, in addition to thermoelectric power conversion properties, a reversible phase change from crystalline to amorphous phase induced by temperature or electric field [53, 54]. Because the phase change is accompanied by a large resistance or reflectivity change such materials are considered candidates for future nonvolatile memory applications [71]. Thermal conductivity plays and important role in phase change applications [102] because it is related to the read - write time. Hence, tailoring the macroscopic properties of an array of low dimensional chalcogenides is not only of importance for fundamental reasons but it has a potential impact in information technology and power generation.

Experimental techniques which give access and measure directly the density of phonon states in bulk structures are limited to inelastic scattering of neutrons and x-rays. However, in nanostructures due to the limited amount of material and the complexity in handling, inelastic x-ray scattering is probably currently the only choice for investigating microscopically the lattice dynamics.

The phonon properties in an ensemble of 56 nm diameter nanowires embedded in a self ordered amorphous alumina membrane are the focus of this study. The lattice dynamical characterization was based on nuclear resonance inelastic scattering [149] using the ^{125}Te resonance [84]. In order to avoid misinterpretation and complement the dynamical properties a combined detailed structural characterization was conducted both of the ensemble, using high energy synchrotron radiation, and of individual nanowires, using electron scattering. Clues are obtained that a reduction in thermal conductivity should primarily be related to the reduced speed of sound.

4.2 EXPERIMENTAL METHOD

We prepared ^{125}Te enriched Bi_2Te_3 nanowires embedded in an anodic self ordered alumina membrane [150] using a novel pulsed electrodeposition technique described elsewhere [151]. In this work, the alumina membrane had nominal pore diameter of 50 nm with nominal interpore distance of 100 nm.

The aqueous electrodeposition solution was formed by dissolution of bismuth (III) nitrate pentahydrate and 80% ^{125}Te enriched tellurium powder in the appropriate ratio. Based on previous studies [152], the reduction potential was set to -200 mV in fixed pulses of 10 ms and the relaxation potential at 80 mV for 50 ms. All measurements reported in this study were carried out on small fragments with area of 5 mm \times 3 mm taken from the same alumina membrane.

In order to verify the crystallographic phase purity, diffraction using synchrotron radiation was performed at the 6-ID-D station of the Advanced Photon Source on bundles of nanowires inside an intact template. Measurements were carried out at 295 K in two orientations, (i) with the incident k vector parallel to the nanowire axes, called transmission geometry and (ii) with the incident k vector perpendicular to the nanowire axes, called grazing incidence geometry. Data was collected using an amorphous Si area detector of 2048 \times 2048 pixels (pixel size: 200 μm). The wavelength was 0.142519 \AA and the sample detector distance of 1715.5 mm was calibrated using diffraction from NIST Si 470c.

Single nanowires from the same sample were characterised by selectively dissolving the alumina matrix using a mixture of 6 wt.% H_3PO_4 and 1.8 wt.% H_2CrO_4 for several days at 40 degree Celcius. The nanowire suspension was deposited on holey grids and dried at room temperature. A Zeiss 912 Ω Transmission Electron Microscope, TEM, with a LaB₆ gun was used, operated at 120 kV having a point resolution of 0.37 nm and an energy resolution of 1 eV. Crystallinity and grain orientation were analyzed by electron diffraction patterns for which a SAED aperture was used and high-resolution images with strongly excited $\{0\ 0\ 1\}$ Bragg reflections were acquired.

The diameter of the wires was measured using a Scanning Electron Microscope, SEM, on single nanowires. In addition, the chemical composition was determined by Energy-Dispersive X-ray spectroscopy, EDX, in (i) a SEM with an accuracy of 0.5 at.% using bulk Bi_2Te_3 calibration standards and (ii) in the TEM using bulk calibrated Cliff Lorimer k factors. Chemical analysis by EDX in the SEM and TEM were in agreement. For EDX spectra acquisition a spot size of 32 nm was used. Quantitative chemical analysis was carried out by applying the Cliff-Lorimer method [153]. The Cliff Lorimer k factors were calibrated by combined EDX spectroscopy in the TEM and electron probe microanalyses, EPMA [154]. The integrated counts, N , under the Bi-L and Te-L edges were larger than 15000 yielding a maximal statistical error of $\sigma_N/N = 0.8\%$ (Poisson statistics) for the determination of the local molar fractions.

The lattice dynamics were investigated by means of nuclear inelastic scattering using a backscattering sapphire single crystal monochromator [45, 84] with a resolution of 1.1 meV for, 35.49keV, ^{125}Te resonance. Several spectra,

on the same sample and for both orientations for which diffraction patterns were acquired, were recorded in 16-bunch mode at the nuclear resonance station ID18 [155] of the European Synchrotron Radiation Facility. In order to minimise multiphonon contributions the measurements were carried out at 40 K.

4.3 RESULTS

4.3.1 Morphology and crystallinity

The precise chemical composition was measured by EDX in the TEM. EDX spectra were acquired on several nanowires and an average Te and Bi mole fraction of 64.6 at.% and 35.4 at.% was determined respectively. Control of the chemical composition in nanowires is still an open issue however our previous investigations [144] revealed that deviations in the order of 6 to 7% for the ideal stoichiometry in similar nanowires affect primarily the electric properties. Fig. 23 shows the expected Bi and Te lines in addition to Cu, Fe, C, Cr, and Al x-ray lines. The additional x-ray lines are coming either from well-known instrumental artifacts [154], i.e. Cu, Fe and C, or from dissolving the alumina template, i.e. Cr and Al. An oxygen peak was not observed and therefore there is no sign of surface oxidation.

It was found that the average wire length was 16 μm and appeared relatively homogeneous with no hint of overgrowth outside of the template pores as well as no hint of surface roughness. The estimated diameter using similar SEM images varies between 53 and 59 nm. To increase our resolution in wire diameter determination we have used two-beam dark-field images in the TEM and the estimated diameter was found in the same range. Fig. 23f shows a high resolution diffraction pattern of a wire in a pole orientation. The $\{0\ 0\ l\}$ reflections are clearly seen and an angle of 85 deg between the crystallographic c -axis and the nanowire axis was determined. Electron diffraction patterns observed at different points of several nanowires revealed single crystallinity over a length of 15 μm . In addition to single crystalline nanowires, Fig. 23d, twinned nanowires coming from the same template were observed using TEM high resolution diffraction. The twinning plane, which is located near the center of Fig. 23e, is identified as the reversal of stacking, 180 deg rotation of the crystal, about the $\langle 0\ 0\ 1 \rangle$ direction commonly observed in rhombohedral systems.

X-ray diffraction by a fragment of the alumina template filled with Bi_2Te_3 nanowires were obtained in two perpendicular orientations: (i) in transmission geometry and (ii) in grazing incidence geometry. Note that because the template is amorphous no contribution is expected in the diffractograms.

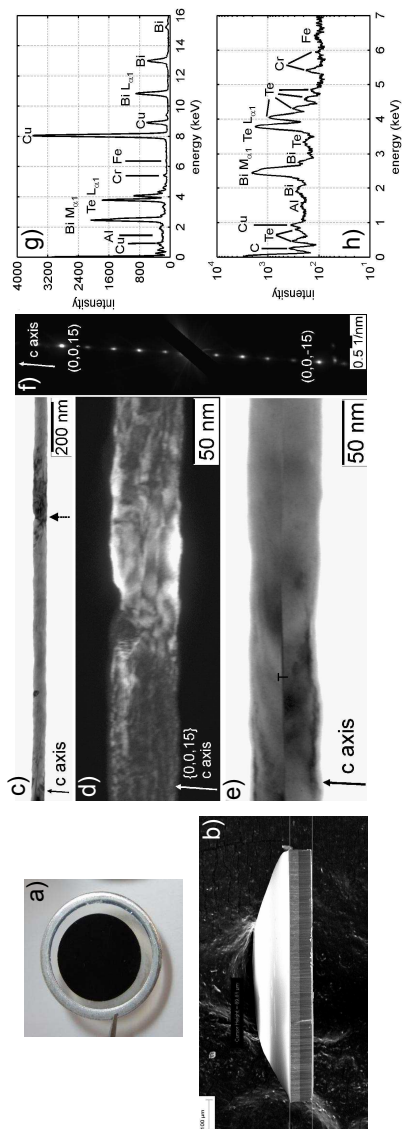


Figure 23: (a) Shows the alumina membrane (transparent area) inside an aluminium frame filled with Bi_2Te_3 nanowires (dark area). (b) Shows a cross section of the alumina membrane. (c) Overview of a TEM bright-field image. (d) High-magnification dark-field TEM image obtained with strongly excited reflections $\{0\ 0\ 1\}$, image was acquired at the nanowire region indicated by a dashed arrow in (c). (e) TEM bright field image of another nanowire with the twin boundary parallel to the basal plane in the center. (f) Appropriately rotated electron diffraction pattern obtained on nanowire shown in (c). EDX spectrum acquired in the TEM on a Bi_2Te_3 nanowire with a Te mole fraction of 64.4 at.%, shown in (g) linear and (h) logarithmic scale.

Fig. 24a,c show the detector patterns in circular coordinates obtained in both orientations. For sake of simplicity a half detector image is shown here. Both detector patterns should be interpreted as follows: the radial distance from the beam center corresponds to the scattering angle 2θ and the circular angle at certain radius corresponds to the azimuthal angle ϕ . Thus, apart from typical information related to structural properties, insight in preferential wire growth was obtained. From both detector patterns the one dimensional diffractograms were extracted after radially integrating the intensities at all azimuthal angles for a certain 2θ , see Fig. 24b. The diffraction patterns in both orientations are indicative of a rhombohedral lattice ($R\bar{3}m$, #160). In transmission geometry the observed Debye - Scherrer rings reveal isotropic scattering and the diffraction pattern was refined using Fullprof [40]. The expected powder diffraction intensities of the $(0\ 0\ 6)$, $(1\ 1\ 0)$ and $(1\ 1\ 15)$ reflections was not explicitly reproduced which indicates preferred orientation. The preferred orientation was corrected by the March-Dollase multiaxial function [89] with the assumption that the preferred orientation planes were the $(0\ 0\ 6)$, $(1\ 1\ 0)$ and $(1\ 1\ 15)$ planes. The obtained March-Dollase coefficient r was 0.283(3), 0.246(1) and 0.243(4) respectively; random oriented powder sample have $r = 1$. After the preferred orientation correction the resulting Bragg R-factor was 10.4%. The lattice parameters obtained at 295 K are $a = 4.3824(1)$ Å and $c = 30.2588(1)$ Å. Although the lattice parameter along the a -axis is in excellent agreement with the corresponding in bulk Bi_2Te_3 [156], the lattice parameter along the c -axis appears $\sim 1\%$ reduced compared to the bulk counterpart.

In grazing incidence geometry the same lattice constants have been extracted. However, strongly anisotropic scattering is observed in the azimuthal distribution. The detector pattern appears highly symmetric around 270 deg. The $(0\ 0\ 6)$ out of plane reflection yielded a triplet of equal intensity peaks at 264.5(1) deg, 269.8(1) deg and 275.2(1) deg. The peak positions were extracted after simultaneous fitting of three Lorentzians with an azimuthal full width at half maximum, FWHM, of 3.8(2) deg. This observation indicates that there are two additional c orientations discretely located at ± 5.4 deg from the nominal growth direction. On the other hand, the basal plane $\{1\ 1\ 0\}$ reflections, at 329.4(1) deg and 210.2(1) deg, are superimposed with diffuse scattering intensity. These reflections have equal intensity, the same azimuthal FWHM of 2.7(1) deg and $\Delta\phi = 59.6$ deg with respect to the central $(0\ 0\ 6)$ reflection. An extra reflection of the same type appears at azimuthal angle of 269.9(1) deg with similar FWHM but with half intensity. In addition to a broad reflection, FWHM 4.6(1) deg, around 180 deg (or for symmetry reasons around 360 deg), the composite $\{1\ 0\ 1\}$ type of reflections show two narrower ones, FWHM 3.5(2) deg, at 240.7(1) deg and 298.7(1) deg. The $\{0\ 1\ 5\}$ and the $\{1\ 0\ 10\}$ type of reflections appear as quartets in Fig. 24a.

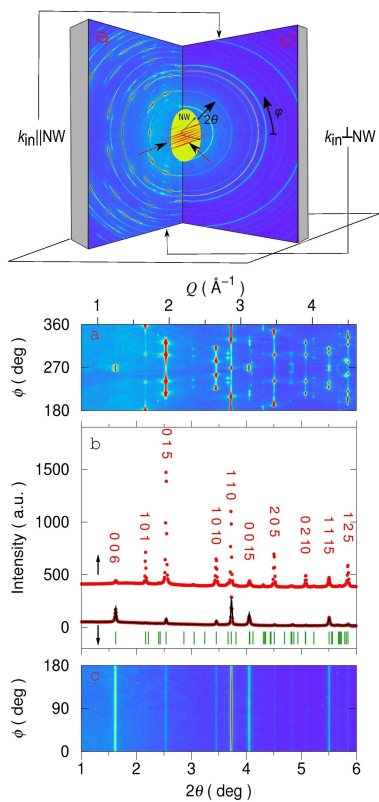


Figure 24: Diffraction of synchrotron radiation obtained on an array of Bi_2Te_3 nanowires with diameter of 56 nm embedded in a self ordered amorphous alumina membrane. (upper figure) shows the diffraction configuration. (a) shows the Debye - Scherrer rings recorded using a two dimensional area detector in grazing geometry versus the azimuthal angle ϕ . (c) shows the azimuthal projection of the Debye - Scherrer measured on the same sample in transmission geometry. (b) shows the extracted diffractograms (red points) and the refinement (black line).

4.3.2 Lattice dynamics

The nuclear inelastic scattering spectra from ^{125}Te enriched bulk and single crystalline Bi_2Te_3 have been recorded earlier [136]. In this study, we used the same instrumental setup [45] and we obtained the ^{125}Te nuclear inelastic spectra together with the time integrated nuclear forward spectra, i.e. instrumental resolution, in an ensemble of Bi_2Te_3 nanowires. The instrumental resolution had a Lorentzian shape with full width at half maximum of 1.1 meV. After subtraction of the elastic peak, a modified version¹ of the program DOS [51] was used to extract the density of phonon states. The self consistency of the procedure was confirmed by applying the conventional sum rules [50] and all thermodynamical parameters were extracted both from the raw data and the DPS. The ^{125}Te specific projected DPS on the nanowire ensemble, $g(E)$, was extracted in both orientations and shown in Fig. 25. Data shown in Fig. 25a was measured in the same orientation, i.e. transmission geometry, as data shown in Fig. 24c, the same holds for the grazing incidence geometry. The DPS in transmission geometry shows enhanced statistical noise and increased error bar compared to grazing incidence geometry. This is due to limited amount of material defined by the nanowire length.

From the DPS a series of thermodynamical parameters can be obtained. The Lamb Mössbauer factor, $f_{\text{LM}} = \exp\left(-E_{\text{R}} \int_0^{\infty} \frac{g(E)}{E} \frac{1+e^{-\beta E}}{1-e^{-\beta E}} dE\right)$, where E_{R} is the recoil energy, $\beta = (k_{\text{B}}T)^{-1}$ where k_{B} is the Boltzmann constant, and T is temperature, is closely associated with the lattice dynamics and the purely incoherent mean square Atomic Displacement Parameters, $\text{ADP} \langle u^2 \rangle = -\ln f_{\text{LM}}/k^2$, where k the wavenumber of the resonant photons. The extracted f_{LM} from NIS as well as the ADP are 0.34(1) and $3.29 \cdot 10^{-3} \text{Å}^2$ in grazing incident geometry, respectively. In transmission geometry, f_{LM} is 0.32(1). In addition, the Debye temperature is obtained directly from the DPS using the expression $\theta_{\text{D}}^2 = 3 / (k_{\text{B}} \int_0^{\infty} g(E) dE/E^2)$ valid in the high temperature limit. The obtained Debye temperature for Te in both orientations is 145(1) K. The Te specific mean force constant, $\langle F_i \rangle$, is obtained from the expression $\langle F_i \rangle = m_{\text{R}} \int_0^{\infty} g(E) E^2 dE/\hbar^2$, where m_{R} the resonant nuclear mass. The obtained values are 61(1) N/m in grazing incidence and 56(1) N/m in transmission geometry. Inset to Fig. 25 shows the Debye representation, $g(E)/E^2$ in the two orientations as well as in the bulk sample. The Debye level, $\lim_{E \rightarrow 0} g(E)/E^2$, increases in nanowires as compared to bulk samples. The average speed of sound, v_{s} , can be extracted from the ^{125}Te Debye level using $\lim_{E \rightarrow 0} g(E)/E^2 = m_{\text{R}}/2\pi\hbar^3 \rho v_{\text{s}}$, where ρ the mass density. In this study the long wavelength limit is defined using the acoustic mode composition factor

¹ The DOS program was modified for reconvoluting the extracted DPS with a gaussian function with the same FWHM as the measured time integrated NFS

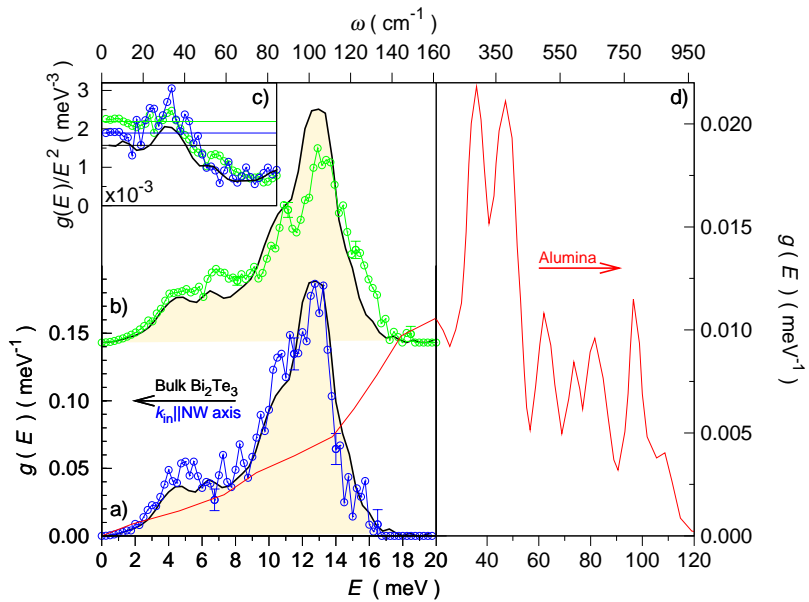


Figure 25: Te specific DPS measured in two orientations, (a) transmission (blue points) and (b) grazing (green points) incident geometry, on an array of Bi₂Te₃ nanowires with 56 nm diameter embedded in amorphous alumina template, typical error bar is given. For comparison, reference data (highlighted area) measured on bulk polycrystalline Bi₂Te₃ are shown. (c) Shows the Debye representation, $g(E)/E^2$, and the extracted Debye level, $\lim_{E \rightarrow 0} g(E)/E^2$, (color lines) are shown. The theoretically calculated DPS of amorphous alumina template is given in (d).

[135], $e_{ac}^2 = m_R/M_\Sigma$, where M_Σ the total molecular mass. The total molecular mass of Bi_2Te_3 is 800.7 amu. The area of three acoustic modes is equal to $m_R/M_\Sigma = 0.16$. The integral over the density of phonon states reaches this value at 6 meV. The extracted average speed of sound is 1.29(3) km/s in grazing incidence geometry and 1.36(2) km/s in transmission geometry.

4.4 DISCUSSION

The binary system Bi_xCh_y ($\text{Ch} = \text{Te}$ or Se) display several phases in the compositional range between 40 and 70 at.% Bi [157]. This wide variation of chemical composition have been theoretically explained in Bi_xSe_y by the approximately zero formation energy difference between all the phases [158]. Remarkably, all Bi_xTe_y phases crystallise in rhombohedral symmetry with very similar in-plane lattice parameter, a , however, the out-of-plane lattice parameter, c , is distinctive [159]. This effect is confirmed from our measurements and only the lattice constant along c -axis appears $\sim 1\%$ reduced compared to the bulk counterpart. Not only does the chemical composition affect the phase in which the material crystallizes but also the sample treatment, e.g. shear deformation during hot-pressing [55] is a key factor. In this study, we identified twins using TEM diffraction on several wires formed during sample growth. The twinning plane corresponds to 180 deg rotation of the unit cell around the c -axis. Similar twinning plane has been reported earlier by Medlin et al. [160] on Bi_2Te_3 nanocomposited samples prepared using current assisted sintering,. however, the precise chemical composition after sintering is not given. Thus, we cannot attribute the formation of twins neither to off stoichiometry nor to sample growth conditions. This type of twinning is well known in rhombohedral symmetry and allows both $-h + k + l = 3n$, indicated as m -type, and $h - k + l = 3n$ indicated as t -type, where h , k , l are the Miller indices of rhombohedral unit cell in the pseudohexagonal notation and n is integer. However, even with the additional information of unit cell twinning the reflection indexing of our detector pattern, see Fig. 24a, using only the interplanar angles [161] between the detected reflections and the $(0\ 0\ 6)$ reflection appears puzzling. For example, the nominal angles between the $\{0\ 0\ l\}$ and the $(1\ 0\ 1)$ or the $(0\ 1\ 5)$ type of reflections are 82.9 deg and 58.1 deg, respectively. However, in our diffraction pattern additional reflections with different azimuthal angles belonging to $(1\ 0\ 1)$ and $(0\ 1\ 5)$ type of reflections are shown. In diffraction of high energy synchrotron radiation, due to very high penetration depth² a superposition of diffraction patterns is obtained from different single crystalline nanowires embedded in the same

² The estimated transmission of synchrotron radiation with energy of 86.9 keV in a 3 mm thick sample of Bi_2Te_3 is 1 %.

template. In order to understand our raw detector images the texture simulation program Anaelu [162] was used and a rotational system composed of three angles, namely x , y , z , around the corresponding coordinate system was introduced. In grazing incidence geometry, the c -axis was almost perpendicular, x between 89 and 91 deg relative to the nanowire axis. The angle z was between -5 and 5 deg and accounting for the triplets in the $\{0\ 0\ l\}$ reflections. The y angle defined as the rotation around the c -axis was between 328 and 332 deg. This unit cell orientation resulted in simulation of all major reflections. The detector pattern in transmission geometry indicates that the $(0\ 0\ 6)$ reflection is isotropically distributed in the scattering plane, see Fig. 24c. Therefore, a composite rotation by 360 deg around the nanowire axis was applied to describe the total pattern. In this case, the $\{0\ 1\ 5\}$ type of reflections shown in Fig. 24a can be indexed as $(1\ 0\ -5)_m$ at $\phi = 322.1(1)$ deg and $(-1\ 0\ -5)_t$ at $\phi = 217.5(1)$ deg. The former correspond to a nanowire sub-ensemble with $x \sim 90$ deg and $y \sim 330$ deg. The reflection appearing at $\phi = 297.8$ deg can be indexed as $(1\ -1\ 5)_t$ and at $\phi = 241.7(1)$ as $(0\ -1\ -5)_m$, however, the origin of these reflections is different. They come from another nanowire sub-ensemble which is rotated by 90 deg around the nanowire axis. Similar indexing is applicable for the $\{1\ 0\ 10\}$ type of reflections. To substantiate the simulation of diffraction patterns, we rotated the beam direction by 90 deg by keeping the same wire orientation and we obtained similar detector image as in Fig. 24a. In summary, the array of 56 nm diameter and 16 μm long Bi_2Te_3 nanowires embedded in an amorphous alumina membrane exhibits a complex diffraction pattern due to preferred orientation during the sample growth as well as due to twinning which might be related either to chemical composition or effective conditions during electrodeposition. The nanowire growth direction is along $\langle 1\ 0\ 1 \rangle$ direction and the c -axis is perpendicular to the wire axis. The nanowire array shows powder like diffraction pattern in one orientation and composite single crystal like diffraction pattern in the perpendicular orientation. It, thus, gives us the possibility to study the influence of phonon transport both due to nanostructuration as well as due to preferred orientation on the same sample.

Previous studies of thermal transport in nanowires with diameter in the range of several nm revealed phonon confinement in the nanowire cross sectional area [163] as well as by surface roughness [164]. Finite size effects were predicted to cause a significant frequency shift or a lineshape broadening [165]. Nevertheless, misleading artifacts of instrumental origin resulting in such effects were identified and explained in germanium nanowires [65]. To the best of our knowledge, no complete experimental study exists on the density of phonon states in nanowires due to experimental limitations, e.g. sample amount and handling. First, no obvious changing phonon lifetime in scattering data is observed. The influence of defects and doping on the

phonon lifetime of optical phonons has been studied in carbon nanotubes [166]. It was shown that irrespectively from the electronic properties the optical phonon lifetime extracted from the Raman linewidth decreases to ~ 0.4 ps at an estimated crystallite size of 130 nm. In bulk Bi_2Te_3 the acoustical energy cut-off is around 6 meV [136]. The prominent peak at 13 meV in the Te DPS is the IR active mode $A_{2u}(2)$ which corresponds to pure Te displacement along the c -axis. The optical phonons in Bi_2Te_3 do not contribute significantly in thermal conduction [116]. In nuclear inelastic scattering, both the absorption probability and DPS depend on the orientation of the incident radiation relative to the crystallographic axes [135]. Orientational dependence of the projected DPS has been observed earlier in anisotropic single crystals [52]. In transmission geometry the nanowire array resembles an isotropic material as it was shown in diffraction of synchrotron radiation. In grazing incidence geometry the sample appears crystallographically anisotropic. Only phonons which have a polarization component parallel to the wavevector of the incident photons are probed. This is the reason why the measured optical phonons around 13 meV deviate significantly from its counterpart in the bulk. A substantial decrease in speed of sound, of the order of 22% has been observed between our nanowires in transmission geometry at 40 K and bulk samples measured at 20 K. Our microscopically extracted speed of sound can be directly compared to reference elastic constants data measured on single crystals using the Voigt average [37]. At 40 K the upper limit of the average speed of sound using Bi_2Te_3 mass density of 7.86 g/cm^3 is 1.918 km/s [136]. Temperature effect does not change, between 20 and 40 K does not change the speed of sound. Hence, the observed difference in the speed of sound between bulk and Bi_2Te_3 nanowires in the transmission geometry is attributed to confinement due to nanowire cross section. The integral of the DPS in both orientations should be the same because is related to the vibrational degrees of freedom. Therefore, the broadening of the $A_{2u}(2)$ mode in the grazing incident geometry due to crystallographic anisotropy causes a further reduction in the speed of sound. Force constant is calculated from the second moment of the DPS. Thus, excessive vibrational states in the high energy limit result in higher force constant, which is the case for the grazing incident geometry. Thus in grazing incident geometry the reduction in the speed of sound is not attributed to confinement.

Theoretical investigations on the DPS in amorphous alumina [167] were recently reported. According to these calculations the DPS of amorphous alumina follows the Debye law until 20 meV where a boson peak related to amorphous state appears. The main phonon modes appear between 24 and 120 meV, see Fig. 25. The alumina template in this case is behaving as an isotropic elastic medium without any interference with the bismuth telluride phonons. Note that the thermal conductivity at room temperature

of the alumina template [168], 1.3 W/m/K, is in the same range with the thermal conductivity measured on similar Bi₂Te₃ nanowires [169] and thus direct integration of nanowires in functional devices inside the template is not desirable because of the heat leakages.

Thermal conductivity data on bulk Bi₂Te₃ has been measured and show a variation as function of Te composition [170]. However, this variation is attributed mainly to electronic part of thermal conductivity. Thus, slight off-stoichiometry does not influence significantly the lattice part of thermal conductivity. In first approximation, the lattice thermal conductivity, k_L , depends on the specific heat at constant volume, C_V , the sound velocity, v_s , and the phonon lifetime, τ , and can be expressed in the simple kinetic gas theory by $k_L = C_V \cdot v_s^2 \cdot \tau/3$. The low thermal conductivity in bulk bismuth telluride is ascribed to the combination of low speed of sound and low acoustic cut-off energy [136] and yields 1.6 W/m/K at room temperature [117]. In this study, no change in the phonon lifetime but a 29% decrease in the speed of sound has been identified in transmission geometry compared to bulk. Hence, the lattice thermal conductivity along the nanowire axis related to confined cross section is expected to decrease by 50%. Indeed a similar decrease, between 28 and 57%, has been reported for macroscopic measurements between bulk and Bi_{0.485}Te_{0.515} nanowires [169]. In summary, the reduction in macroscopically measured thermal conductivity on Bi₂Te₃ nanowires with diameter around 50 nm is mainly related to the reduction of lattice thermal conductivity.

LATTICE INSTABILITIES IN BULK EUROPIUM TITANATE

Our detailed structural and lattice dynamical investigations of the bulk cubic perovskite EuTiO_3 reveal a lattice instability close to room temperature. The low temperature phase is associated with anharmonic europium displacement and has a significant impact on the lattice dynamics. This result is in agreement with recent first principle calculations predicting polymorphism in EuTiO_3 .

5.1 INTRODUCTION

Perovskites exhibit cubic symmetry, with space group $\text{Pm}\bar{3}\text{m}$, at high temperature with a large flexibility of site occupancy, indicated in the chemical formula $\text{ABX}_{3\pm\delta}$, by a broad range of elements, on the A and B sites [171] and flexibility in oxygen stoichiometry on the X site [169]. The oxygen sites in the perovskites' unit cell are forming interconnected octahedra [172], the rotation of which are potentially responsible for distortions away from the cubic symmetry and for structural phase transitions. Ba, Sr, and, to a lesser extend, Eu perovskite titanates have attracted significant interest owing to their ferroelectric properties and their potential applications in information technology. EuTiO_3 is a quantum paraelectric perovskite like SrTiO_3 , with however magnetic cations on the A-site, which undergoes a transition to a G-type antiferromagnetic phase below 5.3 K [173, 174]. Recently, ferroelectric instabilities on EuTiO_3 films [144] under 1% of both compressive and tensile stress were reported. However, in bulk EuTiO_3 the cubic $\text{Pm}\bar{3}\text{m}$ structure was reported [175] to be stable down to LHe temperatures. Only recently some hint of a phase transition at 284 K was published [176, 177] revealing structural disorder between 282 and 200 K and the appearance of antiferrodistortive tetragonal I4/mcm structure. These unexplained results require clarification by detailed microscopic and macroscopic experimental investigations. Coexistent short range phases summing up in the long range to an average structure have been reported both in manganites [178] and titanates [179].

Recent first-principle calculations [180] in EuTiO_3 show that the $\text{Pm}\bar{3}\text{m}$ symmetry is unstable at the M- and R- high symmetry points of the Brillouin zone with respect to the rotation of the oxygen octahedra. The lattice insta-

bilities are removed when the structure relaxes in one of three symmetries: tetragonal (space group: $I4/mcm$), orthorhombic (space group: $Imma$) or rhombohedral (space group: $R\bar{3}c$). Although all aforementioned symmetries exhibit well separated relaxation energies between -25 and -27 meV with respect to the cubic symmetry, the energy difference among them is very small and allows in fact polymorphism [180].

In this study we present a detailed investigation of the phase purity, the crystallinity and the lattice dynamics in bulk polycrystalline EuTiO_3 using both microscopic and macroscopic measurements. We demonstrate that a lattice instability related to europium anharmonic displacement appears close to room temperature with significant impact in the lattice dynamics of the system. Based on our data we attribute the observed lattice instability to the theoretically predicted polymorphism.

5.2 PREPARATION

Phase pure EuTiO_3 polycrystalline samples were prepared using a stoichiometric ratio of precursors (Eu_2O_3 99.99%; and Ti_2O_3 99.9%). The mixture was homogenised in a planetary ball mill, cold isostatically pressed at 300 MPa, and sintered in pure hydrogen at a temperature of 1400 °C for 2 hours. The details of pellets processing are given elsewhere [181]. The sintered pellets had a relative density of 80%. All measurements were performed on small pieces or powder taken from the same pellet.

5.3 RESULTS AND DISCUSSION

To verify the crystallographic phase purity and to check for a potential structural transition related to the M - and R - high symmetry points of the Brillouin zone, temperature dependent powder diffraction was carried out between 10 and 300 K using high-energy synchrotron radiation at station 6-ID-D/APS. The wavelength of the measurement was 0.142013 Å and the overall precision including sample size and detector pixel was $\frac{\Delta d}{d} \sim 5.0 \times 10^{-3}$. No peak splitting was observed. The data were refined with Fullprof [40] using the Rietveld method. A refinement of a typical diffractogram, with $R_{wp} = 8.3\%$, is shown in Fig.26. All observed reflections were identified in all possible symmetries. In order to account for any resolution limited satellite reflection the FWHM of all reflections was studied using a Lorentzian profile. The extracted FWHM between 10 and 300 K of selected reflections (indicated in Fig.26 by $R_1 \equiv (3\ 1\ 0)$ in $Pm\bar{3}m$ or $\{(1\ 3\ 4), (1\ 2\ 8)\}$ in $R\bar{3}c$ or $\{(1\ 1\ 6), (3\ 3\ 2), (4\ 2\ 0)\}$ in $I4/mcm$ or $\{(0\ 6\ 4), (2\ 6\ 0), (0\ 2\ 12), (2\ 0\ 12), (6\ 2\ 0), (6\ 0\ 4)\}$ in $Imma$ and $R_2 \equiv (3\ 1\ 1)$ in $Pm\bar{3}m$ or $\{(0\ 4\ 2), (2\ 2\ 6), (0\ 2\ 10)\}$ in $R\bar{3}c$ or

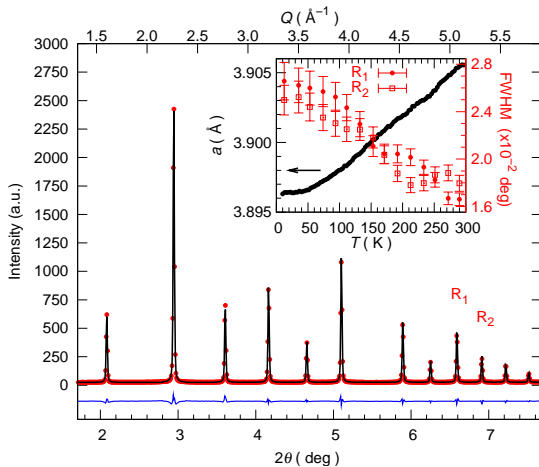


Figure 26: Rietveld refinement (black line) of a typical EuTiO_3 diffractogram (red points) at 300 K measured using synchrotron radiation and refinement residuals (blue line). Inset: the extracted temperature dependent lattice parameter (pointsize defines errorbars) in cubic symmetry and the Full Width at Half Maximum (FWHM) of certain reflections (R_1 and R_2) are given.

$\{(4\ 2\ 2), (2\ 0\ 6)\}$ in $I4/mcm$ or $\{(2\ 6\ 4), (2\ 2\ 12), (6\ 2\ 4)\}$ in $Imma$) are shown in the inset to Fig.26. The FWHM of all the examined reflections show the same broadening upon cooling. Although this observation might be indicating departure from cubic symmetry, it does not give further information on the establishment of a new crystallographic symmetry. The inset to Fig.26 shows also the extracted lattice parameter in cubic symmetry which is in excellent agreement with reference data [175]. Linear thermal expansion is observed between 100 and 300 K. The calculated volume thermal expansion coefficient, α_V , after fitting the lattice parameter with a linear function normalised to the lattice parameter at 300 K is $\alpha_V = 9.92 \times 10^{-6} \text{ K}^{-1}$. Minor deviations from linearity are observed between 200 and 270 K, see inset to Fig.26, which might support the claim of instabilities in this region. A priori, a traditional phase transition is however not established because no obvious sign in the performed measurements has been observed.

The phase purity was extensively investigated using ^{151}Eu -Mössbauer spectroscopy. Temperature dependent Mössbauer spectra were measured between 90 and 325 K on fine powder of EuTiO_3 , 35 mg/cm^2 , mixed with BN using a calibrated spectrometer, see ¹. A typical Mössbauer spectrum at

¹ online supplementary material

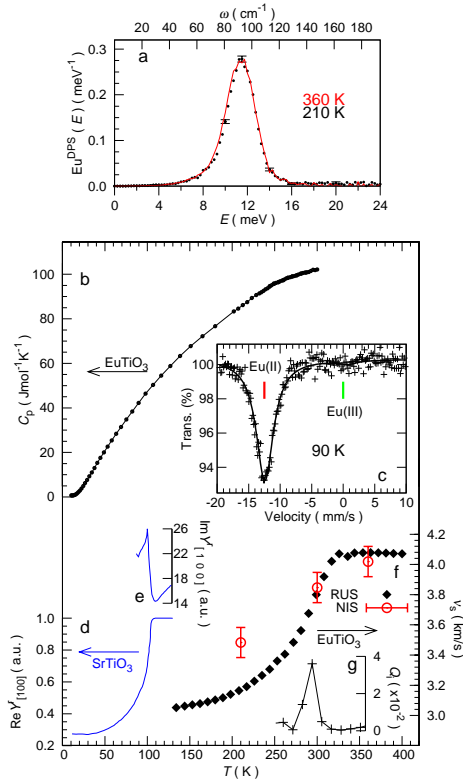


Figure 27: (a) The Eu specific density of phonon states in EuTiO₃ at 210 K (black ticks) and 360 K (red line-ticks) measured using NIS, typical errorbar is given. (b) Heat capacity data between 10 and 300 K measured on EuTiO₃ using calorimetry (pointsize defines errorbar), line between points is given as guide to the eye. (c) Mössbauer spectrum at 90 K (points) and the two component model (line). The positions of divalent and trivalent Eu are indicated. (d) The real part, $\text{Re}Y_{[1 0 0]}'^r$, of the complex Young's modulus in SrTiO₃ obtained from Ref. [182]. The imaginary part, $\text{Im}Y_{[1 0 0]}'^i$, of the complex Young's modulus of SrTiO₃ obtained from the same reference is shown in (e). (f) Speed of sound extracted from RUS (black points), pointsize defines errorbar, and the corresponding extracted from NIS (red circles) at 210, 300 and 360 K. (g) The inverse quality factor of the resonance at 590 kHz between 250 and 350 K.

90 K is given in Fig.27c. The data were fitted with a two component model. The area of the second component contributes to less than 1(1) % in the total area. The extracted isomer shift for the first component of our model was $-12.45(5)$ mm/s relative to EuF_3 , an isomer shift indicative of Eu(II). Thus, the sample contained purely divalent Eu. The upper limit of trivalent Eu which might escape detection is 1%. Within the Debye approximation, the Lamb - Mössbauer temperature $\Theta_{\text{LM}} = 295(5)$ K, was calculated² from the temperature dependent Lamb - Mössbauer factor, f_{LM} .

Magnetic characterization below 30 K was performed in a Cryogenics Ltd. closed cycle measuring system. Using ac susceptibility measurements ($f = 20.4$ Hz, $H_{\text{ac}} = 10$ G at $H_{\text{dc}} = 0$ G) the antiferromagnetic transition was found at $T_{\text{N}} = 5.2(1)$ K³ matching the antiferromagnetic transition of EuTiO_3 [183]. No other magnetic transitions have been identified. Below the observed transition, at 4.9 K, dc magnetization was measured with maximum applied magnetic field of $H_{\text{dc}} = 50$ kG where neither hysteretical behavior nor ferromagnetic contributions were observed⁴. Combining the results of magnetic characterization with the Mössbauer spectroscopy our sample properties are consistent with the reported antiferromagnetic properties of EuTiO_3 [183] and preclude other europium titanates.

In order to verify claims of a striking phase transition observed in heat capacity measurements on EuTiO_3 [176] the same cryostat, Quantum Design (QD-PPMS), utilising the same built-in calorimeter was used. Special attention was taken on the thermal coupling between the measuring platform and the sample [27]. Measurements of both the addenda and sample were performed at the same temperatures between 10 and 300 K with a 0.5 K point density in the region of interest. Every data point was measured three times and an average value was extracted. The averaged data are shown in Fig.27b. The measured heat capacity in EuTiO_3 reveals no evidence of a structural phase transition in contrast with what has been observed using similar techniques in SrTiO_3 [184].

To probe the lattice dynamics macroscopically Resonant Ultrasound Spectroscopy (RUS) [185] was used. Temperature dependent spectra in the frequency range of a hundred kHz to a few MHz were recorded on a rectangular parallelepiped sample (dimensions: 2.5 mm x 2 mm x 1.5 mm) using an in-house spectrometer made of cylindrical Y-cut lithium niobate 0.3 mm thick transducers (diameter 1.5 mm) inside a QD-PPMS. The isotropic elastic tensor, C_{11} and C_{44} , was extracted from the sample's natural resonances and the bulk, $B_{295\text{ K}} = 125$ GPa, and shear, $G_{295\text{ K}} = 76$ GPa, moduli were calculated. The speed of sound extracted from RUS is shown in Fig.27f. In Fig.27g the

² See online supplementary material

³ See online supplementary material

⁴ See online supplementary material

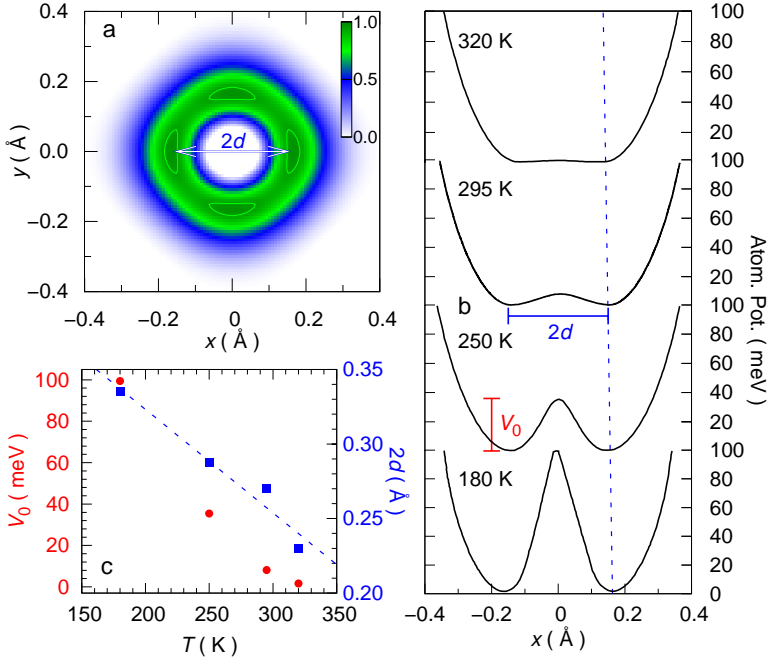


Figure 28: (a) Probability density function distribution of the Eu-atom in the ab plane at 180 K. (b) Shows the effective one-particle potential of the Eu atom along the a direction ($y = 0$) at 320, 295, 250 and 180 K obtained from crystallographic structure analysis. (c) The potential barrier, V_0 , and the displacement from equilibrium position, $2d$, (dashed line is guide to the eye) extracted from the potential given in (b).

inverse quality factor, Q_i , of a typical mechanical resonance at 590 kHz is shown. The average speed of sound calculated from the isotropic elastic tensor indicates 25% hardening at 300 relative to 100 K. Similar behaviour was observed on a second sample from the same batch. Although no obvious instability was identified both in diffraction of synchrotron radiation nor by calorimetry, a prominent acoustical stiffening upon heating is observed between 100 and 300 K. The acoustical stiffening is corroborated by a peak in Q_i at 290 K. A similar behaviour is observed in the real as well as the imaginary part of Young’s modulus measurements at 100 K on SrTiO_3 [182], see Fig. 27d and Fig. 27e.

To study accurately the atomic behaviour in EuTiO_3 further diffraction experiments using neutrons were performed. Europium is a strong neutron

absorber [186], thus a thin homogeneous powder layer was prepared using 700 mg of EuTiO_3 and placed between thin vanadium foils (0.02 mm x 1 cm x 3 cm). Neutron scattering data were collected, with precision $\frac{\Delta d}{d} \sim 1.5 \times 10^{-3}$ at $d = 1 \text{ \AA}$, between 10 and 300 K using the time-of-flight instruments POWGEN [187] and NOMAD at the Spallation Neutron Source. The pair distribution function, PDF, analysis was carried out by Fourier transformation of the total scattering function. However, in the total scattering function diffusive non constant background from the strong europium absorption is arising which produces oscillations in the extracted PDF. The refinement of PDF was conducted using PDFgui [188] between 2.5 and 50 \AA . Within the limited precision of our extracted PDF no clear change with temperature in the inter-atomic distances of oxygen with europium or titanium is observed, see⁵. The raw data were then refined with JANA2006 [38] using the Rietveld method resulting in $R_{\text{wp}} = 7.4\%$. Specifically, the atomic displacement parameters, ADP, extracted in the harmonic approximation of Eu, Ti and O at 180 K are 21.0(8), 7.3(5) and 7.5(5) ($\times 10^{-3} \text{ \AA}^2$) respectively and do not show any substantial irregularity versus temperature. In the harmonic approximation the Eu ADP is large as compared to Ti and O. Hence, a Fourier map study in the vicinity of the Eu was carried out. The Gram-Charlier expansion of anharmonic atomic displacement parameters is extensively described in Ref. [19] and has been followed in several cases of perovskite structure [189, 190]. In this study, the Eu atomic displacement parameters extracted from neutron diffraction assuming cubic symmetry, $\text{Pm}\bar{3}\text{m}$ space group, was modeled using a Gram-Charlier expansion of the probability density function, $p_{\text{Eu}}^{\text{GC}}$, up to fourth-rank tensor given in Eq. 5.1 [191].

$$p_{\text{Eu}}^{\text{GC}}(\mathbf{r}) = p_{\text{Eu}}^{\text{harm}}(\mathbf{r}) \left[1 + \frac{1}{4!} D_{\text{GC}}^{\text{ijkl}}(\mathbf{r}) H_{\text{ijkl}}(\mathbf{r}) \right] \quad (5.1)$$

where \mathbf{r} is the displacement vector of an atom from its equilibrium position, $H_{\text{ijkl}}(\mathbf{r})$ is the Hermite polynomial of fourth order and $D_{\text{GC}}^{\text{ijkl}}(\mathbf{r})$ are anharmonic refined parameters (the third-order cumulants, $C_{\text{GC}}^{\text{ijkl}}(\mathbf{r})$ are zero, based on the site symmetry). The use of a fourth order Gram-Charlier expansion for the ADP [19] significantly improves the refinement. In Fig.28a the europium probability density function at 180 K is illustrated after final refinement. It is seen that Eu exhibits off-centering in [1 0 0] and [0 1 0] directions (and equivalently in the [0 0 1] direction) with significant residual probability density in

⁵ online supplementary material

the azimuthal direction. The effective one-particle atomic potential, $V(r)$, is related to the probability density function by the formula given in Eq. 5.2.

$$V(r) = -k_B T \ln \left[p_{\text{Eu}}^{\text{GC}}(r) / p_{\text{Eu}}^{\text{GC}}(r_0) \right] \quad (5.2)$$

where k_B is the Boltzmann constant and T is temperature. In Fig.28 a section of the Eu one-particle potential extracted according to the Eq. 5.2, along the $[1\ 0\ 0]$ direction for several temperatures is depicted. These sections reveal that Eu atom exhibits temperature dependent off-centering, see Fig.28c, with $d \sim 0.17\ \text{\AA}$ at 180 K. In addition, the boundary potential along the azimuthal direction follows the same behaviour and flattens well before 295 K. Above 295 K, the Eu probability density function forms a plateau which indicates increased anharmonicity. Similar refinements were conducted for the atomic displacement parameters of Ti and O, however, the convergence failed. An analogous double-well potential for EuTiO_3 was suggested theoretically by Bettis et al. [192].

To substantiate the observation of europium delocalization lattice dynamics investigations based on nuclear inelastic scattering [193], NIS, of ^{151}Eu in EuTiO_3 were performed. Several spectra were recorded in 16-bunch mode at the nuclear resonance station ID22N/ESRF [87] using a nested monochromator [194] providing 1.5 meV resolution. Using a closed cycle displax cryostat scans were performed at 110, 210, 295 and 360 K. The raw spectra were treated using a modified version⁶ of the program DOS [51]. The ^{151}Eu -projected density of phonon states⁷, DPS, was extracted between 0 and 24 meV, see Fig.27a, together with all the related thermodynamic parameters. The ^{151}Eu -projected DPS shows a single peak around 11.5 meV which is in agreement with first principle theoretical calculations [180]. No resolvable change has been observed in the ^{151}Eu DPS between 210 and 360 K, see Fig. 27a. The extracted f_{LM} agree with the Mössbauer measurements within 95%. The ^{151}Eu mean force constant between 110 to 360 K ranges from 78 to 70 N/m and the NIS extracted Eu ADP are 80% of those extracted from neutron diffraction. The fair agreement of ADP extracted from NIS and diffraction is discussed elsewhere [195]. From the long wavelength limit, below 4 meV, of DPS the speed of sound, v_s , can be calculated, see⁸. The DPS extracted speed of sound also indicates hardening of EuTiO_3 versus temperature, as observed also using RUS, see Fig. 27f. Both microscopic and macroscopic measurements are in good agreement. The 10% deviation at 210 K is reproducible and we

6 The DOS program was modified for reconvoluting the extracted DPS with a gaussian function with the same FWHM as the measured time integrated NFS

7 The natural abundance of ^{151}Eu is 47.8 % and no further isotopic enrichment was needed

8 online supplementary material

attribute it to the difference in the phonon energy regions probed by RUS and NIS as well as the low mass density of our RUS measured sample.

As a result, the increase in speed of sound upon heating is verified both by microscopic and macroscopic techniques and is in contrast to the usual softening of elastic constants upon heating [196] confirming the lattice instability of EuTiO_3 between 100 and 300 K.

In summary, the combination of the extracted speed of sound by RUS and NIS together with pair distribution function analysis and Gram - Charlier expansion of Eu atomic displacement based on neutron diffraction as well as feedback from theoretical studies based on *ab initio* calculations provides a clear evidence for europium delocalization which results in lowering of the short range symmetry of the system. Short range coexistence of crystallographic phases with candidate symmetries Imma , $\text{R}\bar{3}\text{m}$ and I4/mcm in EuTiO_3 is probably the reason for europium delocalization. Experimental studies under high pressure on phase pure EuTiO_3 might shed further light on the exact scenario.

5.4 SUPPLEMENTARY INFORMATION

5.4.1 *Mössbauer Spectra*

The phase purity was investigated using ^{151}Eu -Mössbauer spectroscopy. Several Mössbauer spectra with 6% absorption were measured between 90 and 325 K on a homogeneous mixture of fine grain EuTiO_3 powder, 35 mg/cm^2 , and BN, see Fig.29a. The data were measured using a calibrated instrument in a nitrogen flow cryostat and fitted using a two component model in order to incorporate for any potential europium impurity related to Eu(III) . A potential second component containing Eu(III) is resolution limited to less than 1%. The f_{LM} related to Eu(II) follows the expected Debye behaviour with Debye temperature given in the main text. From the same data, the isomer shift of the majority component was extracted and is given in Fig.29b.

5.4.2 *Magnetization Measurements*

Divalent Eu based titanium compounds have been investigated extensively by McGuire et al. [197] owing to their remarkable variety in magnetic properties. Among them, pyrochlore compound $\text{Eu}_3\text{Ti}_2\text{O}_7$ and Eu_2TiO_4 perovskite are impurity candidates in any EuTiO_3 sample. According to literature, both compounds show ferromagnetic transitions around $8.7 \pm 0.3 \text{ K}$ [183]. However, in our magnetization data, see Fig.30, neither ferromagnetic transition appeared around 9 K nor is a ferromagnetic contribution present in the $M - H$ curve

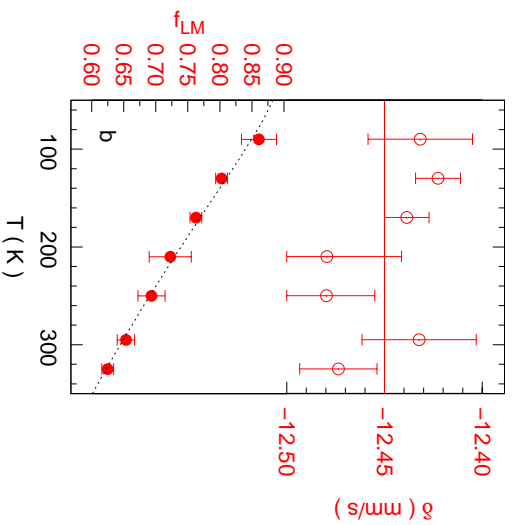
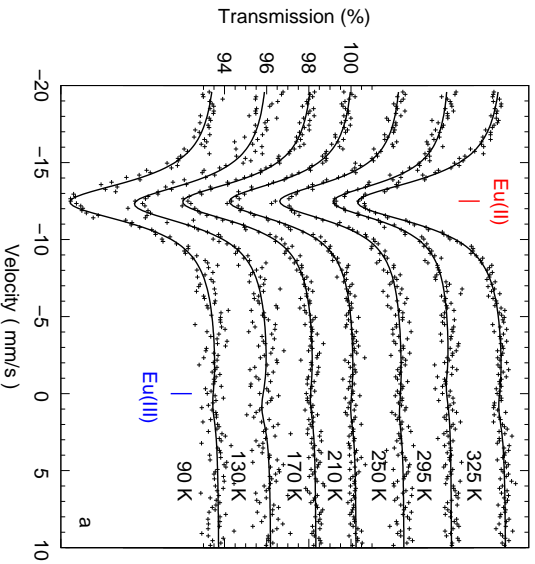


Figure 29: (a) Temperature dependent ^{151}Eu -Mössbauer spectra measured on EuTiO_3 powder (black points) and the corresponding two component model (black line). The expected isomer shift relative to EuT_3 is indicated with tics. (b) Temperature dependent Lamb-Mössbauer factor, f_{LM} , of the majority phase, Eu(II) , extracted from (a) and the associated Debye model (black dashed line). The isomer shift, δ , of the majority phase is also given.

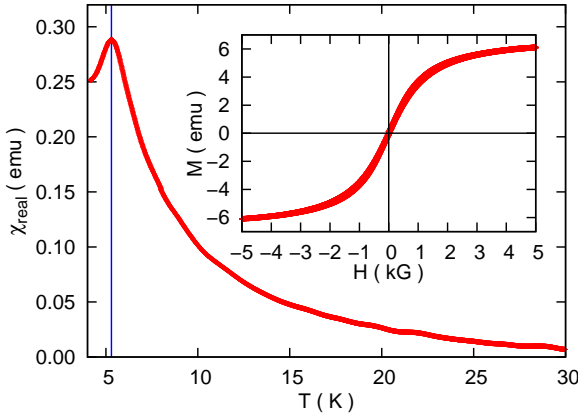


Figure 30: Temperature dependence of the ac magnetic susceptibility measured on cooling in sample in EuTiO_3 using an oscillating magnetic field with frequency $f = 20.4$ Hz amplitude $H_{\text{ac}} = 10$ G at $H_{\text{dc}} = 0$ G. Inset shows a $M - H$ curve measured on the same sample at 4.9 K with maximum applied magnetic field of $H_{\text{dc}} = 50$ kG.

below the antiferromagnetic transition temperature. As a result, within our instrumental resolution, both $\text{Eu}_3\text{Ti}_2\text{O}_7$ and Eu_2TiO_4 are not present in our sample.

5.4.3 Pair Distribution Function Analysis Of Neutron Diffraction

Pair Distribution Function analysis (PDF) probes local disorder in crystalline materials [178, 198, 199]. The PDF can be derived either from X-ray or neutron total scattering data with advantages and disadvantages described extensively by Egami and Billinge [200]. In contrast to Rietveld refinements, the diffuse scattering and other background contributions are of crucial importance because a Fourier transformation is applied to the total scattering function, in the former such contributions are treated phenomenologically. The main information extracted from PDF without further modeling is the interatomic distances, see Fig. 31b. However, europium is a strong neutron absorber [186] [186] which consequently introduces anomalous background in the total scattering as function of the scattering angle. Hence, the Fourier transformation of the total scattering function might introduce artifacts in the PDF which cannot be modeled. In addition, Ti has a negative coherent scattering length which results in negative peaks for the A, X -Ti correlations, where A and X are the perovskite sites. Fig. 31a shows such a case. Although all interatomic distances

were modelled successfully and the extracted parameters (lattice parameters, atomic displacement parameters) agree with the one extracted from Rietveld refinement, the goodness of fit is relatively high. Thus from such analysis, for peaks in PDF which are not easily distinguished from the transformation artifacts we cannot safely conclude whether there is an interatomic distance split accompanied by an atomic off-centering, see highlighted part of Fig.31b.

5.4.4 Gram - Charlier Expansion of Atomic Displacement Parameters

The refined Eu anharmonic parameters $D_{GC}^{ijkl}(r)$ at 110, 210, 295 and 360 K are given in the Table 6.

Table 6: Temperature dependent anharmonic refined parameters $D_{GC}^{ijkl}(r)$ of Eu atom in EuTiO_3 refined using the Gram-Charlier expansion

	Temperature (K)			
	320	295	250	180
$D_{GC}^{iii}(r), i = 1, 2, 3$	-426.0(13)	-375.6(12)	-329.8(11)	-88.7(11)
$D_{GC}^{ijj}(r), i \neq j = 1, 2, 3$	-65.7(8)	-67.5(6)	-69.2(7)	-35.1(4)

5.4.5 Nuclear Inelastic Scattering

Several experimental methods for probing lattice dynamics exist. However, access to the full Density of Phonon States (DPS), $g(E)$, is feasible only by inelastic neutron [201] or x-ray scattering [81]. In this work, nuclear resonance inelastic measurements which requires the existence of Mössbauer active isotope and synchrotron radiation were carried out. The extracted DPS between 110 and 360 K is given in Fig.32a. The ^{151}Eu DPS shows a prominent peak around 11.2 meV which does not shift to higher energies. We extracted using our macroscopic measurements of C_p , α_V , B and the Grüneisen rule [97] the Grüneisen parameter. Our estimation of γ at 290 K is, 1.3(1), in the same range with typical metallic compounds, $\gamma \simeq 2$. To elucidate the impact of the Grüneisen parameter on our measured DPS we used the vibrational frequency definition of the Grüneisen parameter, $\gamma = -\frac{d \ln E}{d \ln V}$, which relates the change in phonon mode energy to the change in volume. The estimated phonon mode energy shift, between 110 and 360 K using our measured $\frac{dV}{V} \sim 0.0025$ and our extracted average Grüneisen parameter of $\gamma = 1.3$ results in $\frac{\delta E}{E} \sim 0.004$. Therefore, the prominent peak, around 10 meV will not shift due to anhar-

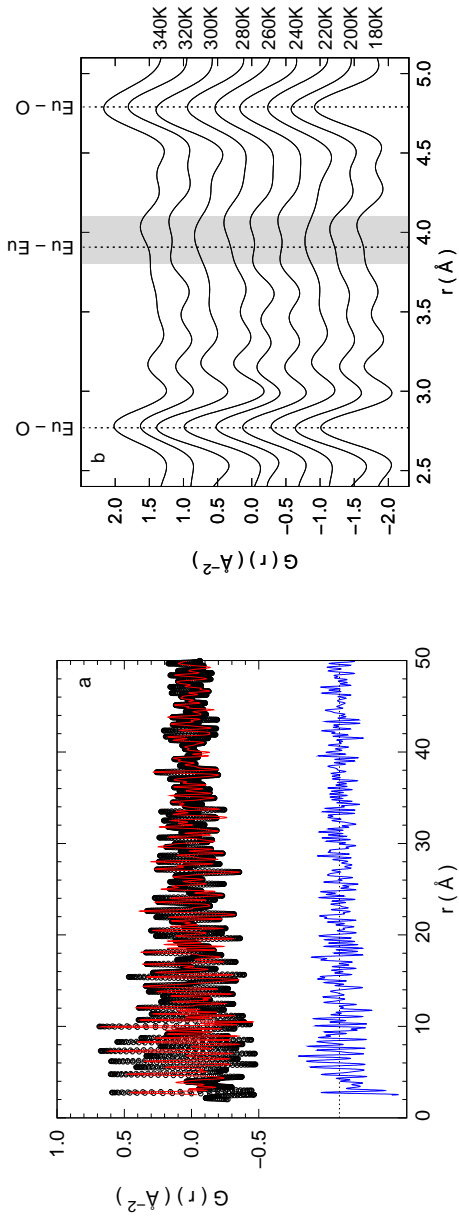


Figure 31: (a) Pair Distribution Function analysis (PDF) of neutron scattering data, $Q = 50 \text{ \AA}^{-1}$, at 300 K, the corresponding refinement (red line). The refinement residual (blue line) represents a fair refinement. (b) shows the first nearest neighbor distances (dashed line) and the region of interest (gray zone).

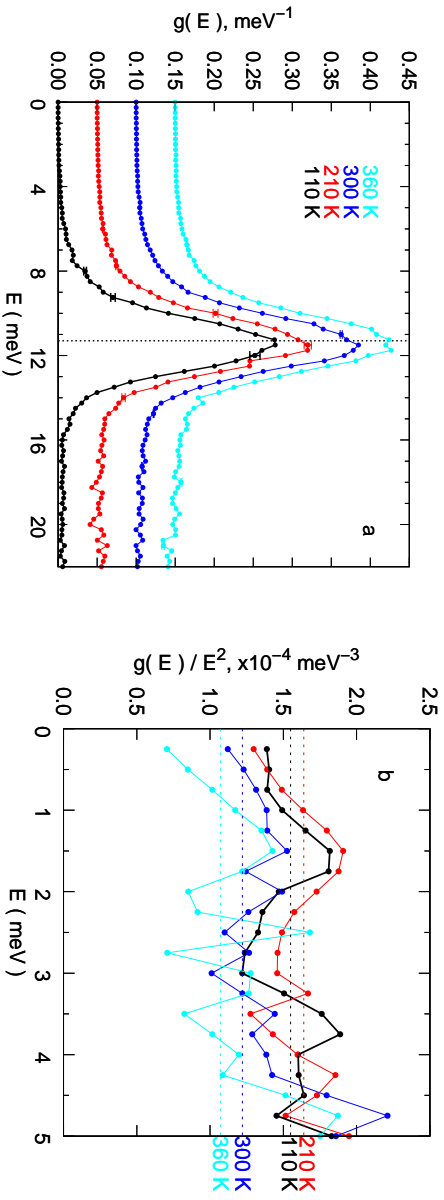


Figure 32: (a) ^{151}Eu projected density of phonon states at 110, 210, 300 and 360 K (typical errorbar are given), the curves were equally shifted for clarity; (b) shows the first 5 meV of the reduced ^{151}Eu projected density of phonon states, $g(E)/E^2$, and the related Debye level (dashed lines).

monicity more than 0.04 meV. Such energy mode shift is currently resolution limited.

In the long wavelength limit, in this work assumed below 4 meV, the average speed of sound, v_s , can be extracted from the DPS using: $\lim_{E \rightarrow 0} \frac{g(E)}{E^2} = \frac{M_i}{2\pi\hbar^3 \rho v_s^3}$ [10] where M_i the isotopic mass and ρ the mass density. A linear fit of the $g(E)/E^2$, below 4 meV, between 110 and 360 K is given in Fig. 32b. The corresponding speed of sound is included in the main text.

CONCLUSIONS

Lattice dynamics measurements using nuclear inelastic scattering by ^{125}Te and ^{121}Sb show that Bi_2Te_3 is acoustically softer than Sb_2Te_3 mainly due to the mass ratio of Bi and Sb. The softening of the low energy modes likely has an influence on the thermal conductivity and thus favorably impacts the thermoelectric properties. An additional 34% force constant softening of the Sb-Te bond with respect to the Bi-Te bond is required to explain the observed high energy optical softening of Sb_2Te_3 compared to Bi_2Te_3 . This observation might be related to the appearance of induced phase switching preferably in antimony than in bismuth bearing chalcogenides. Low temperature heat capacity measurements indicate the existence of antisite defects in both compounds and further thermal conductivity measurements could clarify their resonant interaction with thermal phonons. Close to room temperature a substantial deviation of the measured heat capacity from the Dulong - Petit law is observed only in Sb_2Te_3 and attributed mainly to self doping. It appears that for thermoelectrics, as it was also suggested for phase change materials [202], the role of the elemental binding should be carefully investigated.

Combined lattice dynamics characterization using nuclear inelastic scattering by ^{121}Sb and x-ray diffraction on an elemental modulated Sb_2Te_3 show that in Sb_2Te_3 the main features in the density of phonon states are related to the layered of the crystallographic structure. In the basal plane crystal growth is rapidly growing. Reduction in macroscopically measured thermal conductivity on similar samples might be related primarily with reduction in the acoustic cut-off energy. The interlayer force constant shows an interlayer distance dependence.

Microscopic lattice dynamics measurements on a 56 nm diameter array of nearly stoichiometric Bi_2Te_3 nanowires using nuclear inelastic scattering by ^{125}Te has been performed for first time. The extracted density of phonon states shows that cross sectional confinement leads to a 29% reduction in the speed of sound compared to bulk counterpart which results in a 50 % reduction in the lattice part of thermal conductivity and thus favourably impacts the thermoelectric and phase change properties. No effect in the phonon lifetime and the acoustic cut-off energy has been measured related to confined dimensions.

The behaviour of the lattice dynamics in EuTiO_3 has a resemblance to the lattice dynamics in SrTiO_3 , the atomic delocalization in phase change materials [102] and the local disorder as well as the lattice dynamics in PbTe

[203, 204]. In the the aforementioned cases the associated potential energy is considered as a multi-valley surface, the number of valleys depending on the number of short range coexistent phases, with drastical impact on the macroscopic thermal conductivity [5]. Hence, the phenomenon observed could potentially be characterized as a confined rattling between well defined minima in the potential energy.

Part II

RESONANT ULTRASOUND SPECTROSCOPY

DEVELOPMENT OF A SMALL SAMPLE RUS SETUP

The general foundation of resonant ultrasound spectroscopy for measuring elastic constants of solids is given in the introduction. In this chapter, a more elaborated description of resonant ultrasound spectroscopy will be given dedicated to measurements performed on small samples and thin films.

On the one hand, macroscopic large samples are not always available for such measurements. However, samples in the range of a few mm^3 can be synthesised in almost all cases. It is thus aim of this chapter to provide the basic information for constructing and operating an instrument which can reliably measure the elastic constants of small samples based on the resonant ultrasound spectroscopy technique.

On the other hand, thin film growth is an interesting field of science and technology. Typically 'thin' films have less than $1 \mu\text{m}$ thickness which implies that even if the substrate thickness is in the range of a few hundred micrometers¹ the information extracted from the film can be considered as a perturbation of the information provided by the substrate. Hence, the present chapter will discuss elastic constants measurements on films deposited on substrates.

7.1 MECHANICAL RESONANCES OF SMALL SAMPLES AND THIN FILMS

Measuring the mechanical resonances of small samples is generally not very problematic, especially if an experimental setup exists for relatively large samples. However, a careful investigation on mechanical resonances of small samples reveals that special attention should be drawn on the geometry of the sample as well as on the experimental setup in order to prevent interference with the measured data. The feasibility of a spectrometer made of solid transducers, either LiNbO_3 or PZT, has been shown in several cases [46, 205]. Solid transducers add an external damping force to the oscillating sample due to the weight of the transducers themselves and the weight of the transducer supporting scaffolding. Several designs have been realised which try to reduce this contribution [206]. Although the damping force does not change during measurement and is reproducible for similar sample mountings, it should not be neglected. The first 12 normal modes of a sample with plate like

¹ when the thickness of the substrate is less than few micrometers, it is in general not rigid and cannot be handled easily.

geometry, dimensions $0.05 \text{ mm} \cdot 1.1 \text{ mm} \cdot 1.0 \text{ mm}$, are shown in Fig. 33. All shown normal modes depict similar vibrations, namely surface bending modes, which on the one hand are sensitive to transducer loading and on the other do not provide information about the elastic constants related to all different kind of vibrations. In fact, the non-surface bending modes are shifted to higher frequencies.

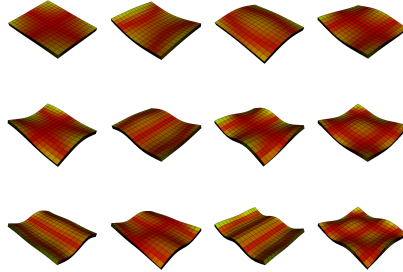


Figure 33: The first 12 normal modes of a sample with plate like geometry, dimensions $0.05 \text{ mm} \cdot 1.1 \text{ mm} \cdot 1.0 \text{ mm}$. The figure was reconstructed from the calculated eigenvectors using Mathematica. The red areas denote high strain regions.

In order to circumvent the problem related to loading effects either a non-plate like sample should be prepared or the transducer loading should be reduced to its minimum value and the measurement should be extended to a broader frequency range. In this study we followed both approaches simultaneously. The transducers of our spectrometer have been prepared from a flexible piezoelectric polymer². A precise measurement of the minimum transducer loading when the sample is held between the transducers has not been carried out, however, we estimate that the minimum applied loading should be at least two times the weight of the sample. In addition, special care was taken to avoid plate like geometries.

In the case of a film deposited on a substrate its mechanical resonances are defined by the material properties of both the substrate and the film. Normally, a deposited film causes a shift of the substrate's natural resonances. This observation can be extracted from the so called "forward problem" or the solution of the equation of motion. For a ratio of substrate to film thickness in the range of 1000, Gladden [208] calculated the minimum resonance frequency shift and found it to be around 600 ppm. He sets this ratio as the lower limit for frequency shift detection. The detection of the frequency shift does not

² PVDF: polyvinylidene fluoride is also known by its trade name Kynar [207]

depend only on the deposited material. Primarily it depends on the so-called quality factor, Q , which is defined as the FWHM of the Lorentzian profiles fitted to the spectra or the inverse quality factor, $Q_i = 1/Q$. Hence, the higher the Q the better is the measurement resolution. It has to be mentioned that Q is a function of the sample's internal friction expressed in dissipation phenomena. There are many excellent works, both theoretical and experimental, which are dealing with dissipation phenomena [209]. All elastic theory presented herein has neglected these dissipation phenomena.

7.2 SAMPLE PREPARATION

There are several ways to reduce the painstaking labor of preparing exact geometrical shape on a sample with approximately $\sim 1 \text{ mm}^3$ volume. First, a simple geometrical shape should be realised. Complex geometrical shapes will not give different physical results but their realisation will be time consuming, if not unrealistic. Throughout this study a rectangular parallelepiped geometry is adopted.

One of the easiest ways to shape a rectangular parallelepiped geometry of a single crystalline sample is to cleave the sample parallel to an easy crystallographic direction. In this case, the crystallographic direction should be either known or determined using a Laue camera. Apart from the Laue camera a diamond scribe fixed on a micropositioning stage with possibility of movement in two perpendicular directions and rotation as well as a guillotine are of essential use. First the sample is firmly fixed on the micropositioning stage with the predetermined crystallographic direction parallel to the positioning stage movement. For fixation a small vacuum pump connected to the base of the stage might be used. After that a grid is carved using the diamond tip on the sample surface with the required dimensions. Last, using the guillotine the carved part is separated from the rest of the wafer. In case cleaving is successful, the sample roughness as well as the parallelity of the sample's faces are the best macroscopically achievable.

The second more time demanding alternative is to polish or cut the sample to the required dimensions. Single crystals might also be polished, however, the results are rarely comparable with cleaving the sample. Nevertheless, if a polycrystalline sample is available polishing is the only way to achieve the required shape. In this study, we tried several times to shape the sample using a fine wire saw instead of polishing. However, the result has never been satisfying and in all cases a further polishing step was conducted. When the sample has a prepolished or relatively flat face it is placed face down on a polishing sample holder so that the opposite face after polishing will be parallel to the first one. The parallelity of the polishing surface is further

ensured during polishing with teflon shims which are part of the polishing holder, see Fig. 34. The sample is initially fixed on the holder using a relatively thin film of any commercially available glue thinned with acetone. For further mechanical support the sample is immersed in molten wax. After the wax is solidified the polishing procedure starts. In this study, thin plastic diamond coated paper with roughness between 1 and 15 μm and a bare sand paper have been used. The polishing paper is placed on a straight smooth lapping disk fixed to a rotating with variable speed polishing table. During the polishing procedure the sample holder is manually moving on the polishing platform in an irregular manner in order to avoid surface scratches and grooves along one direction. The polishing platform is constantly dispensed with a water based liquid for smoother and constant temperature polishing. When the first rough polishing is finished, the procedure is continued with a smother polishing paper. Once two parallel faces exist, the sample is removed from the sample holder using acetone and fixed between two parallel steel blocks³ of variable gap which are located on the top of a similar sample holder. The sample is covered with wax and the procedure is repeated until the third perpendicular face is created. The remaining three sides are polished in the same way by rotating the sample so that a rectangular parallelepiped shape is given. A final cleaning of the sample is crucial in order to remove all remainings of glue and wax.



Figure 34: A snapshot during polishing of a bulk polycrystalline sample mounted on the polishing holder. Inset: a figure of the 'L' shape which is mounted on the sample holder to produce the third perpendicular face, see text. Courtesy: Forschungszentrum Jülich.

Three main categories of sample imperfections exist after the sample preparation:

1. Surface roughness.

³ An even more robust sample holder might have an "L" shape which provides a 90 deg angle

Surface roughness is usually not important because the wavelength of the induced mechanical waves is much longer than the roughness of the sample surface which is equal to the roughness of the diamond coated paper, i.e. several μm . The low roughness is ensured during the polishing procedure in two ways. Firstly, a series of grinding papers are used, from the rougher to the smoother. Secondly, a pseudorandom movement of the sample holder during polishing is realised which excludes surface scratches and grooves.

2. Visual imperfections.

Every sample should be checked under a microscope for visual imperfections such as chips, rounded or broken corners etc. These imperfections are easy to see.

3. Non perpendicular faces.

Although every sample is being checked visually under a microscope against a ruled paper before measurement, the probability that it has non perpendicular faces, see Fig. 35, is high, because on small samples small deviations might escape detection. According to Spoor [210], tilts of a few tenths of a degree could produce frequency shifts in the tenth of a percent. Such artificial frequency shifts are significant since the agreement between theoretically calculated and experimentally measured frequencies is typically better than 0.5 %.

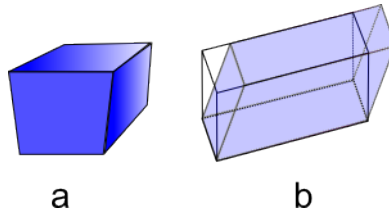


Figure 35: Indicative types of geometry errors during the rectangular parallelepiped sample preparation. (a) shows a trapezoid and (b) a skewed rectangular parallelepiped.

7.3 EXPERIMENTAL SETUP

7.3.1 *Small sample cell*

The bare part of the experimental setup, shown in Fig. 36, was designed to fit in the Quantum Design cryostat (QD-PPMS) and is a modification of

an already existing similar sample holder designed by Gladden [208]. The construction material was brass. Two wagons are in contact with the flattened wall of the cylindrical cell. Parallel rods are guiding the two moveable wagons. The position of the left wagon in Fig. 36b is adjusted with the help of a spring and a lead screw. The right wagon is fixed to the wall of the cylinder. On the top of the wagons insulating transducer holders, i.e. polyimide⁴, have been fixed using two stainless steel screws. The piezoelectric transducers are placed on the insulating holders with the help of two stainless steel stripes fixed on both sides of the transducer holders. For room temperature measurements an additional cylindrical Faraday cage, not shown here, was created which hosts the measuring setup.

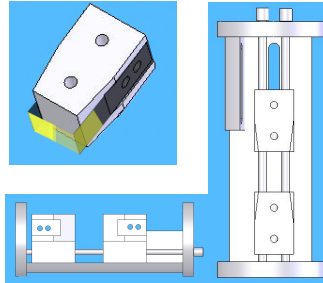


Figure 36: The transducer holder and the flexible transducer, see text, is shown in the left top figure. The bare RUS cell for small samples is shown in side view, bottom left, and top view perspective, bottom right.

7.3.2 Transducer preparation and mounting

The active part of the measuring setup is composed of two identical transducers. In this study, the transducers were constructed by PVDF which is a well known piezoelectric polymer [212]. The polymer was purchased from Goodfellow with a thickness of $9\ \mu\text{m}$ and lateral dimensions of $25 \cdot 25\ \text{mm}^2$. The thickness was chosen such that it is robust enough to survive many measurement repetitions without damage and that the resonances due to the polymer are outside of the measuring regime. At the same time the transducers were flexible enough in order not to load the sample. Initially, the polymer was not in shape for applying the required voltage. The purchased polymer was metallised from both sides and is was cut into the proper dimensions to

⁴ polyimide is also known by its trade name vespel[211]

fit into the spectrometer. The metalisation of PVDF, see Fig. 37, was tricky because of its thermomechanical properties and the fact that the upper glass transition occurs at 333 K. This particular glass transition corresponds to a gradual crystalline to amorphous transformation with phase intermixture which depolarises the already uniaxially polarised film [213]. In order to avoid such effects we used a very low power, ~ 1 W, magnetron sputterer and a liquid nitrogen cooled sample holder to avoid any heat accumulation. The temperature on the sputtering surface has been probed using non reversible temperature labels and during the procedure did not exceed 300 K. The purchased piece of polymer was initially rinsed with distilled water and placed in an ultrasonic cleaner for 5 min. It was subsequently dried in 10^{-3} mbar vacuum. A special mask for metalisation was created from thin cylindrical steel plates, diameter: 45 mm, thickness: 0.5 mm, such that an open area of 12 mm \cdot 22 mm was facing the sputtering target from both sides of the film. The open area had an overlap of 1 mm \cdot 22 mm (active area) perpendicular to the polarization direction. The same procedure as for cleaning the PVDF film was also followed for cleaning the metalisation mask. The PVDF film was fixed in place inside the metalisation template with a tiny amount of vacuum grease at the film's edges and the whole sandwich was clamped on an aluminum sample holder. We sputtered 40 nm of Cr followed by 300 nm of Ag on both sides of the film. The intermediate chromium layer improves the adherence of the silver to the PVDF. When the PVDF film had been metallised we carefully removed it from the mask, cleaned the remaining vacuum grease from its edges using a small amount of methanol and placed it on a clean microscope slide with tape at the ends. From the metallised polymer, see Fig. 37, we cut two stripes along the direction of polarization using a new razor blade at low angle with lateral size of 1 mm \cdot 22 mm. The transducers of our spectrometer, and the remaining part was stored in a desiccator under vacuum for future use. The PVDF transducers are attached to the transducer holders using a conductive epoxy which cures at room temperature. Once the epoxy is dried, the stripes can be tensioned by inserting rubber pieces between the holders and the supporting block. The electrical connections to the transducers can be realised on the metallic holders. The side which is in contact with the sample should always be grounded and the other side should be connected either to the driving AC electric field, transmitter, or to the receiver.

7.3.3 Sample mounting

The mounting of the sample should be preferably on opposite corners, see Fig. 38, since the corners of a rectangular parallelepiped are never nodes

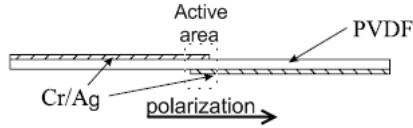


Figure 37: A scheme of the metallised PVDF transducer is shown where the PVDF, the metallised sides and the active area are shown.

and thus all normal modes are detected. To circumvent this difficulty, a USB microscope connected to a color display, a micromanipulator and a pair of vacuum tweezers have been utilised. The vacuum tweezer consists of a small vacuum pump connected to a cylindrical holder. The front end of the holder is extended using a medical injection needle with various sizes and tip shapes. One vacuum tweezer is firmly fixed to the micromanipulator which allows precise control of movement in all directions. The other vacuum tweezer is a pick up tweezer for transporting the sample before mounting. The RUS cell is positioned with the transducers parallel to the fixed vacuum tweezer. The sample to be measured is put on the fixed vacuum tweezer and driven with the micromanipulator in the middle of both transducers. After that, one of its corners is contacted to the fixed transducer. The moveable transducer is adjusted using the leading screw such that the opposite sample's corner touches the active area of the moveable transducer. The whole procedure is inspected using the USB camera. A snapshot of the procedure is given in Fig 38. Once the sample is positioned correctly, it should stay in place even after switching of the vacuum in the holding tweezer. To ensure that the sample will stay in place during spectrometer handling and transportation a gentle crash test is performed when the sample cell is still fixed on the sample mounting stage. It is not uncommon that the sample mounting is not correct and the sample will either fall off or move from the active area.

7.4 MEASUREMENT CONSIDERATIONS AND POSSIBLE ERRORS

The basic scheme of the measuring setup is given in Fig. 7 and is not repeated here. Nevertheless, we remind that it consists of a piezoelectric transmitter connected to a function generator and an identical piezoelectric receiver connected to a lock-in amplifier. The lock in amplifier detects a signal locked to the frequency of excitation [214]. However, due to the small dimensions of the sample the distance between the two parallel semi-metallised PVDF transducers is short and thus electrical cross talk is troublesome when sample resonances are weak. To avoid the appearance of electrical cross talk either the transducers should be fully metallised, i.e. self shielding, or a piece of

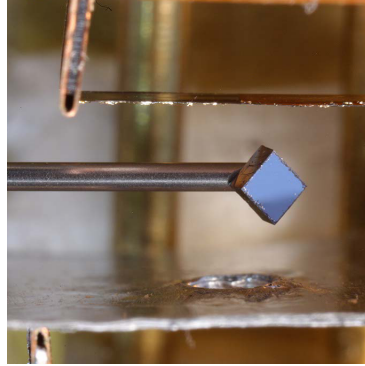


Figure 38: A snapshot of the sample mounting between the transducers using the vacuum tweezer. Courtesy: Forschungszentrum Jülich.

grounded shield should be put between the transducers, i.e. external shielding. The shelf shielding approach induces an extra difficulty in avoiding short circuits during electrical connection due to the small thickness. The external shielding approach introduces a difficulty in putting the sample between the active area of transducers. However, this is approach of electrical shielding was selected. Special attention should be given to the thickness of the cross talk shield. It should be flexible enough in order to align it parallel to the fixed transducer but thick enough to prevent cross talk. We created an aluminum cross talk shield with thickness of 0.5 mm and a center hole slightly larger than the half diagonal of a typical sample. We fixed this additional metallic piece between the transducers, very close to the steady transducer and oriented it such that the hole is only above the active transducer area.

Once the sample is loosely placed between the active area of the transducers through the hole in the cross talk shield, the measurement is ready to start. A first rough estimate of the frequency range to be scanned is important. In order to obtain it, the sample's dimensions, density and estimated elastic constants are needed to solve the so-called forward problem. In principle, a very rough estimate of the frequency range to be scanned for a sample with volume between 1 and 10 mm³ is between 100 KHz and 3 MHz. In this study, all measurements performed at room temperature were conducted with the spectrometer enclosed in a cylindrical aluminum Faraday cage having common ground with the rest of the electronic equipment. In case the measurement is conducted in the QD cryostat a similar Faraday cage enclosure is applied, as shown in Fig. 39.

RUS is a resonant technique, hence, the main errors are related to sample preparation and loading, and to data treatment, and not to the measurement

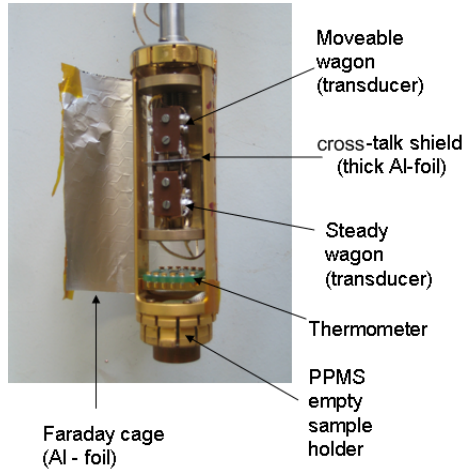


Figure 39: Resonant ultrasound spectrometer for small samples mounted in the QD cryostat sample holder.

procedure itself. A mathematical model which describes the shape of the sample is directly involved in the data analysis. Thus, the larger the deviation from the assumed model the larger the systematic error in the output. It is, hence, of use to identify the likely errors in the extracted results.

The effect of transducer loading on sample resonant frequencies and quality factor is an important issue in any resonant ultrasound spectroscopy experiment. It is important to know how frequency and Q vary between mountings. To address this question, we mounted one GaAs sample with dimensions: $1.0 \text{ mm} \cdot 1.1 \text{ mm} \cdot 0.5 \text{ mm}$ between the PVDF transducers and externally increased the applied tension on the transducers by putting different wedges between the transducer holders and the supporting insulating scaffolding. This procedure reliably simulates the impact of different sample orientation and squeezing force applied to the sample. The results are shown in Fig. 40. Although the applied tension has not been explicitly measured, it can be seen that when higher tension is applied to the polymer transducers the measured resonance is slightly shifting to higher frequencies and becomes more visible. After this experiment the transducers have been irreversibly damaged. The metallisation film was scraped off from the polymers surface due to extreme tension. They have been exchanged with a new set of transducers. Note that the observed deviations in Fig. 40 both in frequency and Q are the effect of transducer loading and not uncertainties in the frequency determination. A typical resonance shift produced by transducer loading is $1/1000$ of the

measured frequency. This ratio, although small enough plays an important role in the determination of elastic constants on a thin film since it is in the same range as the ratio of the minimum film and substrate thickness. Thus, reproducibility in sample mounting which will in turn give reproducible results is of crucial importance.

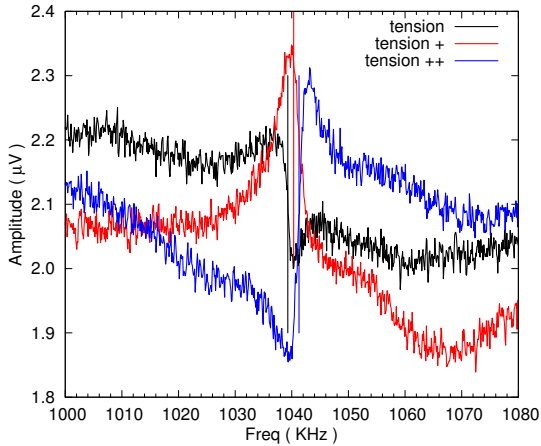


Figure 40: Sample loading effect in determination of resonant frequency in RUS measurement on a GaAs single crystalline sample with dimensions 1.0 mm · 1.1 mm · 0.5 mm. The central frequency is indicated by vertical line.

Last but not least, measurements under controlled external conditions are of essential importance. Temperature effects in resonant ultrasound spectroscopy arise both due to temperature variation of elastic constants as well as due to thermal expansion or contraction. A usual thermal expansion coefficient is $\sim 10^{-5} \text{ K}^{-1}$ and does not contribute significantly in the measurement. Hence, apart from compounds with exceptionally high thermal expansion coefficients, the temperature dependence of resonant ultrasound spectra is due to the temperature dependence of elastic constants. Fig. 41 shows a resonance recorded on the same GaAs sample as the one recorded on Fig. 40 between 275 and 295 K. The observed resonance shifts towards higher frequencies when the temperature increases. For a temperature change of 20 K the observed relative frequency shift is 0.2 %.

7.5 COMPUTATION

The discussion on computing the elastic constants from resonant ultrasound spectroscopy measurements is mainly focused on measurements performed

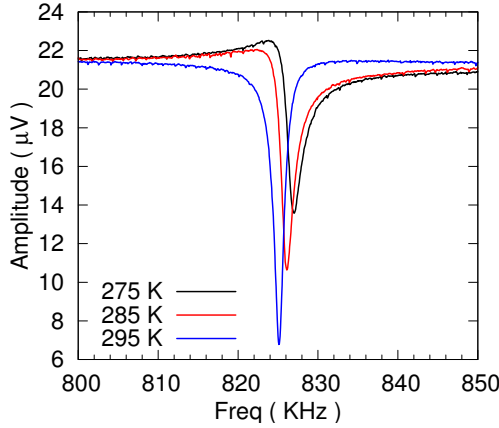


Figure 41: Temperature dependence of a resonance recorded between 275 and 295 K on the same GaAs single crystalline sample used in Fig. 40.

on small single crystals with cubic symmetry. The subcase of polycrystalline samples, i.e. elastically isotropic, will also be discussed.

The full elastic tensor can be extracted by performing resonant ultrasound spectroscopy on single crystals. The elastic tensor is defined relative to a coordinate system. In the general case of a single crystalline sample, there are two sets of coordinate systems which should be taken into account. One is the crystallographic coordinate system in which the system crystallises and the other is the coordinate system in which the sample vibrates and its shape is described. As it may be guessed, the crystallographic coordinate system is of fundamental importance in describing physical phenomena. When this coordinate system does not coincide with the one defined by the sample shape, an appropriate rotation should be applied. In this work, this is accomplished by applying an Euler angle rotation using the Arfken [215] convention to the elastic tensor in order to transform it from the sample's shape coordinate system to the crystallographic coordinate system. The rotation matrix given in Table 7 implies that the initial coordinate system (x, y, z) is rotated with respect to the final coordinate system (x''', y''', z''') using successive rotations by angle α , which defines a rotation around the initial z -axis which results in (x', y', z') . Angle β defines a rotation around the new y' -axis which results in (x'', y'', z'') and γ is the final rotation around the new z'' -axis which results in (x''', y''', z''') .

The algorithm written in Fortran 77 for calculating the elastic tensor and refining the elastic tensor of a cubic symmetry single crystal with crystallo-

Table 7: Matrix for rotating a coordinate system (x, y, z) to (x''', y''', z''') using the angles of rotation α , β and γ as defined in the text.

$$R = \begin{pmatrix} \cos\gamma \cdot \cos\beta \cdot \cos\alpha - \sin\gamma \cdot \sin\alpha & \cos\gamma \cdot \cos\beta \cdot \sin\alpha + \sin\gamma \cdot \cos\alpha & -\cos\gamma \cdot \sin\beta \\ -\sin\gamma \cdot \cos\beta \cdot \cos\alpha - \cos\gamma \cdot \sin\alpha & -\sin\gamma \cdot \cos\beta \cdot \sin\alpha + \cos\gamma \cdot \cos\alpha & \sin\gamma \cdot \sin\beta \\ \sin\beta \cdot \cos\alpha & \sin\beta \cdot \sin\alpha & \cos\beta \end{pmatrix}$$

graphic axes rotated with respect to the sample's axes is given in the Appendix. This code is a modification of the prototype code written by Gladen [208]. It was tested by performing several rotations around all axis and evaluating the results. The required input is limited to the dimensions of the sample, the initial values of the elastic constants, the Euler angles (for the forward problem) and the measured resonance frequencies in strict ascending order (for the inverse calculation). When a resonance is not identified in the measured spectra it should be excluded from the refinement by setting the weight factor to zero. Special attention should be drawn to the fact that a sufficient amount of resonances has to be measured. Migliori and Sarrao [68] set the limit of detected resonances to five times the number of parameters which will be refined. The output of this program can be either the calculated resonance frequencies (forward problem) or the refined elastic constants (inverse problem).

From the information technology point of view, the consequence of rotating the coordinate system is that the calculated elastic tensor is not any more symmetric along its diagonal and cannot be reduced in block diagonal submatrices. The interested reader is referred to Ref. [68]. More computing power is required for the minimisation of the Langrangian but this is not an issue with up-to-date personal computers.

For the measurement of a polycrystalline sample the whole procedure is simpler. Only two independent elastic constants, namely C_{11} and C_{44} , in this case $C_{12} = C_{11} - 2C_{44}$, exist. The crystallographic coordinate system is not defined and the Euler angle must be set to zero. The required modifications in the algorithm are given in the appendix.

The goodness of fit of the refinement can be judged by two parameters, the average error of resonance position and the RMS error. Both parameters are calculated by the program and given in the output file. A reasonable refinement should result in an RMS error around 0.2 %.

7.6 PROOF OF PRINCIPLE AND OUTLOOK

As a proof of principle, measurements on GaAs single crystalline samples were performed. Approximately 100 samples have been prepared from a GaAs wafer with diameter of 10 cm and 0.5 mm thickness oriented in the $\langle 0\ 0\ 1 \rangle$ direction following the procedure described in the sample preparation paragraph. The typical dimensions of all samples were 1.0 mm · 1.1 mm · 0.5 mm. To determine the Euler angles, i.e. the relative rotation of the crystallographic axes with respect to the sample axes, Laue diffraction has been carried out. The obtained diffraction pattern is given in Fig. 42. From such pattern the Euler angles have been determined using the program OrientExpress[216]

and found to be $\alpha = 45$ deg, $\beta = 0$ deg and $\gamma = 0$ deg, which means that the $[1\ 1\ 0]$ is along one side and the $[1\ 0\ 0]$ is along the diagonal of the sample. Similar measurements have been performed on several samples from the same batch and the extracted Euler angles are in excellent agreement.

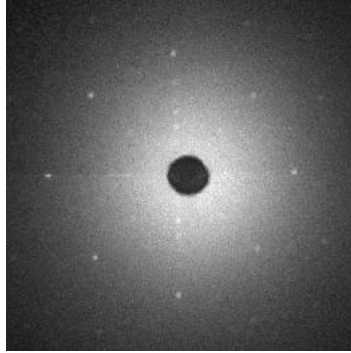


Figure 42: A Laue diffraction pattern on a GaAs single crystalline substrate

Several scans between 500 KHz and 4 MHz at 295 K inside the QD cryostat have been performed. The frequencies of the resonances have been extracted by fitting the spectra close to the resonances with a Lorentzian profile. The first 22 resonance frequencies in strict ascending order, see column 1, are shown in column 2 of Fig. 43 in MHz. In column 3 the theoretically expected frequencies are shown. The relative error is shown in column 4 and the weighting factor is depicted in column 5. For illustration reasons, the first and the last resonances have been excluded from the refinement. In columns 6 to 8 the dependence of a particular resonance to the extracted elastic moduli are shown. The output of the elastic constants refinement is given in the bottom of Fig. 43. The elastic constants of GaAs at 295 K are $C_{11} = 117$ GPa, $C_{12} = 53$ GPa and $C_{44} = 59$ GPa and typical errorbar is given in Fig. 44.

We performed temperature dependent measurements between 100 and 300 K. Our measured temperature dependent elastic constants are given in Fig. 44 and are in good agreement with reference data obtained from Ref [69]. C_{12} shows an increased dispersion of the measured data due to the fact that this particular elastic modulus does not strongly depend on any of the measured resonances.

Apart from measuring elastic constants on small samples the constructed spectrometer within this framework is capable of measuring elastic constants of thin films. The elastic constants of thin films cannot be measured in situ during deposition using the approach described in this thesis. Therefore, the measurement should be conducted in two separated steps. In the first step,

```

# GaAs w/o film (Sample C)
Free moduli are c11, c12, c44
#      fexp      ftheor      %err      wt      df/dc11      df/dc12      df/dc44
1      0.842958    0.831502    1.378      EXC      0.00      0.00      0.00
2      1.379157    1.381052    -0.137     INC      0.42      0.11      0.47
3      1.493971    1.491859    0.142      INC      0.68      0.31      0.01
4      1.620605    1.612398    0.509      INC      0.45      0.11      0.44
5      1.626666    1.633910    -0.443     INC      0.62      0.25      0.14
6      1.842147    1.829296    0.702      INC      0.53      0.21      0.26
7      1.893742    1.889092    0.246      INC      0.62      0.25      0.12
8      1.978434    1.968728    0.493      INC      0.50      0.19      0.31
9      2.127001    2.139754    -0.596     INC      0.58      0.20      0.23
10     2.259016     2.265334    -0.279     INC      0.48      0.17      0.34
11     2.360000     2.367222    -0.305     INC      0.41      0.15      0.45
12     2.606358     2.614768    -0.322     INC      0.61      0.26      0.13
13     2.617128     2.625203    -0.308     INC      0.27      0.05      0.68
14     2.719825     2.724688    -0.178     INC      0.17      0.06      0.76
15     2.732082     2.732713    -0.023     INC      0.59      0.25      0.16
16     2.793247     2.778660    0.525      INC      0.55      0.22      0.23
17     2.864199     2.866523    -0.081     INC      0.65      0.28      0.06
18     2.894568     2.895133    -0.020     INC      0.21      0.04      0.76
19     3.177155     3.171636    0.174      INC      0.44      0.12      0.44
20     3.343751     3.338005    0.172      INC      0.32      0.13      0.55
21     3.354220     3.355824    -0.048     INC      0.61      0.27      0.11
22     3.374542     3.378857    -0.128     EXC      0.00      0.00      0.00
Avg error of included peaks= 0.285

      c11      c12      c44      (%GPa)
1.1752  0.5385  0.5907

      d1 (cm)      d2 (cm)      d3 (cm)
0.10020  0.11110  0.04940

      alpha (deg)      beta (deg)      gamma (deg)
45.0      0.0      0.0

% RMS Error= 0.31220
% Change= 0.00000
    
```

Figure 43: The output of the elastic constants refinement on a GaAs bare substrate.

the substrate should be characterised under controlled external conditions using RUS. All mechanical resonances should be recorded and the elastic constants should be extracted as precisely as possible. After film deposition the sample should be characterised again under exactly the same conditions. It is crucial that before and during film deposition the substrate is handled with great care as any slight chip or impurity adhering to the surface may perturb the resonances and obscure the effect of the film. It is also important that the sample mounting in the RUS cell before and after film deposition is similar.

The procedure for extracting the elastic constants of a thin film with thickness 1/1000 of the thickness of the supporting substrate is sensitive to error propagation and thus it should be corrected. As it is shown in Fig. 43 the relative error, ϵ_i , of any experimentally determined resonance i with respect

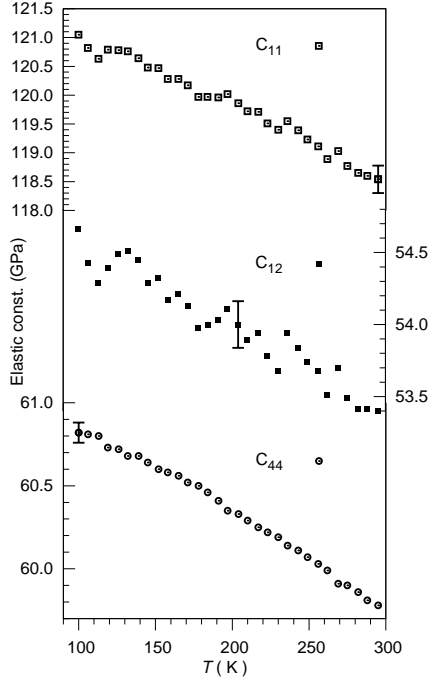


Figure 44: The elastic constants of GaAs between 100 and 300 K measured using the RUS cell for small samples constructed in this work

to the calculated one from the resulting elastic constants is given in the third column. The average error of all resonance frequencies is 0.285 %. A rescaling applied to all resonances measured on the substrate plus deposited film is required since the frequency shift due to the film is in the same order of magnitude as the numerical error resulting from the refinement procedure. Hence, the rescaling of the film's resonances should be realised according to $f_{\text{cor}}^{\text{film}}(i) = (1 + \varepsilon_i) f_{\text{raw}}^{\text{film}}(i)$. In case the frequencies are not corrected, the program will essentially fit the residual errors from the substrate fit by adjusting the film's elastic constants. It is important to note that in the film fitting session, all substrates parameters and the film thickness are kept fixed. The only parameters allowed to vary are the elastic constants of the film.

We precharacterised a series of GaAs substrates using the ultrasonic spectrometer and then sputtered an amorphous SnSb_2Te_4 film of 1 μm thickness. We observe a resonance shift to lower frequencies due to presence of the film, see Fig. 45. However, the extracted elastic constants, $C_{11} = 112(1)$ GPa and $C_{44} = 57.3(5)$ GPa, are not in agreement with the elastic constants

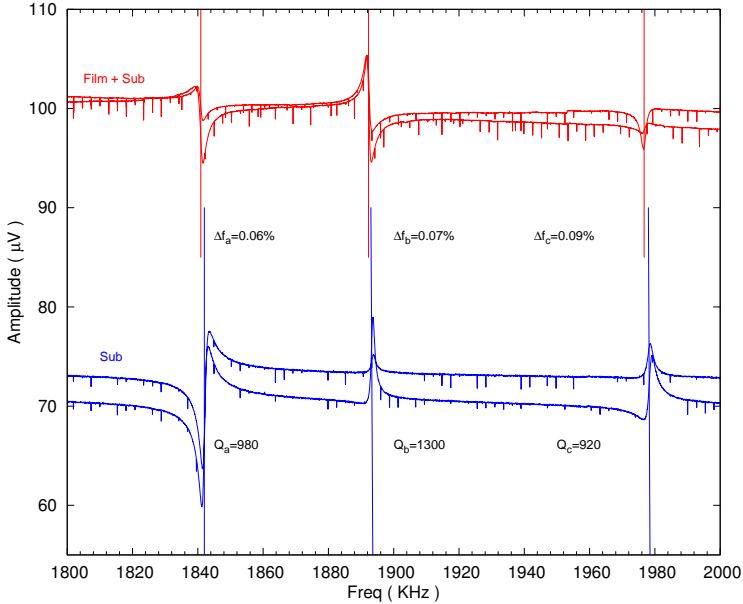


Figure 45: A comparison of two RUS spectra measured on a bare substrate and two spectra measured on the same substrate covered with SnSb_2Te_4 film.

extracted of the isoelectronic compound GeSb_2Te_4 , $C_{11} = 31(2)$ GPa and $C_{44} = 9.8(5)$ GPa measured by Brillouin light scattering [217]. In order to directly compare the reference data on GeSb_2Te_4 with data obtained in this work we sputtered a $5 \mu\text{m}$ amorphous film of GeSb_2Te_4 on GaAs. The observed resonance shift was proportional to the film thickness, however, the extracted elastic constants did not converge to the reference data. We, thus, suspect that there is a flaw in the algorithm dedicated to the extraction of the elastic constants of thin films which should be revised for future use.

7.7 CONCLUSIONS

We developed a resonant ultrasound spectrometer based on flexible piezoelectric transducers for extracting the elastic constants of small samples, either poly- or single-crystalline, and thin films deposited on substrates. The apparatus was tested both at room temperature as well as in a cryostat between 100 and 300 K. The elastic constants of several $\sim 1 \text{ mm}^3$ GaAs single crystals were measured between 100 and 300 K and are in very good agreement with

reference data. Resonance shifts proportional to film thickness have been identified when thin films are deposited on substrates. However, an algorithm problem which is still not clarified prevents the extraction of elastic constants of thin films.

7.8 APPENDIX

The basis of the algorithm for extracting the elastic constants of a solid is adjusted from the one obtain by Gladden [208]. In this work, we take the algorithm for extracting the elastic constants of a single crystal of cubic symmetry with rectangular parallelepiped shape as a basis and we modify accordingly for all other cases, i.e. polycrystalline sample with rectangular parallelepiped shape and polycrystalline film deposited on a single crystalline substrate of cubic symmetry with the same geometry.

7.8.1 *Isotropic rectangular parallelepiped sample*

The modification in the code given in paragraph 7.8.3 in order to be applicable for an elastically isotropic, polycrystalline, rectangular parallelepiped sample is given below. This part of the code should be replaced in the correct place in the given template code.

```

c
READ(3,* ,ERR=101) C11,C44,E1,E2,E3
READ(3,* ,ERR=101) (IA(I),I=1,5)
c
MA=5
A(1)=C11
A(2)=C44
A(3)=E1
A(4)=E2
A(5)=E3
c
827 FORMAT('Free moduli are c11, c44')
c
1205 FORMAT(' c11 c44 (%GPa)')
WRITE(*,1207)(A(I),I=1,2)
WRITE(3,1207)(A(I),I=1,2)
1207 FORMAT(2f7.4)
WRITE(*,'(1H )')
WRITE(3,'(1H )')
WRITE(*,1306)

```

```

WRITE(3,1306)
1306 FORMAT(' d1(cm) d2(cm) d3(cm)')
WRITE(*,1307)(A(I),I=3,5)
WRITE(3,1307)(A(I),I=3,5)
1307 FORMAT(3f9.5)
c
c
c Setup the elastic tensor according to symmetry
c
c C11, C22, C33
G(1,1,1,1)=A(1)
G(2,2,2,2)=A(1)
G(3,3,3,3)=A(1)
c C12, C23, C13
G(1,1,2,2)=A(1)-2*A(2)
G(2,2,1,1)=A(1)-2*A(2)
G(1,1,3,3)=A(1)-2*A(2)
G(3,3,1,1)=A(1)-2*A(2)
G(2,2,3,3)=A(1)-2*A(2)
G(3,3,2,2)=A(1)-2*A(2)
c C44
G(2,3,2,3)=A(2)
G(2,3,3,2)=A(2)
G(3,2,2,3)=A(2)
G(3,2,3,2)=A(2)
c C55
G(1,3,1,3)=A(2)
G(1,3,3,1)=A(2)
G(3,1,1,3)=A(2)
G(3,1,3,1)=A(2)
c C66
G(2,1,2,1)=A(2)
G(2,1,1,2)=A(2)
G(1,2,2,1)=A(2)
G(1,2,1,2)=A(2)
c
c Dimensions
c
E1=A(3)
E2=A(4)
E3=A(5)
NNP1=NN+1

```

```

NNP3=NN+3
c
DO 43 I=1,NMDS
WSAV(I)=1.D64
43 CONTINUE
c
c factors coming out of the derivation
c
E11=4.Do/(E1*E1)
E22=4.Do/(E2*E2)
E33=4.Do/(E3*E3)
E23=4.Do/(E2*E3)
E13=4.Do/(E1*E3)
E12=4.Do/(E1*E2)
c
c Loops for eight blocks
c
DO 8000 Lo=1,2
DO 8000 Mo=1,2
DO 8000 NO=1,2
c
IG=0
DO 2 I=1,3
LMN(1)=Lo
LMN(2)=Mo
LMN(3)=No
LMN(I)=LMN(I)+1
IF (LMN(I).EQ.3) LMN(I)=1
c
DO 2 L=LMN(1), NNP1,2
DO 2 M=LMN(2), NNP1,2
DO 2 N=LMN(3), NNP1,2
IF (L+M+N.GT.NNP3) GOTO 2
IG=IG+1
IC(IG)=I
LB(IG)=L-1
MB(IG)=M-1
NB(IG)=N-1
2 CONTINUE
NR=IG
c
c Calculate Gamma and E

```

```

c
DO 3 IG=1,NR
DO 3 JG=IG,NR
E(IG,JG)=o.Do
GAMMA(IG,JG)=o.Do
I=IC(IG)
J=IC(JG)
LS=LB(IG)+LB(JG)
MS=MB(IG)+MB(JG)
NS=NB(IG)+NB(JG)
GAMMA(IG,JG)=
& C(I,1,J,1)*DFLOAT(LB(IG)*LB(JG))*F(LS-2,MS,NS)*E11
& +C(I,2,J,2)*DFLOAT(MB(IG)*MB(JG))*F(LS,MS-2,NS)*E22
& +C(I,3,J,3)*DFLOAT(NB(IG)*NB(JG))*F(LS,MS,NS-2)*E33
& +(C(I,1,J,2)*DFLOAT(LB(IG)*MB(JG))+C(I,2,J,1)*
& DFLOAT(MB(IG)*LB(JG)))*F(LS-1,MS-1,NS)*E12
& +(C(I,1,J,3)*DFLOAT(LB(IG)*NB(JG))+C(I,3,J,1)*
& DFLOAT(NB(IG)*LB(JG)))*F(LS-1,MS,NS-1)*E13
& +(C(I,2,J,3)*DFLOAT(MB(IG)*NB(JG))+C(I,3,J,2)*
& DFLOAT(NB(IG)*MB(JG)))*F(LS,MS-1,NS-1)*E23
c
GAMMA(JG,IG)=GAMMA(IG,JG)
IF(I.EQ.J) E(IG,JG)=F(LS,MS,NS)
E(JG,IG)=E(IG,JG)
3 CONTINUE

```

c
function F stays the same because we did not change the shape of the sample

c

7.8.2 *Isotropic film on single crystalline rectangular parallelepiped substrate of cubic symmetry*

There are two main changes that one should apply in the code given in paragraph 7.8.3 in order to extract the elastic constants of a film deposited on a substrate. The first change is related to the description of the new shape of the sample, different thickness, by taking into account the deposited film. The second change is related to the modification in the potential energy of the system by taking into account the elastic constants of the substrate, C_{ijkl} , and of the film separately, C'_{ijkl} .

c

```

READ(3,*,ERR=101) C11,C12,C44,E1,E2,E3
READ(3,*,ERR=101) D11,D12,D44,E4
READ(3,*,ERR=101) ALPH0,BET0,GAM0
READ(3,*,ERR=101) (IA(I),I=1,13)
c
c
c Calculates the %density diff between film and substrate
c
DRHO=(RHOP-RHO)/RHO
c
c Here are the settings for substrate with film
c
MA=13
A(1)=D11
A(2)=D12
A(3)=D44
A(4)=E4
A(5)=C11
A(6)=C12
A(7)=C44
A(8)=E1
A(9)=E2
A(10)=E3
A(11)=ALPH
A(12)=BET
A(13)=GAM
c
827 FORMAT('Free moduli are c'11, c'12, c'44')
c
1204 FORMAT(' c11 c12 c44 (%GPa)')
WRITE(*,1207)(A(I),I=5,7)
WRITE(3,1207)(A(I),I=5,7)
WRITE(*,'(1H )')
WRITE(3,'(1H )')
WRITE(*,1205)
WRITE(3,1205)
1205 FORMAT(' c'11 c'12 c'44 (%GPa)')
WRITE(*,1207)(A(I),I=1,3)
WRITE(3,1207)(A(I),I=1,3)
1207 FORMAT(2f7.4)
WRITE(*,'(1H )')
WRITE(3,'(1H )')

```

```

WRITE(*,1305)
WRITE(3,1305)
1305 FORMAT(' d1(cm) d2(cm) d3(cm)')
WRITE(*,1307)(A(I),I=8,10)
WRITE(3,1307)(A(I),I=8,10)
WRITE(*,'(1H )')
WRITE(3,'(1H )')
WRITE(*,1306)
WRITE(3,1306)
1306 FORMAT(' film thick (cm)')
WRITE(*,1307)
WRITE(3,1307)
1307 FORMAT(3f9.5)
ALPHF=A(11)*360.0/TWOPI
BETF=A(12)*360.0/TWOPI
GAMF=A(13)*360.0/TWOPI
WRITE(*,'(1H )')
WRITE(3,'(1H )')
WRITE(*,1308)
WRITE(*,1309) ALPHF, BETF, GAMF
WRITE(3,1308)
WRITE(3,1309) ALPHF, BETF, GAMF
1308 FORMAT (' alpha(deg) beta(deg) gamma(deg)')
1309 FORMAT (3F11.1)
c
c Setup the elastic tensor according to symmetry
c
c C11, C22, C33
CG(1,1,1,1)=A(5)
CG(2,2,2,2)=A(5)
CG(3,3,3,3)=A(5)
c C12, C23, C13
CG(1,1,2,2)=A(6)
CG(2,2,1,1)=A(6)
CG(1,1,3,3)=A(6)
CG(3,3,1,1)=A(6)
CG(2,2,3,3)=A(6)
CG(3,3,2,2)=A(6)
c C44
CG(2,3,2,3)=A(7)
CG(2,3,3,2)=A(7)
CG(3,2,2,3)=A(7)

```

$$CG(3,2,3,2)=A(7)$$

c C55

$$CG(1,3,1,3)=A(7)$$

$$CG(1,3,3,1)=A(7)$$

$$CG(3,1,1,3)=A(7)$$

$$CG(3,1,3,1)=A(7)$$

c C66

$$CG(2,1,2,1)=A(7)$$

$$CG(2,1,1,2)=A(7)$$

$$CG(1,2,2,1)=A(7)$$

$$CG(1,2,1,2)=A(7)$$

c D11, D22, D33

$$DG(1,1,1,1)=A(1)$$

$$DG(2,2,2,2)=A(1)$$

$$DG(3,3,3,3)=A(1)$$

c D12, D23, D13

$$DG(1,1,2,2)=A(2)$$

$$DG(2,2,1,1)=A(2)$$

$$DG(1,1,3,3)=A(2)$$

$$DG(3,3,1,1)=A(2)$$

$$DG(2,2,3,3)=A(2)$$

$$DG(3,3,2,2)=A(2)$$

c D44

$$DG(2,3,2,3)=A(3)$$

$$DG(2,3,3,2)=A(3)$$

$$DG(3,2,2,3)=A(3)$$

$$DG(3,2,3,2)=A(3)$$

c D55

$$DG(1,3,1,3)=A(3)$$

$$DG(1,3,3,1)=A(3)$$

$$DG(3,1,1,3)=A(3)$$

$$DG(3,1,3,1)=A(3)$$

c D66

$$DG(2,1,2,1)=A(3)$$

$$DG(2,1,1,2)=A(3)$$

$$DG(1,2,2,1)=A(3)$$

$$DG(1,2,1,2)=A(3)$$

c

c Euler angles

c

$$ALPH=A(11)$$

$$BET=A(12)$$

```

GAM=A(13)
c
c Create the rotation according to Euler angles
c
ROT(1,1)=DCOS(GAM)*DCOS(BET)*DCOS(ALPH)-DSIN(GAM)*DSIN(ALPH)
ROT(1,2)=DCOS(GAM)*DCOS(BET)*DSIN(ALPH)+DSIN(GAM)*DCOS(ALPH)
ROT(1,3)=-DCOS(GAM)*DSIN(BET)
ROT(2,1)=-DSIN(GAM)*DCOS(BET)*DCOS(ALPH)-DCOS(GAM)*DSIN(ALPH)
ROT(2,2)=-DSIN(GAM)*DCOS(BET)*DSIN(ALPH)+DCOS(GAM)*DCOS(ALPH)
ROT(2,3)=DSIN(GAM)*DSIN(BET)
ROT(3,1)=DSIN(BET)*DCOS(ALPH)
ROT(3,2)=DSIN(BET)*DSIN(ALPH)
ROT(3,3)=DCOS(BET)
c
DO 110 I=1,3
DO 110 J=1,3
DO 110 K=1,3
DO 110 L=1,3
C(I,J,K,L)=0.Do
D(I,J,K,L)=0.Do
DO 100 IP=1,3
DO 100 IQ=1,3
DO 100 IR=1,3
DO 100 IS=1,3
c
c Create the rotated elastic moduli matrices
c
C(I,J,K,L)=C(I,J,K,L)+ROT(I,IP)*ROT(J,IQ)*ROT(K,IR)*ROT(L,IS)
&*CG(IP,IQ,IR,IS)
D(I,J,K,L)=D(I,J,K,L)+ROT(I,IP)*ROT(J,IQ)*ROT(K,IR)*ROT(L,IS)
&*DG(IP,IQ,IR,IS) 100 CONTINUE D(I,J,K,L)=D(I,J,K,L)-C(I,J,K,L)
110 CONTINUE
c
c Dimensions
c
E4=A(4)
E1=A(8)
E2=A(9)
E3=A(10)
c
NNP1=NN+1
NNP3=NN+3

```

```

c
c 2.Do is there due to normalisation
c
ALPHA=E4/(E3/2.Do)
c
DO 43 I=1,NMDS
WSAV(I)=1.D64
43 CONTINUE
c
c factors coming out of the derivation
c
E11=4.Do/(E1*E1)
E22=4.Do/(E2*E2)
E33=4.Do/(E3*E3)
E23=4.Do/(E2*E3)
E13=4.Do/(E1*E3)
E12=4.Do/(E1*E2)
c
IG=0
DO 2 I=1,3
DO 2 L=1,NNP1
DO 2 M=1,NNP1
DO 2 N=1,NNP1
IF(L+M+N.GT.NNP3) GO TO 2
IG=IG+1
IC(IG)=I
LB(IG)=L-1
MB(IG)=M-1
NB(IG)=N-1
2 CONTINUE
NR=IG
c
c Calculate Gamma
c
DO 3 IG=1,NR
DO 3 JG=IG,NR
E(IG,JG)=0.Do
GAMMA(IG,JG)=0.Do
I=IC(IG)
J=IC(JG)
LS=LB(IG)+LB(JG)
MS=MB(IG)+MB(JG)

```

```

NS=NB(IG)+NB(JG)
GAMMA(IG,JG)=
&C(I,1,J,1)*DFLOAT(LB(IG)*LB(JG))*F(LS-2,MS,NS)*E11
&+C(I,2,J,2)*DFLOAT(MB(IG)*MB(JG))*F(LS,MS-2,NS)*E22
&+C(I,3,J,3)*DFLOAT(NB(IG)*NB(JG))*F(LS,MS,NS-2)*E33
&+(C(I,1,J,2)*DFLOAT(LB(IG)*MB(JG))+C(I,2,J,1)*
&DFLOAT(MB(IG)*LB(JG)))*F(LS-1,MS-1,NS)*E12
&+(C(I,1,J,3)*DFLOAT(LB(IG)*NB(JG))+C(I,3,J,1)*
&DFLOAT(NB(IG)*LB(JG)))*F(LS-1,MS,NS-1)*E13
&+(C(I,2,J,3)*DFLOAT(MB(IG)*NB(JG))+C(I,3,J,2)*
&DFLOAT(NB(IG)*MB(JG)))*F(LS,MS-1,NS-1)*E23
&+D(I,1,J,1)*DFLOAT(LB(IG)*LB(JG))*G(LS-2,MS,NS)*E11
&+D(I,2,J,2)*DFLOAT(MB(IG)*MB(JG))*G(LS,MS-2,NS)*E22
&+D(I,3,J,3)*DFLOAT(NB(IG)*NB(JG))*G(LS,MS,NS-2)*E33
&+(D(I,1,J,2)*DFLOAT(LB(IG)*MB(JG))+D(I,2,J,1)*
&DFLOAT(MB(IG)*LB(JG)))*G(LS-1,MS-1,NS)*E12
&+(D(I,1,J,3)*DFLOAT(LB(IG)*NB(JG))+D(I,3,J,1)*
&DFLOAT(NB(IG)*LB(JG)))*G(LS-1,MS,NS-1)*E13
&+(D(I,2,J,3)*DFLOAT(MB(IG)*NB(JG))+D(I,3,J,2)*
&DFLOAT(NB(IG)*MB(JG)))*G(LS,MS-1,NS-1)*E23

```

```

c
GAMMA(JG,IG)=GAMMA(IG,JG)
IF(I.EQ.J) E(IG,JG)=F(LS,MS,NS)
&+DRHO*G(LS,MS,NS) E
(JG,IG)=E(IG,JG)
3 CONTINUE

```

c
function F stays the same because we did not change the shape of the substrate and we add function G for the film

```

c
c*****
c
FUNCTION G(IP,IQ,IR)
c*****
IMPLICIT INTEGER (I-N)
IMPLICIT REAL*8 (A-H,O-Z)
COMMON /ALPHA/ ALPHA
COMMON /RHOP/ RHOP
c
G=0.00D+00
IF((ALPHA.LE.0.0).OR.(RHOP.LE.0.0)) RETURN
IF((IP.LT.0).OR.(IQ.LT.0).OR.(IR.LT.0)) RETURN

```

```

IF((MOD(IP,2).NE.o).OR.(MOD(IQ,2).NE.o)) RETURN
c
IP1=IP+1
IQ1=IQ+1
IR1=IR+1
c
G=(4.Do/DFLOAT(IP1*IQ1*IR1))*(1.Do-(1.Do-ALPHA)**(IR1))
RETURN
END
c

```

7.8.3 *Single crystalline rectangular parallelepiped sample of cubic symmetry*

The algorithm below is written in fortran 77. It calculates the elastic constants of a single crystal with cubic symmetry having a rectangular parallelepiped geometry with the crystallographic axes rotated with respect to the sample axes. In order to be informative and practical to the non expert the algorithm contains a series of comments.

```

c*****
c
PROGRAM XYZMRQ
c
c*****
c
c Declaration of the variables
c
IMPLICIT INTEGER (I-N)
c
PARAMETER (MMAX=20,MDAT=60,TWOPI=6.283185307795864769)
c
INTEGER IA(MMAX)
REAL X(MDAT),Y(MDAT),A(MMAX),FDATA(MDAT)
REAL SIG(MDAT),ALPHA(MMAX,MMAX),COVAR(MMAX,MMAX)
c
REAL*8 RHO,WSAV(MDAT),WTMP(MDAT),DYDAA(MMAX,MDAT)
REAL*8 RAD,ALPH,BET,GAM,ALPHo,BETo,GAMo
REAL*8 DYDDAP, DOT1, DOT2, DOT3
CHARACTER HEADER*50, USED(MDAT)*3
EXTERNAL FREQS
c
c RHO=density, NN=Polynomial order, NMDS=# frequencies,

```

```

c NDATA=index of frequency, IA=refinement index
c
COMMON /RHO/ RHO
COMMON /NN/ NN
COMMON /NMDS/ NMDS
COMMON /NDATA/ NDATA
COMMON /IA/ IA
COMMON /X/ X
COMMON /WSAV/ WSAV,WTMP
COMMON /SIG/ SIG
COMMON /DYDAA/ DYDAA
c
c Format 400 means 50 characters
c
400 FORMAT(A50)
c
c TOL is the convergence limit
c
TOL=0.05
c
c Open the input file
c
OPEN(3,FILE='xyzmrq_rot.dat',STATUS='OLD',ERR=101)
GO TO 102
101 WRITE(*,'(A)') ' Error opening xyzmrq_rot.dat.'
GO TO 9900
c
c Read from the Elastic constants C.,the dimensions E., the Euler angles
c the density, polynomial order, # of freq
c
102 READ(3,400) HEADER
READ(3,*,ERR=101) C11,C12,C44,E1,E2,E3
READ(3,*,ERR=101) ALPH0,BET0,GAM0
READ(3,*,ERR=101) (IA(I),I=1,9)
READ(3,*,ERR=101) RHO,NN,NMDS
DO 103 I=1,NMDS
READ(3,*,ERR=101) FDATA(I)
103 CONTINUE
CLOSE(3,ERR=9900)
c
c Define the Euler angles in radians
c

```

```

RAD=TWOPI/360.
ALPH=ALPHo*RAD
BET=BETo*RAD
GAM=GAMo*RAD
c
c Store in X the index each frequency,
c Store in Y each frequency
c
FSUM=0.0
NDATA=0
DO 105 I=1,NMDS
IF(FDATA(I).LE.0.0) THEN
USED(I)='EXC'
GO TO 104
ELSE
IF(FDATA(I).GT.0.0) THEN
USED(I)='INC'
FSUM=FSUM+FDATA(I)
END IF
END IF
NDATA=NDATA+1
X(NDATA)=FLOAT(I)
Y(NDATA)=FDATA(I)
GO TO 105
104 IF(FDATA(I).EQ.0.0) USED(I)='- '
FDATA(I)=-FDATA(I)
105 CONTINUE
FAVG=FSUM/NDATA
c
c Parameter initialization through INIT subroutine
c
CALL INIT
c
c Parameter setup, MA # of parameters
c
MA=9
A(1)=C11
A(2)=C12
A(3)=C44
A(4)=E1
A(5)=E2
A(6)=E3

```

```

A(7)=ALPH
A(8)=BET
A(9)=GAM
c
c Give initial values
c
ALAMDA=-1.
SUMSQ=1.D23
ITER=0
c
c Create the output file, write in the header from the input,
c leave some blank lines
c
OPEN(3,FILE='mrqout.txt',STATUS='UNKNOWN')
WRITE(3,400) HEADER
c
c Count the iterations you have done and write them in the screen
c CALL CPU_TIME(tmo)
200 ITER=ITER+1
OLAMDA=ALAMDA
CHI0=SUMSQ
WRITE(*,'(1H)')
WRITE(*,'(A20,I2)') ' Iteration number',ITER
WRITE(*,'(1H)')
WRITE(3,'(1H)')
WRITE(3,'(A20,I2)') ' Iteration number',ITER
WRITE(3,'(1H)')
c
c Run the Levenberg-Marquardt minimization algorithm iteratively
c until you have the requested convergence
c
CALL MRQMIN(X,Y,SIG,NDATA,A,IA,MA,COVAR,ALPHA,MMAX,
&SUMSQ,FREQS,ALAMDA)
c
c Setup the outputs
c
WRITE(*,400) HEADER
WRITE(*,827)
WRITE(3,400) HEADER
WRITE(3,827)
827 FORMAT('Free moduli are c11, c12, c44')
WRITE(*,1107)

```

```

WRITE(3,1107)
1107 FORMAT(' # fexp ftheor %err wt df/dc11 df/dc12
&df/dc44')
c
CHANGE=ABS((SUMSQ-CHI0)/CHI0)
RMS=sqrt(SUMSQ/NDATA)
c
c You can interrupt the procedure at any step by including
c the lines: #162 + #247-#251 and exclude line #167
c IF(CHANGE.GT.TOL) GO TO 200
c
c Continue with setting up the outputs
c
SUMERR=0.0
DO 8200 I=1,NMDS
ERR=0.0
IF(FDATA(I).GT.0.) ERR=100.*((FDATA(I)-WSAV(I))/WSAV(I))
c
c Dydaa are the derivative output of the mrqmin subroutine,
c Dyddap is the sum of the derivatives for each freq
c Dot1-3 is the % contribution
c
DYDDAP=dabs((A(1)/WSAV(I))*DYDAA(1,I))
&+dabs((A(2)/WSAV(I))*DYDAA(2,I))
&+dabs((A(3)/WSAV(I))*DYDAA(3,I))
c
IF (DYDDAP .EQ. 0.0) THEN
DOT1=0
DOT2=0
DOT3=0
ELSE
DOT1=dabs((A(1)/WSAV(I))*DYDAA(1,I))/DYDDAP
DOT2=dabs((A(2)/WSAV(I))*DYDAA(2,I))/DYDDAP
DOT3=dabs((A(3)/WSAV(I))*DYDAA(3,I))/DYDDAP
ENDIF
c
WRITE(3,'(I3,2F10.6,F8.3,A6,3F8.2)') I,FDATA(I),WSAV(I),ERR,
&USED(I), DOT1,DOT2,DOT3
WRITE(*,'(I3,2F10.6,F8.3,A6,3F8.2)') I,FDATA(I),WSAV(I),ERR,
&USED(I), DOT1, DOT2, DOT3
IF (USED(I) .EQ. 'INC') SUMERR=SUMERR+ABS(ERR)
8200 CONTINUE

```

```

WRITE(*,'(A30,F8.3)') 'Avg error of included peaks= ',ERRAVG
WRITE(3,'(A30,F8.3)') 'Avg error of included peaks= ',ERRAVG
WRITE(*,'(1H)')
WRITE(3,'(1H)')
WRITE(*,1205) WRITE(3,1205)
1205 FORMAT(' c11 c12 c44 (%GPa)')
WRITE(*,1207)(A(I),I=1,3)
WRITE(3,1207)(A(I),I=1,3)
1207 FORMAT(3f7.4)
WRITE(*,'(1H)')
WRITE(3,'(1H)')
WRITE(*,1306)
WRITE(3,1306)
1306 FORMAT(' d1(cm) d2(cm) d3(cm)')
WRITE(*,1307)(A(I),I=4,6)
WRITE(3,1307)(A(I),I=4,6)
1307 FORMAT(3f9.5)
ALPHF=A(7)*360.0/TWOPI
BETF=A(8)*360.0/TWOPI
GAMF=A(9)*360.0/TWOPI
WRITE(*,'(1H)')
WRITE(3,'(1H)')
WRITE(*,1308)
WRITE(*,1309) ALPHF, BETF, GAMF
WRITE(3,1308)
WRITE(3,1309) ALPHF, BETF, GAMF
1308 FORMAT(' alpha(deg) beta(deg) gamma(deg)')
1309 FORMAT(3F11.1)
ERRAVG=SUMERR/NDATA
WRITE(*,'(1H)')
WRITE(3,'(1H)')
WRITE(*,'(A14,F8.5)') '% RMS Error= ',RMS/FAVG*100.
WRITE(3,'(A14,F8.5)') '% RMS Error= ',RMS/FAVG*100.
WRITE(*,'(A11,F8.5)') '% Change= ',CHANGE*100.
WRITE(3,'(A11,F8.5)') '% Change= ',CHANGE*100.
c
c Find and print only in screen the time between two iterations
c
CALL CPU_TIME(tm1)
WRITE(*,3900) (tm1-tm0)/60
3900 FORMAT(' Elapsed time(min) for this pass= ',f6.2)
CALL CPU_TIME(tm0)

```

```

IF (CHANGE.GT.0.0) Go TO 200
c 8210 WRITE(*,'(A)') Iterate again? (1=yes,0=no)
c READ(*,*) IB
c IF(IB.EQ.1) GO TO 200
c IF(IB.EQ.0) GO TO 9000
c GO TO 8210
c
9000 CLOSE(3, ERR=9900)
9900 STOP
END
c
c*****
c
SUBROUTINE FREQS(XVAL,A,YMOD,DYDA,MA)
c Supply a subroutine FUNCS(NF,X,A,YFIT,DYDA,MA) that evaluates the
c fitting function YFIT, and its derivatives DYDA with respect to
c the fitting parameters A at X. On the first call provide an initial
c guess for the parameters A, and set ALAMDA<0 for initialization
c (which then sets ALAMDA=0.001).
c*****
c
c Declaration of the variables
c
IMPLICIT INTEGER (I-N)
IMPLICIT REAL*8 (A-H,O-Z)
c
PARAMETER (MMAX=20,MDAT=60)
c
INTEGER IA(MMAX)
REAL XVAL,A(MA),YMOD,DYDA(MA),Ao,X(MDAT)
c
COMMON /ALST/ ALST(MMAX),EPS(MMAX)
COMMON /WSAV/ WSAV(MDAT),WTMP(MDAT)
COMMON /DYDAA/ DYDAA(MMAX,MDAT)
COMMON /NDATA/ NDATA
COMMON /X/ X COMMON /IA/ IA
c
c
c
10 DO 11 I=1,MA
IF(A(I).NE.ALST(I)) GO TO 100
11 CONTINUE GO TO 200

```

```

c
100 CALL XYZBLK(A,MA,WSAV)
c
DO 112 I=1,MA
IF(IA(I).EQ.0) GO TO 112
Ao=A(I)
A(I)=Ao*(1.Do+EPS(I))
DA=A(I)-Ao
CALL XYZBLK(A,MA,WTMP)
DO 111 J=1,NDATA
JX=NINT(X(J))
DYDAA(I,JX)=(WTMP(JX)-WSAV(JX))/DA
111 CONTINUE
A(I)=Ao
112 CONTINUE
c
DO 113 I=1,MA
ALST(I)=A(I)
113 CONTINUE
c
200 IX=NINT(XVAL)
YMOD=WSAV(IX)
DO 201 I=1,MA
DYDA(I)=DYDAA(I,IX)
201 CONTINUE
c
RETURN
END
c
c*****
c
SUBROUTINE XYZBLK(A,MA,WSAV)
c It is a subroutine in which one creates the tensor for the
c kinetic and potential energy
c*****
IMPLICIT INTEGER (I-N)
IMPLICIT REAL*8 (A-H,O-Z)
c
PARAMETER (MMAX=20,MDAT=60)
PARAMETER(NRR=2048,TWOPI=6.283185307795864769)
c
REAL A(MA)

```

```

c
DIMENSION LB(NRR),MB(NRR),NB(NRR),IC(NRR),LMN(3)
DIMENSION E(NRR,NRR),GAMMA(NRR,NRR),W(NRR),V(NRR,NRR),P(NRR)
DIMENSION D(NRR),WSAV(MDAT)
DIMENSION G(3,3,3,3), ROT(3,3)
c
COMMON /RHO/ RHO
COMMON /NN/ NN
COMMON /NMDS/ NMDS
COMMON /CIJKL/ C(3,3,3,3)
c
DO 12 I=1,3
DO 12 J=1,3
DO 12 K=1,3
DO 12 L=1,3
G(I,J,K,L)=0.Do
12 CONTINUE
c
c Setup the elastic tensor according to symmetry
c
c C11, C22, C33
G(1,1,1,1)=A(1)
G(2,2,2,2)=A(1)
G(3,3,3,3)=A(1)
c C12, C23, C13
G(1,1,2,2)=A(2)
G(2,2,1,1)=A(2)
G(1,1,3,3)=A(2)
G(3,3,1,1)=A(2)
G(2,2,3,3)=A(2)
G(3,3,2,2)=A(2)
c C44
G(2,3,2,3)=A(3)
G(2,3,3,2)=A(3)
G(3,2,2,3)=A(3)
G(3,2,3,2)=A(3)
c C55
G(1,3,1,3)=A(3)
G(1,3,3,1)=A(3)
G(3,1,1,3)=A(3)
G(3,1,3,1)=A(3)
c C66

```

```

G(2,1,2,1)=A(3)
G(2,1,1,2)=A(3)
G(1,2,2,1)=A(3)
G(1,2,1,2)=A(3)
c
c Euler angles
c
ALPH=A(7)
BET=A(8)
GAM=A(9)
c
c Create the rotation according to Euler angles
c
ROT(1,1)=DCOS(GAM)*DCOS(BET)*DCOS(ALPH)-DSIN(GAM)*DSIN(ALPH)

ROT(1,2)=DCOS(GAM)*DCOS(BET)*DSIN(ALPH)+DSIN(GAM)*DCOS(ALPH)

ROT(1,3)=-DCOS(GAM)*DSIN(BET)
ROT(2,1)=-DSIN(GAM)*DCOS(BET)*DCOS(ALPH)-DCOS(GAM)*DSIN(ALPH)

ROT(2,2)=-DSIN(GAM)*DCOS(BET)*DSIN(ALPH)+DCOS(GAM)*DCOS(ALPH)

ROT(2,3)=DSIN(GAM)*DSIN(BET)
ROT(3,1)=DSIN(BET)*DCOS(ALPH)
ROT(3,2)=DSIN(BET)*DSIN(ALPH)
ROT(3,3)=DCOS(BET)
c
DO 110 I=1,3
DO 110 J=1,3
DO 110 K=1,3
DO 110 L=1,3
C(I,J,K,L)=0.0
DO 100 IP=1,3
DO 100 IQ=1,3
DO 100 IR=1,3
DO 100 IS=1,3
c
c Create the rotated elastic moduli matrix
c
C(I,J,K,L)=C(I,J,K,L)+
&ROT(I,IP)*ROT(J,IQ)*ROT(K,IR)*ROT(L,IS)*G(IP,IQ,IR,IS)
100 CONTINUE

```

```

110 CONTINUE
c
c Dimensions
c
E1=A(4)
E2=A(5)
E3=A(6)
NNP1=NN+1
NNP3=NN+3
c
DO 43 I=1,NMDS
WSAV(I)=1.D64
43 CONTINUE
c
c factors coming out of the derivation
c
E11=4.Do/(E1*E1)
E22=4.Do/(E2*E2)
E33=4.Do/(E3*E3)
E23=4.Do/(E2*E3)
E13=4.Do/(E1*E3)
E12=4.Do/(E1*E2)
c
IG=0
DO 2 I=1,3
DO 2 L=1,NNP1
DO 2 M=1,NNP1
DO 2 N=1,NNP1
IF(L+M+N.GT.NNP3) GO TO 2
IG=IG+1 IC(IG)=I
LB(IG)=L-1
MB(IG)=M-1
NB(IG)=N-1
2 CONTINUE
NR=IG
c
c Calculate Gamma and E
c
DO 3 IG=1,NR
DO 3 JG=IG,NR
E(IG,JG)=0.Do
GAMMA(IG,JG)=0.Do

```

```

I=IC(IG)
J=IC(JG)
LS=LB(IG)+LB(JG)
MS=MB(IG)+MB(JG)
NS=NB(IG)+NB(JG)
GAMMA(IG,JG)=
& C(I,1,J,1)*DFLOAT(LB(IG)*LB(JG))*F(LS-2,MS,NS)*E11
& +C(I,2,J,2)*DFLOAT(MB(IG)*MB(JG))*F(LS,MS-2,NS)*E22
& +C(I,3,J,3)*DFLOAT(NB(IG)*NB(JG))*F(LS,MS,NS-2)*E33
& +(C(I,1,J,2)*DFLOAT(LB(IG)*MB(JG))+C(I,2,J,1)*
& DFLOAT(MB(IG)*LB(JG)))*F(LS-1,MS-1,NS)*E12
& +(C(I,1,J,3)*DFLOAT(LB(IG)*NB(JG))+C(I,3,J,1)*
& DFLOAT(NB(IG)*LB(JG)))*F(LS-1,MS,NS-1)*E13
& +(C(I,2,J,3)*DFLOAT(MB(IG)*NB(JG))+C(I,3,J,2)*
& DFLOAT(NB(IG)*MB(JG)))*F(LS,MS-1,NS-1)*E23
c
GAMMA(JG,IG)=GAMMA(IG,JG)
IF(I.EQ.J) E(IG,JG)=F(LS,MS,NS)
E(JG,IG)=E(IG,JG)
3 CONTINUE
c
CALL CHOLD(C,E,NR,NRR,P)
c
OOP=1.Do/P(1)
DO 21 I=1,NR
V(I,1)=GAMMA(I,1)*OOP
21 CONTINUE
DO 23 J=2,NR
OOP=1.Do/P(J)
DO 23 I=J,NR
SUM=GAMMA(I,J)
DO 22 K=1,J-1
SUM=SUM-V(I,K)*E(J,K)
22 CONTINUE
V(I,J)=SUM*OOP
23 CONTINUE
GAMMA(1,1)=V(1,1)/P(1)
DO 25 I=2,NR
SUM=V(I,1)
DO 24 K=1,I-1
SUM=SUM-E(I,K)*GAMMA(K,1)
24 CONTINUE

```

```

GAMMA(I,1)=SUM/P(I)
GAMMA(1,I)=GAMMA(I,1)
25 CONTINUE
DO 27 J=2,NR
DO 27 I=J,NR
SUM=V(I,J)
DO 26 K=1,I-1
SUM=SUM-E(I,K)*GAMMA(J,K)
26 CONTINUE
GAMMA(I,J)=SUM/P(I)
GAMMA(J,I)=GAMMA(I,J)
27 CONTINUE
c
CALL TRED2(GAMMA,NR,NRR,W,D)
c
CALL TQLI(W,D,NR,NRR,GAMMA)
c
c Save lowest frequencies.
c
60 DO 64 J=1,NR
W1=W(J)
IF(W1.LT.1.D-4) GO TO 64
DIFMAX=-1.Do
DO 61 I=1,NMDS
DIF=WSAV(I)-W1
IF(DIF.LE.DIFMAX) GO TO 61
DIFMAX=DIF IMAX=I
61 CONTINUE
IF(DIFMAX.LE.o.Do) GO TO 64
WSAV(IMAX)=W1
64 CONTINUE
c
c Sort frequencies.
c
DO 8012 I=1,NMDS-1
K=I
TMP=WSAV(I)
DO 8011 J=I+1,NMDS
IF(WSAV(J).GT.TMP) GO TO 8011
K=J TMP=WSAV(J)
8011 CONTINUE
IF(K.EQ.I) GO TO 8012

```

```

WSAV(K)=WSAV(I)
WSAV(I)=TMP
8012 CONTINUE
c
DO 8020 I=1,NMDS
WSAV(I)=DSQRT(WSAV(I)/RHO)/TWOPI
8020 CONTINUE
c
9000 RETURN
END
c
c*****
c
SUBROUTINE INIT
c It is a subroutine which initializes the variables but setting
c everything to zero or one or to the proper initial value
c*****
IMPLICIT INTEGER (I-N)
IMPLICIT REAL*8 (A-H,O-Z)
c
PARAMETER (MMAX=20,MDAT=60)
c
REAL SIG(MDAT)
c
COMMON /ALST/ ALST(MMAX),EPS(MMAX)
COMMON /CIJKL/ C(3,3,3)
COMMON /DYDAA/ DYDAA(MMAX,MDAT)
COMMON /SIG/ SIG
c
DO 11 I=1,MMAX
ALST(I)=0.Do
EPS(I)=1.D-5
11 CONTINUE
c
DO 12 I=1,3
DO 12 J=1,3
DO 12 K=1,3
DO 12 L=1,3
C(I,J,K,L)=0.Do
12 CONTINUE
c
DO 13 I=1,MMAX

```

```

DO 13 J=1,MDAT
DYDAA(I,J)=0.Do
13 CONTINUE
c
DO 14 I=1,MDAT
SIG(I)=1.Do
14 CONTINUE
c
RETURN
END
c
c*****
c
FUNCTION F(IP,IQ,IR)
c In this function the integral which gives the volume of your
c sample according to Visscher basis function is calculated.
c ATTENTION: The dimensions are normalised!!!
c*****
c
IMPLICIT INTEGER (I-N)
IMPLICIT REAL*8 (A-H,O-Z)
c
c Set the initial value of the integral to zero
c
F=0.00D+00
IF((IP.LT.0).OR.(IQ.LT.0).OR.(IR.LT.0))
RETURN
IF((MOD(IP,2).NE.0).OR.(MOD(IQ,2).NE.0).OR.(MOD(IR,2).NE.0))
& RETURN
c
IP1=IP+1
IQ1=IQ+1
IR1=IR+1
c
F=8.Do/DFLOAT(IP1*IQ1*IR1)
RETURN
END
c
c From now on all subroutine are taken without any change from libraries
c*****
c
SUBROUTINE CHOLDC(A,N,NP,P)

```

```
SUBROUTINE TRED2(A,N,NP,D,E)
SUBROUTINE TQLI(D,E,N,NP,Z)
FUNCTION DPYTHAG(A,B)
SUBROUTINE mrqmin(x,y,sig,ndata,a,ia,ma,covar,alpha,nca,chisq, *funcs,alamda)
SUBROUTINE mrqcof(x,y,sig,ndata,a,ia,ma,alpha,beta,nalp,chisq, *funcs)
SUBROUTINE gaussj(a,n,np,b,m,mp)
SUBROUTINE covsrt(covar,npc,ma,ia,mfit)
```

BIBLIOGRAPHY

- [1] Plato, *Republic* (850bc). (Cited on page [xv](#).)
- [2] C. G. Levi, *Curr. Opin. Solid State Mater. Sci.* **8**, 77 (2004). (Cited on page [1](#).)
- [3] N. S. Lewis and D. G. Nocera, *Proc. Natl. Acad. Sci. U.S.A.* **103**, 15729 (2006). (Cited on page [1](#).)
- [4] C. Kittel, *Introduction to Solid State Physics* (John Wiley and Sons, 2004). (Cited on page [1](#).)
- [5] M. Christensen, S. Johnsen, and B. B. Iversen, *Dalton Trans.* **39**, 978 (2010). (Cited on pages [1](#) and [84](#).)
- [6] J. Callaway, *Phys. Rev.* **113**, 1046 (1959). (Cited on page [2](#).)
- [7] A. Möchel, I. Sergueev, N. Nguyen, G. J. Long, F. Grandjean, D. C. Johnson, and R. P. Hermann, *Phys. Rev. B* **84**, 064302 (2011). (Cited on page [2](#).)
- [8] A. Balandin and K. L. Wang, *Phys. Rev. B* **58**, 1544 (1998). (Cited on page [2](#).)
- [9] D. C. Wallace, *Thermodynamics of Crystals* (Dover Publications, 1998). (Cited on pages [3](#) and [4](#).)
- [10] N. W. Ashcroft and N. D. Mermin, *Solid State Physics* (Brooks / Cole, 1976). (Cited on pages [4](#), [6](#), [36](#), [41](#), and [81](#).)
- [11] H. Ledbetter, A. Lawson, and A. Migliori, *J. Phys. Condens. Matter* **22**, 165401 (2010). (Cited on page [4](#).)
- [12] A. F. Ioffe, *Semiconductor Thermoelements and Thermoelectric Cooling* (Infosearch, 1957). (Cited on page [4](#).)
- [13] URL <http://www.theenergyreport.com/>. (Cited on page [5](#).)
- [14] J. G. Snyder and E. S. Toberer, *Nat. Mater.* **7**, 105 (2008). (Cited on page [5](#).)
- [15] B. Forbes, A. D’Alfonso, S. Findlay, D. V. Dyck, J. LeBeau, S. Stemmer, and L. Allen, *Ultramicroscopy* **111**, 1670 (2011). (Cited on page [5](#).)

- [16] M. W. Cole and D. R. Frankl, *Surf. Sci.* **70**, 585 (1978). (Cited on page 5.)
- [17] K. J. Gaffney and H. N. Chapman, *Science* **316**, 1444 (2007). (Cited on page 5.)
- [18] G. E. Bacon and K. Lonsdale, *Rep. Prog. Phys.* **16**, 1 (1953). (Cited on page 5.)
- [19] W. F. Kuhs, *Acta Crystallogr., Sect. A: Found. Crystallogr.* **48**, 80 (1992). (Cited on pages 6, 20, and 73.)
- [20] R. Stedman, L. Almqvist, and G. Nilsson, *Phys. Rev.* **162**, 549 (1967). (Cited on page 6.)
- [21] R. Wielinga, J. Lubbers, and W. Huiskamp, *Physica* **37**, 375 (1967). (Cited on page 6.)
- [22] R. Felten, F. Steglich, G. Weber, H. Rietschel, F. Gompf, B. Renker, and J. Beuers, *Europhys. Lett.* **2**, 323 (1986). (Cited on pages 6 and 36.)
- [23] V. K. Pecharsky and J. K. A. Gschneidner, *J. Appl. Phys.* **86**, 6315 (1999). (Cited on page 6.)
- [24] J. A. Souza, Y.-K. Yu, J. J. Neumeier, H. Terashita, and R. F. Jardim, *Phys. Rev. Lett.* **94**, 207209 (2005). (Cited on page 6.)
- [25] LOT-Oriel, *Advanced heat capacity with helium-3 for PPMS* (Quantum Design, 2012), application note. (Cited on page 7.)
- [26] J. S. Hwang, K. J. Lin, and C. Tien, *Review of Scientific Instruments* **68**, 94 (1997). (Cited on page 7.)
- [27] Q. Design, *Non-smooth specific heat between 200 K and 300 K due to anomalous specific heat of Apiezon N-grease* (Quantum Design, 2002), heat Capacity application note 1085-152. (Cited on pages 8 and 71.)
- [28] A. Kalinichev, J. Bass, B. Sun, and D. Payne, *J. Mater. Res.* **12**, 2623 (1997). (Cited on page 8.)
- [29] S. Klotz, T. Strässle, A. Cornelius, J. Philippe, and V. Pomjakushin, *J. Phys. D: Appl. Phys.* **44**, 055406 (2011). (Cited on page 8.)
- [30] A. Bosak, M. Krisch, M. Mohr, J. Maultzsch, and C. Thomsen, *Phys. Rev. B* **75**, 153408 (2007). (Cited on page 8.)
- [31] H. Koizumi, M. Tachibana, and K. Kojima, *Phys. Rev. E* **79**, 061917 (2009). (Cited on page 8.)

- [32] L. L. Stevens, D. E. Hooks, and A. Migliori, *J. Appl. Phys.* **108**, 053512 (2010). (Cited on page 8.)
- [33] J. Rayleigh, *The theory of sound* (MacMillan, 1894). (Cited on page 10.)
- [34] J. Plešek, R. Kolman, and M. Landa, *J. Acoust. Soc. Am.* **116**, 282 (2004). (Cited on page 10.)
- [35] W. M. Visscher, A. Migliori, T. M. Bell, and R. A. Reinert, *J. Acoust. Soc. Am.* **90**, 2154 (1991). (Cited on page 10.)
- [36] L. Landau, *Theory of elasticity* (Elsevier, 1986). (Cited on page 11.)
- [37] R. Hill, *Proc. Phys. Soc. London, Sect. A* **65**, 349 (1952). (Cited on pages 11, 40, 41, and 64.)
- [38] V. Petricek et al., *Jana 2006. The crystallographic computing system.* (2006). (Cited on pages 14 and 73.)
- [39] B. H. Toby, *J. Appl. Cryst.* **34**, 210 (2001). (Cited on page 14.)
- [40] J. Rodríguez-Carvajal, *Physica B* **192**, 55 (1993). (Cited on pages 14, 27, 29, 58, and 68.)
- [41] W. Kuhn, *Phil. Mag* **8**, 625 (1929). (Cited on page 14.)
- [42] V. Potapkin, A. I. Chumakov, G. V. Smirnov, J.-P. Celse, R. Rüffer, C. McCammon, and L. Dubrovinsky, *J. Synchrotron Radiat.* **19**, 559 (2012). (Cited on page 14.)
- [43] A. Chumakov and R. Rüffer, *Hyperfine Interact.* **113**, 59 (1998). (Cited on pages 14 and 26.)
- [44] URL <http://www.nucleide.org/>. (Cited on page 15.)
- [45] I. Sergueev, H.-C. Wille, R. P. Hermann, D. Bessas, Y. V. Shvyd'ko, M. Zajac, and R. Rüffer, *J. Synchrotron Radiat.* **18**, 802 (2011). (Cited on pages 15, 16, 17, 28, 46, 48, 55, and 60.)
- [46] D. Ishikawa, A. Q. R. Baron, and T. Ishikawa, *Phys. Rev. B* **72**, 140301 (2005). (Cited on pages 15 and 87.)
- [47] Y. Shvyd'ko, *X-Ray Optics* (Springer, 2004). (Cited on page 16.)
- [48] T. S. Toellner, A. Alatas, and A. H. Said, *J. Synchrotron Radiat.* **18**, 605 (2011). (Cited on page 16.)

- [49] K. S. Singwi and A. Sjölander, *Phys. Rev.* **120**, 1093 (1960). (Cited on page 16.)
- [50] H. J. Lipkin, *Phys. Rev. B* **52**, 10073 (1995). (Cited on pages 16, 30, 48, and 60.)
- [51] V. Kohn and A. Chumakov, *Hyperfine Interact.* **125**, 205 (2000). (Cited on pages 16, 30, 48, 60, and 74.)
- [52] A. I. Chumakov, R. Rüffer, A. Q. R. Baron, H. Grünsteudel, H. F. Grünsteudel, and V. G. Kohn, *Phys. Rev. B* **56**, 10758 (1997). (Cited on pages 17, 50, and 64.)
- [53] N. Han, S. I. Kim, J.-D. Yang, K. Lee, H. Sohn, H.-M. So, C. W. Ahn, and K.-H. Yoo, *Adv. Mater.* **23**, 1871 (2011). (Cited on pages 18, 25, and 54.)
- [54] J. Liu, S. Liu, and J. Wei, *Appl. Phys. Lett.* **97**, 261903 (2010). (Cited on pages 18, 25, and 54.)
- [55] B. Poudel, Q. Hao, Y. Ma, Y. Lan, A. Minnich, B. Yu, X. Yan, D. Wang, A. Muto, D. Vashaee, et al., *Science* **320**, 634 (2008). (Cited on pages 18, 53, and 62.)
- [56] J. Drabble and C. Goodman, *J. Phys. Chem. Solids* **5**, 142 (1958). (Cited on pages 18 and 26.)
- [57] J.-P. Gaspard and R. Ceolin, *Solid State Commun.* **84**, 839 (1992). (Cited on page 18.)
- [58] J. O. Jenkins, J. A. Rayne, and R. W. Ure, *Phys. Rev. B* **5**, 3171 (1972). (Cited on pages 19, 28, 29, 38, 40, 41, and 42.)
- [59] L. D. Hicks and M. S. Dresselhaus, *Phys. Rev. B* **47**, 12727 (1993). (Cited on pages 19 and 53.)
- [60] L. D. Hicks and M. S. Dresselhaus, *Phys. Rev. B* **47**, 12727 (1993). (Cited on pages 19 and 53.)
- [61] J. E. Cornett and O. Rabin, *Appl. Phys. Lett.* **98**, 182104 (2011). (Cited on pages 19 and 54.)
- [62] N. Peranio, E. Leister, W. Töllner, O. Eibl, and K. Nielsch, *Adv. Funct. Mater.* **22**, 151 (2012). (Cited on page 19.)
- [63] N. Fukata, T. Oshima, K. Murakami, T. Kizuka, T. Tsurui, and S. Ito, *Appl. Phys. Lett.* **86**, 213112 (2005). (Cited on page 20.)

- [64] S. Piscanec, M. Cantoro, A. C. Ferrari, J. A. Zapien, Y. Lifshitz, S. T. Lee, S. Hofmann, and J. Robertson, *Phys. Rev. B* **68**, 241312 (2003). (Cited on page 20.)
- [65] X. Wang, A. Shakouri, B. Yu, X. Sun, and M. Meyyappan, *J. Appl. Phys.* **102**, 014304 (2007). (Cited on pages 20 and 63.)
- [66] R. P. Hermann, V. Keppens, P. Bonville, G. S. Nolas, F. Grandjean, G. J. Long, H. M. Christen, B. C. Chakoumakos, B. C. Sales, and D. Mandrus, *Phys. Rev. Lett.* **97**, 017401 (2006). (Cited on page 20.)
- [67] M. Christensen, A. B. Abrahamsen, N. B. Christensen, F. Juranyi, N. H. Andersen, K. Lefmann, J. Andreasson, C. R. H. Bahl, and B. B. Iversen, *Nat. Mater.* **7**, 811 (2008). (Cited on page 20.)
- [68] A. Migliori and J. Sarrao, *Resonant Ultrasound Spectroscopy* (John Willey and Sons, 1997). (Cited on pages 21, 41, and 100.)
- [69] R. I. Cottam and G. A. Saunders, *J. Phys. C: Solid State Phys.* **6**, 2105 (1973). (Cited on pages 21 and 101.)
- [70] R. J. Mehta, Y. Zhang, C. Karthik, B. Singh, R. W. Siegel, T. Borca-Tasciuc, and G. Ramanath, *Nat. Mater.* **11**, 233 (2012). (Cited on page 25.)
- [71] M. H. Lankhorst, B. W. Ketelaars, and R. A. Wolters, *Nat. Mater.* **4**, 347 (2005). (Cited on pages 25 and 54.)
- [72] H. Zhang, C.-X. Liu, X.-L. Qi, X. Dai, Z. Fang, and S.-C. Zhang, *Nat. Phys.* **5**, 438 (2009). (Cited on page 25.)
- [73] B.-T. Wang and P. Zhang, *Appl. Phys. Lett.* **100**, 082109 (2012). (Cited on page 25.)
- [74] Y. Xia, D. Qian, D. Hsieh, L. Wray, A. Pal, H. Lin, A. Bansil, D. Grauer, Y. Hor, R. J. Cava, et al., *Nat. Phys.* **5**, 398 (2009). (Cited on page 25.)
- [75] Y. L. Chen, J. G. Analytis, J.-H. Chu, Z. K. Liu, S.-K. Mo, X. L. Qi, H. J. Zhang, D. H. Lu, X. Dai, Z. Fang, et al., *Science* **325**, 178 (2009). (Cited on page 25.)
- [76] R. Vilaplana, O. Gomis, F. J. Manjón, A. Segura, E. Pérez-González, et al., *Phys. Rev. B* **84**, 104112 (2011). (Cited on page 26.)
- [77] R. T. Delves, A. E. Bowley, D. W. Hazelden, and H. J. Goldsmid, *Proc. Phys. Soc. London* **78**, 838 (1961). (Cited on page 26.)

- [78] P. Fornasini, *J. Phys. Condens. Matter* **13**, 7859 (2001). (Cited on page 26.)
- [79] A. S. Pine and G. Dresselhaus, *Phys. Rev. B* **4**, 356 (1971). (Cited on page 26.)
- [80] M. Christensen, F. Juranyi, and B. B. Iversen, *Physica B* **385-386**, 505 (2006). (Cited on page 26.)
- [81] E. Burkel, *Rep. Prog. Phys.* **63**, 171 (2000). (Cited on pages 26 and 78.)
- [82] A. Hashibon and C. Elsässer, *Phys. Rev. B* **84**, 144117 (2011). (Cited on pages 26 and 39.)
- [83] H.-C. Wille, Y. V. Shvyd'ko, E. E. Alp, H. D. Rüter, O. Leupold, I. Sergueev, R. Ruffer, A. Barla, and J. P. Sanchez, *Europhys. Lett.* **74**, 170 (2006). (Cited on pages 26 and 30.)
- [84] H.-C. Wille, R. P. Hermann, I. Sergueev, U. Pelzer, A. Möchel, T. Claudio, J. Perßon, R. Ruffer, A. Said, and Y. V. Shvyd'ko, *Europhys. Lett.* **91** (2010). (Cited on pages 26, 30, 46, 54, and 55.)
- [85] H. Rauh, R. Geick, H. Kohler, N. Nucker, and N. Lehner, *J. Phys. C: Solid State Phys.* **14**, 2705 (1981). (Cited on pages 26, 30, 33, 34, 38, and 43.)
- [86] T. L. Anderson and H. Krause, *Acta Crystallogr., Sect. B: Struct. Sci* **30**, 1307 (1974). (Cited on pages 28, 29, and 49.)
- [87] R. Ruffer and A. Chumakov, *Hyperfine Interact.* **97-98**, 589 (1996). (Cited on pages 28, 47, and 74.)
- [88] A. I. Chumakov, A. Barla, R. Ruffer, J. Metge, H. F. Grünsteudel, H. Grünsteudel, J. Plessel, H. Winkelmann, and M. M. Abd-Elmeguid, *Phys. Rev. B* **58**, 254 (1998). (Cited on page 28.)
- [89] C. J. Howard and E. H. Kisi, *J. Appl. Cryst.* **33**, 1434 (2000). (Cited on pages 29 and 58.)
- [90] M. Y. Hu, H. Sinn, A. Alatas, W. Sturhahn, E. E. Alp, H. C. Wille, Y. V. Shvyd'ko, J. P. Sutter, J. Bandaru, E. E. Haller, et al., *Phys. Rev. B* **67**, 113306 (2003). (Cited on pages 29 and 36.)
- [91] J. Barnes, J. Rayne, and R. U. Jr, *Phys. Lett. A* **46**, 317 (1974). (Cited on page 29.)

- [92] X. Chen, H. D. Zhou, A. Kiswandhi, I. Miotkowski, Y. P. Chen, P. A. Sharma, A. L. L. Sharma, M. A. Hekmaty, D. Smirnov, and Z. Jiang, *Appl. Phys. Lett.* **99**, 261912 (2011). (Cited on page 29.)
- [93] G. C. Sosso, S. Caravati, and M. Bernasconi, *J. Phys. Condens. Matter* **21**, 095410 (2009). (Cited on pages 30, 33, 38, and 50.)
- [94] W. Richter and C. R. Becker, *Phys. Status Solidi B* **84**, 619 (1977). (Cited on page 30.)
- [95] V. G. Kohn, A. I. Chumakov, and R. Rüffer, *Phys. Rev. B* **58**, 8437 (1998). (Cited on page 32.)
- [96] R. Rüffer and A. Chumakov, *Hyperfine Interact.* **128**, 255 (2000). (Cited on page 32.)
- [97] E. S. R. Gopal, *Specific Heats at Low Temperatures* (Heynwood Books, 1966). (Cited on pages 36, 42, and 78.)
- [98] W. A. Phillips, *J. Low Temp. Phys.* **7**, 351 (1972). (Cited on page 36.)
- [99] J. W. Gardner and A. C. Anderson, *Phys. Rev. B* **23**, 474 (1981). (Cited on page 36.)
- [100] R. Movshovich, A. Yatskar, M. F. Hundley, P. C. Canfield, and W. P. Beyermann, *Phys. Rev. B* **59**, R6601 (1999). (Cited on page 36.)
- [101] H. R. Schober and W. Petry, *Lattice Vibrations* (Wiley-VCH Verlag GmbH, 2006), ISBN 9783527603978. (Cited on page 38.)
- [102] T. Matsunaga et al., *Adv. Funct. Mater.* **21**, 2232 (2011). (Cited on pages 38, 54, and 83.)
- [103] D. Lencer, M. Salinga, B. Grabowski, T. Hickel, J. Neugebauer, and M. Wuttig, *Nat. Mater.* **7**, 971 (2008). (Cited on pages 38 and 45.)
- [104] U. Heinzmann and J. H. Dil, *J. Phys. Condens. Matter* **24**, 173001 (2012). (Cited on page 39.)
- [105] G. E. Shoemaker, J. A. Rayne, and R. W. Ure, *Phys. Rev.* **185**, 1046 (1969). (Cited on page 39.)
- [106] N. Peranio, M. Winkler, Z. Aabdin, J. König, H. Böttner, and O. Eibl, *Phys. Status Solidi A* **521**, 163 (2012). (Cited on page 39.)
- [107] M. Saint-Paul, J. C. Lasjaunias, and M. Locatelli, *J. Phys. C: Solid State Phys.* **15**, 2375 (1982). (Cited on page 41.)

- [108] Y. Wang, *J. Phys. Chem. Solids* **47**, 181 (1986). (Cited on page 41.)
- [109] A. Pashinkin, A. Malkova, and M. Mikhailova, *Russ. J. Phys. Chem. A* **82**, 1035 (2008). (Cited on page 41.)
- [110] B. Y. Yavorsky, N. F. Hinsche, I. Mertig, and P. Zahn, *Phys. Rev. B* **84**, 165208 (2011). (Cited on page 41.)
- [111] N. Sakai, T. Kajiwara, K. Takemura, S. Minomura, and Y. Fujii, *Solid State Commun.* **40**, 1045 (1981). (Cited on pages 41 and 42.)
- [112] D. Hsieh, Y. Xia, D. Qian, L. Wray, J. H. Dil, F. Meier, J. Osterwalder, L. Patthey, J. G. Checkelsky, N. P. Ong, et al., *Nature* **460**, 1101 (2009). (Cited on page 41.)
- [113] R. P. Hermann, F. Grandjean, and G. J. Long, *Am. J. Phys* **73**, 110 (2005). (Cited on page 41.)
- [114] T. Barron, J. Collins, and G. White, *Adv. Phys.* **29**, 609 (1980). (Cited on page 42.)
- [115] G. K. White, *J. Phys. C: Solid State Phys.* **5**, 2731 (1972). (Cited on page 42.)
- [116] E. S. Toberer, A. Zevalkink, and G. J. Snyder, *J. Mater. Chem.* **21**, 15843 (2011). (Cited on pages 43 and 64.)
- [117] D. Spitzer, *J. Phys. Chem. Solids* **31**, 19 (1970). (Cited on pages 43, 44, 52, and 65.)
- [118] O. Anderson, *J. Phys. Chem. Solids* **12**, 41 (1959). (Cited on page 43.)
- [119] G. A. Slack, *Solid State Physics* (Academic Press, 1979). (Cited on pages 43 and 52.)
- [120] A. Jacquot, N. Farag, M. Jaegle, M. Bobeth, J. Schmidt, D. Ebling, and H. Böttner, *J. Electron. Mater.* **39**, 1861 (2010). (Cited on page 44.)
- [121] E. Makovicky, *Rev. Mineral. Geochem.* **61**, 7 (2006). (Cited on page 45.)
- [122] P. Schmid, in *Festkörperprobleme 16* (1976), vol. 16 of *Advances in Solid State Physics*, pp. 47–64, ISBN 978-3-528-08022-8. (Cited on page 45.)
- [123] H. Zabel, *J. Phys. Condens. Matter* **13**, 7679 (2001). (Cited on page 45.)
- [124] R. Zallen and M. Slade, *Phys. Rev. B* **9**, 1627 (1974). (Cited on pages 45 and 50.)

- [125] X. A. Fan, J. Y. Yang, Z. Xie, K. Li, W. Zhu, X. K. Duan, C. J. Xiao, and Q. Q. Zhang, *J. Phys. D.: Appl. Phys.* **40**, 5975 (2007). (Cited on page 45.)
- [126] S. Li, H. M. A. Soliman, J. Zhou, M. S. Toprak, M. Muhammed, D. Platzek, P. Ziolkowski, and E. Müller, *Chem. Mater.* **20**, 4403 (2008). (Cited on page 46.)
- [127] F. R. Harris, S. Standridge, C. Feik, and D. Johnson, *Angew. Chem. Int. Engl* **42**, 5295 (2003). (Cited on page 46.)
- [128] Y. Kim, A. Di Venere, G. K. L. Wong, J. B. Ketterson, S. Cho, and J. R. Meyer, *J. Appl. Phys.* **91**, 715 (2002). (Cited on page 46.)
- [129] D. C. Johnson, *Curr. Opin. Solid. St. M.* **3**, 159 (1998). (Cited on page 46.)
- [130] M. Winkler, X. Liu, J. D. Konig, S. Buller, U. Schurmann, L. Kienle, W. Bensch, and H. Böttner, *J. Mater. Chem.* **22**, 11323 (2012). (Cited on pages 46 and 52.)
- [131] J. Nurnus, *PhD thesis* (Fakültat für Physik der Albert-Ludwigs-Universität Freiburg i. Br., Germany, 2001). (Cited on page 46.)
- [132] C. Christescu, D. G. Cahill, C. Heideman, Q. Lin, C. Mortensen, D. Johnson, R. Rostek, and H. Böttner, *J. Appl. Phys.* **104**, 033533 (2008). (Cited on page 46.)
- [133] D. G. Cahill, *Rev. Sci. Instr.* **75**, 5119 (2004). (Cited on page 46.)
- [134] A. P. Hammersley, S. O. Svensson, M. Hanfland, A. N. Fitch, and D. Hausermann, *High Pressure Res.* **14**, 235 (1996). (Cited on page 46.)
- [135] A. I. Chumakov, R. Rüffer, O. Leupold, and I. Sergueev, *Struct. Chem.* **14**, 109 (2003). (Cited on pages 47, 62, and 64.)
- [136] D. Bessas, I. Sergueev, H.-C. Wille, J. Persson, D. Ebling, and R. Hermann, *Phys. Rev. B* (2012), submitted July 2012. (Cited on pages 48, 52, 60, 64, and 65.)
- [137] P. Boolchand, W. Bresser, M. Zhang, Y. Wu, J. Wells, and R.ENZWEILER, *J. Non-Cryst. Solids* **182**, 143 (1995). (Cited on page 49.)
- [138] M. H. Francombe, *Philos. Mag.* **10**, 989 (1964). (Cited on page 50.)
- [139] J. D. Bass, *Elasticity of minerals, glasses and melts, in mineral physics and crystallography* (American Geophysical Union, 1995). (Cited on page 50.)

- [140] G. C. Schatz, Proc. Natl. Acad. Sci. U.S.A. **104**, 6885 (2007). (Cited on page 53.)
- [141] A. A. Balandin, Nat. Mater. **10**, 569 (2011). (Cited on page 53.)
- [142] V. Swamy, E. Holbig, L. S. Dubrovinsky, V. Prakapenka, and B. C. Muddle, J. Phys. Chem. Solids **69**, 2332 (2008). (Cited on page 53.)
- [143] A. K. Geim and K. S. Novoselov, Nat. Mater. **6**, 183 (2007). (Cited on page 53.)
- [144] J. H. Lee et al., Nature **466**, 954 (2010). (Cited on pages 53, 56, and 67.)
- [145] T. Gao and T. Wang, Cryst. Growth Des. **10**, 4995 (2010). (Cited on page 53.)
- [146] P. S. Kireev, *Semiconductor Physics* (Mir Publishers, 1978). (Cited on page 53.)
- [147] M. Kashiwagi, S. Hirata, K. Harada, Y. Zheng, K. Miyazaki, M. Yahiro, and C. Adachi, Appl. Phys. Lett. **98**, 023114 (2011). (Cited on page 54.)
- [148] S. H. Lee, W. Shim, S. Y. Jang, J. W. Roh, P. Kim, J. Park, and W. Lee, Nanotechnology **22**, 295707 (2011). (Cited on page 54.)
- [149] A. I. Chumakov, A. Q. R. Baron, R. Ruffer, H. Grünsteudel, H. F. Grünsteudel, and A. Meyer, Phys. Rev. Lett. **76**, 4258 (1996). (Cited on page 54.)
- [150] K. Nielsch, J. Choi, K. Schwirn, R. B. Wehrspohn, and U. Gösele, Nano Lett. **2**, 677 (2002). (Cited on page 54.)
- [151] L. Trahey, C. R. Becker, and A. M. Stacy, Nano Lett. **7**, 2535 (2007). (Cited on page 54.)
- [152] N. Peranio, E. Lester, W. Töllner, O. Eibl, and N. K., Adv. Funct. Mater. **22**, 151 (2012). (Cited on page 55.)
- [153] G. Cliff and G. W. Lorimer, J. Microsc. **103**, 203 (1975). (Cited on page 55.)
- [154] N. Peranio and O. Eibl, Phys. Status Solidi A **204**, 3243 (2007). (Cited on pages 55 and 56.)
- [155] R. Ruffer and A. Chumakov, Hyperfine Interact. **97-98**, 589 (1996). (Cited on page 56.)

- [156] Seizo and Nakajima, *J. Phys. Chem. Solids* **24**, 479 (1963). (Cited on page 58.)
- [157] T. B. Massalski, *Binary Alloys Phase Diagrams* (American Society for Metals, 1990). (Cited on page 62.)
- [158] H. Lind, S. Lidin, and U. Häussermann, *Phys. Rev. B* **72**, 184101 (2005). (Cited on page 62.)
- [159] H. Lind and S. Lidin, *Solid State Sci.* **5**, 47 (2003). (Cited on page 62.)
- [160] D. L. Medlin, Q. M. Ramasse, C. D. Spataru, and N. Y. C. Yang, *J. Appl. Phys.* **108**, 043517 (2010). (Cited on page 62.)
- [161] C.-N. Liao, H.-D. Shih, and P.-W. Su, *J. Electrochem. Soc.* **157**, D605 (2010). (Cited on page 62.)
- [162] L. Fuentes-Montero, M. E. Montero-Cabrera, and L. Fuentes-Cobas, *J. Appl. Crystallogr.* **44**, 241 (2011). (Cited on page 63.)
- [163] C. Weber, A. Fuhrer, C. Fasth, G. Lindwall, L. Samuelson, and A. Wacker, *Phys. Rev. Lett.* **104**, 036801 (2010). (Cited on page 63.)
- [164] P. N. Martin, Z. Aksamija, E. Pop, and U. Ravaioli, *Nano Lett.* **10**, 1120 (2010). (Cited on page 63.)
- [165] I. Campbell and P. Fauchet, *Solid State Commun.* **58**, 739 (1986). (Cited on page 63.)
- [166] D. Abdula, K. T. Nguyen, K. Kang, S. Fong, T. Ozel, D. G. Cahill, and M. Shim, *Phys. Rev. B* **83**, 205419 (2011). (Cited on page 64.)
- [167] S. Davis and G. Gutiérrez, *J. Phys. Condens. Matter* **23**, 495401 (2011). (Cited on page 64.)
- [168] D.-A. Borca-Tasciuc and G. Chen, *J. Appl. Phys.* **97**, 084303 (2005). (Cited on page 65.)
- [169] H. D. Zhou and J. B. Goodenough, *J. Phys. Condens. Matter* **17**, 7395 (2005). (Cited on pages 65 and 67.)
- [170] J. Fleurial, L. Gailliard, R. Triboulet, H. Scherrer, and S. Scherrer, *J. Phys. Chem. Solids* **49**, 1237 (1988). (Cited on page 65.)
- [171] C. Li et al., *J. Alloys Compd.* **372**, 40 (2004). (Cited on page 67.)

- [172] A. M. Glazer, *Acta Crystallogr., Sect. B* **28**, 3384 (1972). (Cited on page 67.)
- [173] T. R. McGuire et al., *J. Phys. Condens. Matter* **37**, 981 (1966). (Cited on page 67.)
- [174] T. Katsufuji and H. Takagi, *Phys. Rev. B* **64**, 054415 (2001). (Cited on page 67.)
- [175] J. Brous et al., *Acta Cryst.* **6**, 67 (1953). (Cited on pages 67 and 69.)
- [176] A. Bussmann-Holder et al., *Phys. Rev. B* **83**, 212102 (2011). (Cited on pages 67 and 71.)
- [177] M. Allieta et al., arXiv:1111.0541. (Cited on page 67.)
- [178] X. Qiu et al., *Phys. Rev. Lett.* **94**, 177203 (2005). (Cited on pages 67 and 77.)
- [179] K. Page et al., *Chem. Mater.* **22**, 4386 (2010). (Cited on page 67.)
- [180] K. Z. Rushchanskii et al., *Phys. Rev. B* **85**, 104109 (2012). (Cited on pages 67, 68, and 74.)
- [181] M. Kachlik et al., *Mater. Lett.* **74**, 16 (2012). (Cited on page 68.)
- [182] A. V. Kityk et al., *Europhys. Lett.* **50**, 41 (2000). (Cited on pages 70 and 72.)
- [183] J. E. Greedan and McCarthy, *Mat. Res. Bull.* **7**, 531 (1972). (Cited on pages 71 and 75.)
- [184] M. Gallardo et al., *J. Phys. Condens. Matter* **14**, 1881 (2002). (Cited on page 71.)
- [185] A. Migliori et al., *Physica B* **183**, 1 (1993). (Cited on page 71.)
- [186] M. Ross and J. S. Story, *Rep. Prog. Phys.* **12**, 291 (1949). (Cited on pages 73 and 77.)
- [187] A. Huq et al., *Z. Kristallogr. Proc.* **1**, 127 (2011). (Cited on page 73.)
- [188] C. L. Farrow et al., *J. Phys. Condens. Matter* **19**, 335219 (2007). (Cited on page 73.)
- [189] B. Etschmann et al., *Z. Kristallogr.* **216**, 455 (2001). (Cited on page 73.)

- [190] E. A. Zhurova et al., *Acta Crystallogr., Sect. B: Struct. Sci* **56**, 594 (2000). (Cited on page 73.)
- [191] *International Tables for Crystallography* (International Union of Crystallography, 1995). (Cited on page 73.)
- [192] J. L. Bettis et al., *Phys. Rev. B* **84**, 184114 (2011). (Cited on page 74.)
- [193] E. Alp et al., *Hyperfine Interact.* **144-145**, 3 (2002). (Cited on page 74.)
- [194] O. Leupold et al., *Europhys. Lett.* **35**, 671 (1996). (Cited on page 74.)
- [195] B. C. Sales et al., *Semiconductors and Semimetals* (Academic Press, 2001). (Cited on page 74.)
- [196] Y. P. Varshni, *Phys. Rev. B* **2**, 3952 (1970). (Cited on page 75.)
- [197] T. R. McGuire et al., *J. Appl. Phys.* **34**, 1345 (1963). (Cited on page 75.)
- [198] E. S. Jeong et al., *Phys. Rev. Lett.* **94**, 147602 (2005). (Cited on page 77.)
- [199] E. S. Božin et al., *Phys. Rev. Lett.* **98**, 137203 (2007). (Cited on page 77.)
- [200] T. Egami and S. J. L. Billinge, *Underneath the Bragg Peaks: Structural Analysis of Complex Materials* (Pergamon Press, 2003). (Cited on page 77.)
- [201] M. Christensen, N. Lock, J. Overgaard, and B. B. Iversen, *J. Am. Chem. Soc.* **128**, 15657 (2006). (Cited on page 78.)
- [202] M. Wuttig and N. Yamada, *Nat. Mater.* **6**, 824 (2007). (Cited on page 83.)
- [203] K. M. Jensen et al., *Phys. Rev. B* (2012), in press. (Cited on page 84.)
- [204] E. S. Božin et al., *Science* **330**, 1660 (2010). (Cited on page 84.)
- [205] M. Li and Z. Yang, in *Electrical and Control Engineering (ICECE), 2010 International Conference on* (2010), pp. 837–841. (Cited on page 87.)
- [206] A. Migliori and J. D. Maynard, *Rev. Sci. Instrum.* **76**, 121301 (2005). (Cited on page 87.)
- [207] URL <http://www.arkema-inc.com/kynar>. (Cited on page 88.)
- [208] J. R. Gladden, *Characterization of Thin films and novel materials using resonant ultrasound spectroscopy* (Pennsylvania State University, 2003). (Cited on pages 88, 92, 100, and 105.)

- [209] V. Braginsky, V. Mitrofanov, and V. Panov, *Systems with Small Dissipation* (The University of Chicago Press, 1985). (Cited on page 89.)
- [210] P. S. Spoor, *Elastic properties of Novel Materials using PVDF Film and Resonance Ultrasound Spectroscopy* (The Pennsylvania State University, 1997). (Cited on page 91.)
- [211] URL <http://www2.dupont.com/Vespe1>. (Cited on page 92.)
- [212] A. Ambrosy and K. Holdik, *J. Phys. E: Sci. Instrum.* **17**, 856 (1984). (Cited on page 92.)
- [213] B.-E. E. Mohajir and N. Heymans, *Polymer* **42**, 5661 (2001). (Cited on page 93.)
- [214] *Model SR844 RF Lock-In Amplifier* (Stanford Research Systems, 2007). (Cited on page 94.)
- [215] G. B. Arfken and H. J. Weber, *Mathematical Methods for Physicists, sixth edition* (Elsevier Academic Press, 2005). (Cited on page 98.)
- [216] URL <http://www.ccp14.ac.uk/tutorial/lmgp/orientexpress.htm>. (Cited on page 100.)
- [217] T. Blachowicz, M. G. Beghi, G. Guntherodt, B. Beschoten, H. Dieker, and M. Wuttig, *J. Appl. Phys.* **102**, 093519 (2007). (Cited on page 104.)

COLOPHON

This thesis was typeset with L^AT_EX 2_ε. 2-d figures were produced either with gnuplot or with Origin. 3-d figures were produced with inkscape or Mathematica. Any self-made related program was written either in Fortran 77 or C.

Final Version as of August 27, 2012 at 12:01.

CURRICULUM VITAE – DIMITRIOS BESSAS

Dimitrios Bessas was born on December 19th 1983 in Lamia, Greece. He participated in the pan-Hellenic exams for attending university education at the Lyceum of Makrakomi in 2001. He received his Degree on Physics from the National and Kapodistrian University of Athens in 2005 and his Master of Science in 2007 from the same university. He carried out his doctoral research at the Forschungszentrum Jülich and the University of Liège under the supervision of Dr. Raphaël Hermann.



AWARDS - SCHOLARSHIPS

2005→2006 *Award / Donation of Professor Efstratios Manousakis, University of Athens, Athens, Greece.*

2003→2004 *Award / Scholarship at the third year of undergraduate studies from the Greek State Scholarship Foundation for exceptional progress, University of Athens, Athens, Greece.*

2001→2002 *Award / Scholarship for the good results in the Pan-Hellenic exams, Intellectual Institution of Roumeli, Athens, Greece.*

CONTRIBUTED TALKS

- i. **D. Bessas**, I. Sergueev, K. Ruschandskii, M. Ležaic, S. Kamba and R.P. Hermann, *Mössbauer spectroscopy and phonon assisted nuclear absorption studies on EuTiO₃*. 7th Seeheim - Workshop on Mössbauer spectroscopy, June 13-17, 2011, Frankfurt, Germany.
- ii. **D. Bessas**, W. Töllner, I. Sergueev, K. Nielsch, R.P. Hermann, *Lattice dynamics on low dimensional chalcogenides*. 9th European Conference on Thermoelectrics, September 28-30, 2011, Thessaloniki, Greece.

CONFERENCE PROCEEDINGS

- a. G.J. Papaioannou, G. Wang, **D. Bessas**, J. Papapolymerou, Proceedings of the 1st European Microwave Integrated Circuits Conference, 513, 2006.

PEER REVIEWED PUBLICATIONS

5. Z. Aabdin, N. Peranio, O. Eibl, W. Töllner, K. Nielsch, **D. Bessas**, R.P. Hermann, M. Winkler, J. König, H. Böttner, V. Pacheco, J. Schmidt, A. Hashibon, C. Elsässer, *Nanostructures, excitations, and thermoelectric properties of Bi_2Te_3 - based nanomaterials*, J. Electron. Mater. **41**, 1792, 2012.
4. N. Peranio, M. Winkler, **D. Bessas**, Z. Aabdin, J. König, H. Böttner, R.P. Hermann, O. Eibl, *Room-temperature MBE deposition, thermoelectric properties, and advanced structural characterization of binary Bi_2Te_3 and Sb_2Te_3 thin films*, J. Alloys Compd. **521**, 163, 2012.
3. Z. Aabdin, N. Peranio, M. Winkler, **D. Bessas**, J. König, R.P. Hermann, H. Böttner, O. Eibl, *Sb_2Te_3 and Bi_2Te_3 thin films grown by room-temperature MBE*, J. Electron. Mater. **41**, 1493, 2012.
2. C.S. Birkel, G. Kieslich, **D. Bessas**, T. Claudio, R. Branscheid, U. Kolb, M. Panthöfer, R.P. Hermann, W. Tremel, *Wet chemical synthesis and a combined X-ray and Mössbauer study of the formation of FeSb_2 nanoparticles*. Inorg. Chem. **18**, 11807, 2011.
1. I. Sergueev, H.-C. Wille, R.P. Hermann, **D. Bessas**, Y.V. Shvyd'ko, M. Zajac, R. Rüffer, *Milli-electronvolt monochromatization of hard X-rays with a sapphire backscattering monochromator*, J. Synchrotron Radiat. **18**, 802, 2011.